Synthesis, modelling and characterisation of gold nanoparticle colloidal crystals

A Thesis presented for the degree of

Doctor of Philosophy

by

Nadine Harris

B.E. Eng. (Elec.) (Hons.): University of Technology, Sydney

Institute for Nanoscale Technology

Faculty of Engineering

University of Technology, Sydney

December 2008

Certificate of Originality

I certify that the work in this thesis has not previously been submitted for a degree nor has it been submitted as part of requirements for a degree except as fully acknowledged within the text.

I also certify that the thesis has been written by me. Any help that I have received in my research work and the preparation of the thesis itself has been acknowledged. In addition, I certify that all information sources and literature used are indicated in the thesis.

Chapter 1 contains a literature review prepared by myself. Chapter 2 describes the theoretical concepts behind the work presented in this thesis and while this theory is described in many textbooks and journal articles, I have presented it here in order to relate the most salient theoretical concepts appropriate to my research. Chapters 3 – 6 detail work done by me under the supervision of Associate Professor Mike Ford and Professor Michael Cortie along with advice from other colleagues. One exception should be noted. The work using the software package COMSOL in section 4.1 was contributed by Dr Matthew Arnold. Chapter 7 contains my concluding remarks and suggestions for future work.

Nadine Harris

Acknowledgements

Firstly, I would like to thank my supervisor Associate Professor Mike Ford whose guidance, infinite levels of patience, enthusiasm and limitless availability were paramount to this work and my development as a researcher. I've know Mike both professionally and socially during the time it has taken me to complete my PhD. During this time he has taught me how to follow the scientific method, the best way to negotiate a jump on my mountain bike, although I never did get it quite right, and finally how to climb Aunty Jack. I would also like to thank my co-supervisor Professor Michael Cortie for many discussions and support. I am indebted to all of my peers at the University of Technology, Sydney (UTS) in particular Dr Andrew McDonagh for his patience in supplementing my knowledge of chemistry, Dr Chris Poulton for his mathematical guidance, Ms Katie McBean for her help with Scanning Electron Microscopy and Dr Matthew Arnold for all things optical. Fellow PhD students, both past and present, who have helped me during my PhD include Dr Benjamin Soulé de Bas, Dr Rainer Hoft, Ms Dakrong Pissuwan, Mr Burak Cankurtaran, Mr Nicholas Stokes, Mr Michael (Bob) Coutts, and of course Mr Marty Blaber, who is exceedingly generous and has taught me many things during my PhD. In particular, how to program and write scripts which have saved me a considerable amount of time.

This PhD would not have been possible without the financial support of the Australian Research Council (ARC) and the ample computing time provided by the Australian Partnership for Advanced Computing (APAC) and the Australian Centre for Advanced Computing and Communications (AC3).

I have been fortunate enough to have been supported by many researchers external to UTS and I would like to thank Dr Åsa Jamting, Dr Bruce Warrington and Mr Malcolm

Lawn from the National Measurement Institute (NMI) in Lindfield for allowing me to use their particle sizer and laser. Also, thanks to Professor Paul Mulvaney from the University of Melbourne for his advice in both experimental and career matters and Professor Julian Gale from Curtin University for his help with GULP.

Finally, I would like thank my husband Gary and at this point I am lost for words to express how grateful I am for his unparalleled support while I have been working on my PhD. He will know what I mean when I simply say, “cheers mate!”

Contents

List of Figures

List of Tables

Glossary of Acronyms

BCC	Body Centred Cubic
CMR	Clausius Mossotti Relation
CTAB	Cetyltrimethylammonium Bromide
DDA	Discrete Dipole Approximation
DLS	Dynamic Light Scattering
EDS	Energy Dispersive Spectroscopy
ESEM	Environmental Scanning Electron Microscope
FCC	Face Centred Cubic
GULP	General Utility Lattice Program
HCP	Hexagonal Close-Packed
HHDT	16-Hydroxy-1-Hexadecanethiol
ITO	Indium-doped Tin Oxide
LBL	Layer By Layer
LDR	Lattice Dispersion Relation
MD	Molecular Dynamics
MEA	Mercaptoethyl Alcohol
MMA	Methyl Methacrylate
MSA	Mercaptosuccinic Acid
MUOH	11-Mercapto-1-Undecanol
MUTEG	1-Mercaptoundecyl Tetra(Ethylene Glycol)
NAG	N-Acetylglutathion
NIR	Near-Infrared
NNLS	Non Negative Least Squares Fit

PBCGST	Preconditioned BiConjugate Gradient Stabilisation
PIM	Parallel Iterative Methods
pMA	p-marcaptoaniline
PML	Perfectly Matched Layer
PMMA	Polymerised Methyl Methacrylate
SAXS	Small Angle X-ray Scattering
SC	Simple Cubic
SCLDR	Surface Corrected Lattice Dispersion Relation
SEM	Scanning Electron Microscope
SERS	Surface Enhanced Raman Scattering
TEM	Transmission Electron Microscope
T-matrix	Transition matrix
UV	Ultraviolet

Abstract

Three-dimensional, micron-sized colloidal crystals comprised of gold nanospheres have been synthesised directly from a gold nanoparticle/methyl methacrylate (MMA) colloid by application of a 514 nm laser at 480 mW. An array of colloidal crystals can be created by translation of the glass substrate under the laser beam, after two minutes of irradiation at each site. Control experiments and calculations show that plasmon-induced localised heating of the gold nanoparticles contributes to the rapid formation of colloidal crystals.

The effects of particle order and disorder on the optical response of three-dimensional structures containing 15 nm diameter gold nanospheres are investigated using the T-matrix technique. Calculations were performed on structures containing up to 163 particles. The ordered structures produce an additional extinction peak that is not present in the disordered structures. The position of this additional peak depends upon the inter-particle spacing. In the disordered structure this peak is therefore missing because the inter-particle spacing is not well-defined.

The optical response of a simplified array of a one-dimensional chain of 15 nm diameter gold nanospheres in the regime where the near-fields of the particles are coupled is investigated using the T-matrix technique. Calculations are performed with chains up to 150 particles in length and with an inter-particle spacing between 0.5 and 30 nm. For wavevectors perpendicular to the chain axis and longitudinal polarisation the extinction peak red-shifts as the inter-particle spacing is reduced. The magnitude of the peak-shift is inversely proportional to the inter-particle spacing, a result that is consistent with the Van der Waals attraction between two spheres at short range. For a fixed particle gap the

extinction peak tends towards an asymptotic value with increasing chain length, with the asymptotic value determined by the inter-particle spacing.

A nanoshell geometry that produces maximum absorption efficiency is investigated using a formulation of Mie theory. The calculated surface heat flux under sunlight (800 W/m^2) and laser (50 kW/m^2) irradiation is used to determine the temperature of the nanoshell using a convective heat transfer model. For irradiation by sunlight, the resultant heat flux is optimised for an 80 nm diameter nanoshell with an aspect ratio of 0.8, while for irradiation by laser the maximum heat flux is found for 50 nm nanoshells, but with an aspect ratio of 0.9.

A direct comparison between the absorption efficiencies of geometrically varying nanoshells and nanorods is performed using a formulation of Mie theory and the Discrete Dipole Approximation (DDA) technique, respectively. The absorption efficiency produced by nanorods far exceeds that produced by nanoshells for a constant volume of gold.

Chapter 1

1. Introduction

1.1. Overview and motivation

This thesis describes the synthesis and modelling of three-dimensional gold nanoparticle colloidal crystals. These structures have unique optical properties due to the collective behaviour of the assembled nanoparticles within the array. Potential applications of these structures include photonic crystals[1-4] and active substrates for Surface-Enhanced Raman Scattering (SERS).[5-11]

Initially it would seem appropriate to describe the progression of the field of plasmonics from individual gold nanospheres through to collective arrays of nanospheres in colloidal crystals. Therefore Chapter 1 contains a literature review presenting the optical properties and common synthesis techniques of nanospheres, nanoshells, nanorods, dimers, chains and colloidal crystals.

Chapter 2 is a theoretical section describing the mathematical basis underlying the computational techniques used to model these structures. These include Mie theory, Gans theory, the Discrete Dipole Approximation (DDA) and the T-matrix technique.

The results chapters presented in this thesis combine both experimental and computational research. The experimental component focused on synthesising gold nanoparticle colloidal crystals while computational analysis focused on investigating the

optical response of both individual and arrays of gold nanoparticles. The results chapters are presented in the following order.

Chapter 3 describes a facile technique that was developed to synthesise three-dimensional colloidal crystals from gold nanospheres by exploiting the localised heating effects of laser irradiation. This work has been published in a paper entitled, "*Laser-induced assembly of gold nanoparticles into colloidal crystals*" by Nadine Harris, Mike J. Ford, Michael B. Cortie and Andrew M. McDonagh in *Nanotechnology*, 2007, **18**, 365301. Also presented in this chapter is computational analysis of three-dimensional gold nanoparticle structures with the express purpose of examining the effect of order and disorder on their optical response. The T-matrix technique was used for these calculations and led to interesting and unexpected results. In order to further elucidate the physical phenomenon associated with the optical response of these structures a much simpler structure of a chain of gold nanospheres was considered. These results constitute the bulk of the contribution to this thesis and are reported in Chapter 4.

Specifically, Chapter 4 uses the T-matrix technique to investigate the optical response of ordered chains containing up to 150 particles of gold nanospheres with small inter-particle gaps with the aim of investigating the effect of long-range order in the near-field regime. These results have been published in a paper entitled, "*Plasmonic resonances of closely-coupled gold nanosphere chains*" by Nadine Harris, Matthew D. Arnold, Martin G. Blaber and Mike J. Ford in the *Journal of Physical Chemistry C*, 2009, **113,** 2784. This work was also extended to a long chain of silver nanosphere dimers in an attempt to combine near-field and diffractive effects in one structure.

The effect of the rapid formation of colloidal crystals from laser irradiation due to localised plasmonic heating was examined in Chapter 3. Nanoshells and nanorods have the ability to exploit these localised heating effects far more efficiently than nanospheres. Therefore, Chapter 5 reports the use of an implementation of Mie theory to calculate the nanoshell geometry that provides optimum absorption efficiency in order to calculate the maximum nanoshell temperature under sunlight and laser irradiation. These results have been published in a paper entitled, "*Localized plasmonic heating of gold nanospheres and*

nanoshells" by Nadine Harris, Mike J. Ford and Michael B. Cortie in the *Journal of Physical Chemistry B*, 2006, **110**, 10701

In Chapter 6 the DDA technique and an implementation of Mie theory were used to calculate and compare the absorption spectra of nanorods and nanoshells, respectively, with the aim of determining the geometry that provides the best absorption efficiency for a constant volume of gold. These results have been published as a paper entitled, "*Nanoparticles: The case for gold rods and shells*" by Nadine Harris, Mike J. Ford, Paul Mulvaney and Michael B. Cortie in *Gold Bulletin*, 2008**, 41**, 5.

Finally, Chapter 7 details a summary of the work presented in this thesis along with suggestions for future research and concluding remarks.

1.2. Literature review

1.2.1. Progress in the field of plasmonics

Gold nanoparticles of varying geometries have stimulated considerable research interest owing to their unique optical properties. Nanospheres with diameters in the size range of about 10 to 100 nm have large absorption cross-sections that surpass their geometric cross-sections. This is possible due to the production of a plasmon resonance, whereby the conduction electrons of the nanosphere are polarised into a resonant condition from the electric field of the incident light.[12-14]

Techniques for preparing gold nanospheres have been know since Roman times[15, 16] and have since been modified to enable almost monodispersed production of either citrate or organically stabilised nanospheres.[17, 18]

Nanospheres with diameters smaller than about 5 nm suffer from plasmon damping and the magnitude of the absorption efficiency is reduced because the diameter of the particle is considerably less than the mean free path of bulk gold.[14] For particles with diameters less than about 2 nm the plasmon disappears entirely[19] and scattering mechanisms dominate for particles larger than about 100 nm.

The ability to tune the position of the plasmon resonance peak to a desired wavelength is somewhat limited for gold nanospheres with diameters between 10 and 100 nm because the plasmon resonance position is considered to be size independent.[20] When the diameter is increased beyond 100 nm, scattering begins to dominate, the peak red-shifts and broadens within the spectrum, and suffers the disadvantage on no longer providing efficient absorption.

Aden and Kerker[21] presented a way in which this limitation could be overcome when they provided a solution to the problem of the scattering of a plane wave from a sphere with a concentric shell, known as a core-shell particle, or nanoshell. For the case of a dielectric core with a metallic shell, such as gold or silver, plasmon resonances associated with the core and shell are produced, then interact or hybridise[22] and shift the position of the plasmon resonance into the infrared part of the spectrum. The aspect ratio, which is the ratio of the inner core to the outer shell diameter, determines the extent to which the plasmon peak resonance is shifted. Thinner shells provide greater hybridisation and therefore a greater peak position shift when compared to thicker shells.

An alternative method for achieving the same ends is the use of gold nanorods.[23] These particles have two absorption peaks corresponding to excitation of the longitudinal and transverse plasmon. While the transverse plasmon remains at more or less the same position as a sphere of the same diameter, the longitudinal plasmon red-shifts as the aspect ratio, the ratio of the length to the width, of the nanorod increases.[24]

It is now well established that the optical response of an individual gold nanoparticle can be tuned by changing the dielectric of the surrounding medium but more dramatically by changing the nanoparticle geometry itself.[25] This has prompted great interest in the synthesis and study of not only nanoshells[26-29] and nanorods[30-33] but a wide variety of other geometries such as, stars,[34-37] octahedra,[38-40] decahedra,[41] crescents,[42-45] rattles,[46] triangles[47-50] and rice[51, 52] to name a few, where the main aim is to create a particle geometry that provides a very controlled, highly absorbing plasmon resonance at the desired wavelength. For this reason, applications have been proposed that exploit this strong absorption such as thermal therapy of selectively targeted cells,[53-56] *in vivo* drug delivery systems [57-59] and energy efficient window coatings.[60]

Dimers, chains and arrays of nanospheres, such as colloidal crystals, present a further method for controlling the position or shape of the plasmon resonance.[61-63] The optical response of these structures can be considered in the near- and far-field regimes. In the near-field regime the inter-particle spacing between the nanospheres is quite small, normally less than about 50 nm, and there is considerable overlap between the particle near-fields forcing the plasmon resonance to shift into the infrared part of the spectrum. In the far-field regime the inter-particle spacing is quite large, comparable to the wavelength of the incident light, and no interaction can be seen between the near-fields of the particles. Under these conditions diffractive effects start to dominate.

Schematic illustrations of the geometries considered in this thesis are shown in figure 1.1.

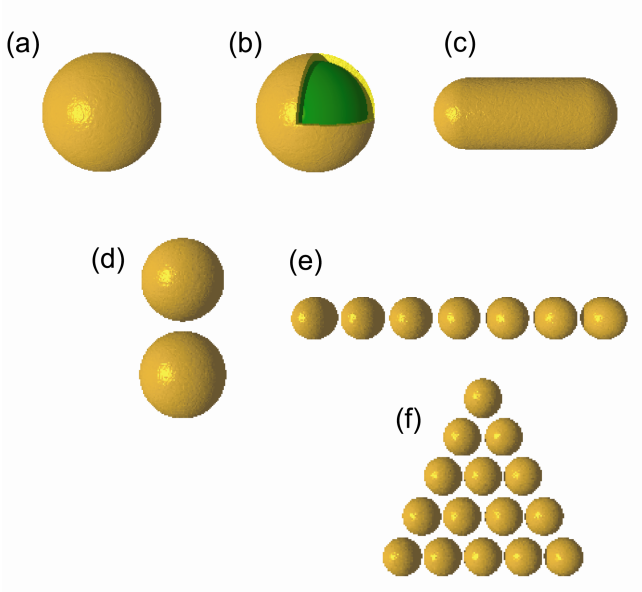

Figure 1.1. Schematic illustration of gold nanostructures investigated in this thesis **(a)** nanosphere, **(b)** nanoshell, **(c)** nanorod, **(d)** dimer, **(e)** chain and **(f)** colloidal crystal.

1.2.2. Nanospheres

Gold spherical nanoparticles, which are smaller than the wavelength of the incident light, are capable of producing brilliant red pigmentation and have been used since Roman times as a means of decorating glass windows and vessels, such as, the Lycurgus cup.[16, 64-

[66] The cup is on display in the British Museum in London and contains a 14:1 molar ratio of silver and gold nanoparticles of about 70 nm in diameter.[16] The presence of these particles is responsible for the interesting optical properties of the cup. When viewed in transmission the cup appears red, in contrast when viewed with reflected light, it appears opaque green.

Despite the successful synthesis of nanoparticles during Roman times little was known about the physical process responsible for the red colouration until 1857 when Michael Faraday[67] hypothesised that gold was present in a divided state. His ensuing synthesis of colloids ranging in colour from red to amethyst led to the discovery that the variation of particle size gives rise to a variety of resulting colours. However, he had no way of measuring the size of the particles.[19]

In 1908 Gustav Mie[68] solved Maxwell's equations[13] to calculate the extinction efficiency of an arbitrary sized spherical particle. This is known as Mie theory and will be described in greater detail in Chapter 2. The use of Mie theory explained that the red colouration of gold nanospheres is due to their ability to absorb more light than their geometric cross-section will allow. This intense particle absorption is due to the production of a dipole plasmon resonance. A schematic illustration of dipole plasmon resonance production is shown in figure 1.2.[65]

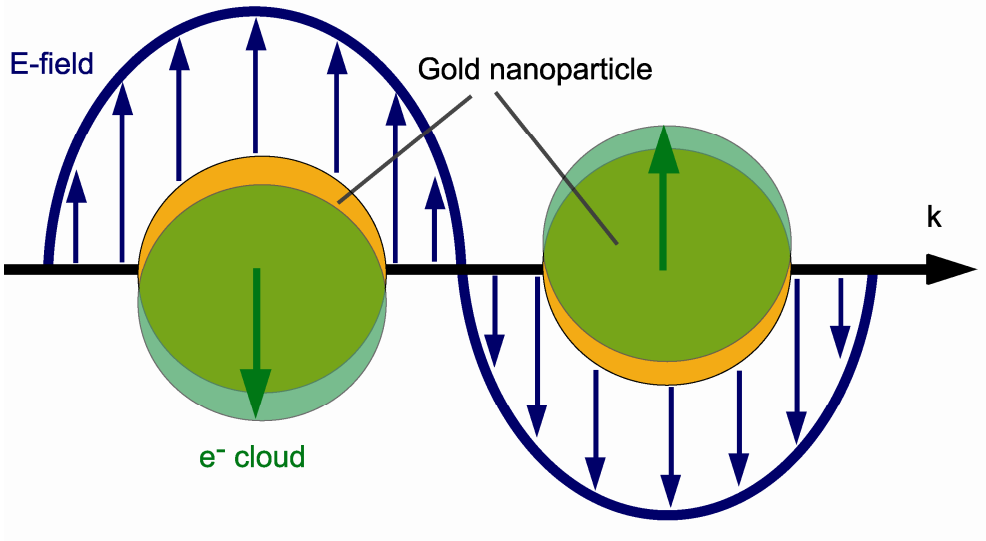

Figure 1.2. Schematic illustration of the production of a dipole plasmon resonance in a gold nanosphere.

When a gold nanoparticle, with a diameter of between about 10 and 100 nm, is irradiated by light with a wavelength much greater than the particle diameter, the conduction band free electrons (e^- cloud) are displaced relative to the fixed background of immovable positive ions by the oscillating electric field (E-field) of the incident light.[12, 65] The e^- cloud will acquire momentum from the E-field and overshoot the equilibrium position where a restoring force arises from the Coulomb attraction between the displaced e^- cloud and the nuclei of positive ions. This results in an oscillation of the e^- cloud known as a dipole plasmon resonance.[12, 65] The wavelength at which the plasmon resonance is produced is longer if the electrons are less tightly bound. For gold this occurs in the visible part of the spectrum at about 520 nm.[25]

The establishment of a dipole plasmon resonance is not dependent upon size when the particle diameter is much smaller than the wavelength of the incident light.[13, 14] However, the magnitude and width of the plasmon resonance is reduced and broadened in particles with diameters of less than about 5 nm and disappears completely for particles with diameters less than about 2 nm.[19] This has been shown experimentally for gold clusters.[69, 70]

Both classical physics and quantum mechanical models have been used to describe this phenomenon. The classical approach describes an increase in the damping constant of the Drude-free electron model from additional random collisions by the electrons with the particle surface causing incoherence in the plasmon oscillation. This phenomenon is generally referred to as surface-scattering.[13, 19]

The Drude-free electron model states that the real (ε') and imaginary (ε'') parts of the dielectric function are[13]

$$\varepsilon' = 1 - \frac{\omega_p^2}{\omega^2 + \gamma^2} \qquad 1.1$$

$$\varepsilon'' = \frac{\omega_p^2 \gamma}{\omega(\omega^2 + \gamma^2)} \qquad 1.2$$

where ω_p is the plasma frequency, $\omega = \frac{2\pi c}{\lambda}$, c is the speed of light in a vacuum, λ the wavelength of incident light and γ the bulk damping constant, which is inversely proportional to the electron-electron, electron-phonon and electron-defect scattering times in the bulk material[19]

$$\gamma_{bulk} = \frac{1}{\tau_{e-e}} + \frac{1}{\tau_{e-ph}} + \frac{1}{\tau_{e-d}} \qquad 1.3$$

An additional term, which accounts for electron-surface scattering is added to equation (1.3) and γ becomes a function of particle radius[13, 14, 19]

$$\gamma(r_{eff}) = \gamma_{bulk} + \frac{Av_F}{r_{eff}} \qquad 1.4$$

where A is an empirically found constant, v_F is the electron velocity at the Fermi surface and r_{eff} is the effective mean free path of collisions. Kreibig[14] used $r_{eff} = \frac{4a}{3}$ for a particle with radius a.

Kawabata and Kubo[71] disagree with the classical physical approach and have reported a quantum mechanical model that suggests the surface of the particle does not contribute to electron scattering but does determine the electron eigenstates within the particle. They suggest that damping of the plasmon resonance is caused by the transfer of energy between the individual eigenstates.

Despite the disagreement between classical and quantum models both models show that size effects are apparent in small particles that cause modification of the bulk dielectric function.

Particles with diameters larger than about 100 nm are not efficient absorbers as they scatter more light than they absorb because higher-order modes begin to dominate and the E-field from the incident light can no longer polarise the particle homogeneously. This results in a broadening and red shift of the plasmon resonant peak position.[19] Moreover, changes in the electron density[72] and refractive index of the particle as well as the refractive

index of the surrounding medium[20] contribute to altering the position and shape of the plasmon resonance peak.

Methods for preparing gold spherical nanoparticle colloids have been known for several decades[17] with the type of colloid produced falling into one of two categories, namely an aqueous or organic colloid. The basic mechanism behind particle production involves reducing metal ions with an appropriate reducing agent[25] and then capping the particles with a stabilising agent to prevent aggregation.

Aqueous colloids are the least complex to synthesise and one of the most popular techniques[25] was developed by Turkevich *et al.*[73] In this method the addition of sodium citrate to a boiling solution of gold chloride ($HAuCl_4$) acts as a reducing agent and nucleation of the gold atoms starts to occur. The solution first turns colourless, then dark grey and eventually deep burgundy as the dissolved salt starts to form gold spherical nanoparticles. In this case the sodium citrate acts as both the reducing agent and the stabilising agent through electrostatic interactions.

One of the most popular techniques for producing an organic gold colloid was developed by Brust *et al.*[74] Here gold chloride ($HAuCl_4$) was reduced by sodium borohydride in the presence of an alkanethiol producing 1-3 nm diameter thiol stabilised particles. An advantage of organically stabilised particles is that they can be dried, which allows for long storage times, and re-suspended in other organic solvents.[18]

Over time these synthetic methods have been supplemented with additional methods for controlling the size and monodispersity of the spherical nanoparticles.[18, 75, 76]

1.2.3. Nanoshells

During the 1950's it was realised that core-shell nanoparticles could be used to tune the position of the particle plasmon resonance peak.[21] A thin shell of gold surrounding a spherical dielectric core will have a plasmon resonance associated with the outer and inner surface of the shell. As the shell thickness is decreased the two plasmons will interact with each other more strongly and hence shift in position relative to the position of a resonance on the surface of sphere or one inside a spherical cavity. This effect has been described in

terms of hybridisation of the two plasmon resonances in analogy with hybridisation of molecular orbitals seen in quantum chemistry.[22] Clearly, if the shell is made sufficiently thick the cavity resonance is not excited by the incident light and the nanoshell will approximate a solid sphere. For thin shells, however, the plasmon absorption can be tuned from the visible into the near infrared by varying the aspect ratio of the nanoshell alone, that is by changing the relative thickness of the shell to the core.[77]

This ability to tune the magnitude and position of the plasmon resonance within the spectra has been proven experimentally by several groups.[27, 28, 78-81] In particular Oldenburg *et al.*[27] observed a plasmon blue shift from around 810 nm to around 710 nm as the gold shell on a 120 nm diameter silica particle increased in thickness from around 20 nm to 33 nm. Moreover Liang *et al.*[28] saw a peak shift from 526 nm to 628 nm as they reduced the gold shell thickness from 30 nm (solid sphere) to around 10 nm, thereby increasing the size of the hollow cavity core. Liu *et al.*[79] reacted $HAuCl_4$ with silver particles and observed a peak shift from 400 nm to 800 nm as the particle cavity diameter increased and the shell thickness decreased.

The observed peak shift is not unique to gold shells. The criterion for the establishment of this geometry dependent phenomenon is the existence of a negative real part of the dielectric constant of the shell metal within the visible regime, as will be described in greater detail in Chapter 2. Consequently the peak absorption of nanoshells made from a metal such as silver can also be tuned or engineered. This has been demonstrated by Chen and co-workers[78] who synthesised silver nanoshells with outer diameters of 40 – 50 nm and inner diameters of 20 – 30 nm. They observed a resonant peak at 395 nm for a 20 nm diameter solid silver particle however, when these particles were transformed into nanoshells the resonant peak red-shifted to 506 nm.

Wet chemistry techniques are the most common method used to synthesise gold nanoshells, with two of the most simple and elegant methods developed by Zhou *et al.*[81] and Liu *et al.*[79] Zhou reduced the surface of gold sulphide (Au_2S) nanoparticles with sodium sulphide (Na_2S) to produce a gold layer on the surface of the gold sulphide particles. Liu produced 20 nm silver – gold, core – shell particles by reacting silver

nanoparticles with chloroauric acid ($HAuCl_4$), which led to the formation of gold shells around the silver nanoparticles.

Template-mediated methods, which employ layer-by-layer (LBL) deposition,[82] are slightly more complicated than the methods of Zhou *et al*. and Liu *et al*., however they are more common because they provide greater control over the final shell morphology.[83] Oldenburg *et al*.[27] produced silica – gold, core – shell particles with diameters of around 120 nm by functionalising the surface of silica nanoparticles with 3-Aminopropyltriethoxysilane then partially cover the surface with 1 – 2 nm gold particles that were covalently bound to the 3-Aminopropyltriethoxysilane. Then the silica particles, with the partial gold covering, behave as nucleation sites for the reduction of chloroauric acid ($HAuCl_4$) and potassium carbonate (K_2CO_3) by a solution of sodium borohydride ($NaBH_4$), resulting in an increased coverage of gold particles on the surface of the silica particles. This technique has been modified for polystyrene, as opposed to silica cores, by Shi *et al*.[84] In their preparation aminoethanethiol was used as a linker molecule on the surface of carboxylate-terminated polystyrene cores upon which gold nanoparticles were adsorbed. Compared to the methods described by Zhou *et al*. and Liu *et al*. these techniques produce much larger diameter shells of several hundred nanometers because of the initial diameter of the silica or polystyrene nanoparticle template.

The use of solid cores in shell synthesis provides mechanical rigidity, however hollow core shells[85] are attractive because of their relatively low density when compared to core-shell particles with equivalent dimensions.[83]

Sun *et al*.[86] used a template engaged replacement reaction to produce gold shells with hollow interiors. These shells were around 50 nm in diameter with a shell thickness of around 4.5 nm. Liang *et al*.[28] synthesised 60 nm diameter hollow gold shells by using cobalt nanoparticles as sacrificial templates and shell thicknesses varied between 10 and 30 nm depending upon the sample preparation technique. Pastoriza *et al*.[83] used LBL to produce hollow metallodielectric nanoshells whereby nanorods were deposited onto 705 nm diameter polystyrene spheres followed by a sol-gel process, which produced a silica or titania outer shell that allowed improved particle robustness and rigidity. Ammonia was used to dissolve the polystyrene core template and control over shell thickness was

achieved by controlling rod density. Varying the aspect ratio of the nanorods and their density on the surface of the polystyrene core allowed optical tuneability.

Dissolution of the core to produce hollow shells is most common however, heat can also be used to achieve the same result. Prasad *et al.*[57] irradiated silica-gold, core-shell particles using a pulsed laser, which removed the silica core leaving water-gold, core-shell particles.

The synthesis of gold nanoshells with hybrid cores is also possible. Ji *et al.*[87] used wet chemistry techniques to synthesise a gold shell with a super paramagnetic iron oxide – silica core. Their aim was to combine the magnetic and a NIR optical response of the shells to enhance the efficacy of photothermal therapy by directing the shells to tumours through the application of an external magnetic field.

Other shell synthesis techniques have been developed. Pol *et al.*[88] used ultrasonic irradiation to coat polystyrene spheres with silver, gold, palladium and platinum nanocrystals, producing shells of around 0.5 microns. Finally, electro less plating was used by Suzuki *et al.*[89] to produce 250 nm diameter shells. Within this method gold nanoparticles were attached to thermo sensitive hybrid core-shell particles whereupon they were treated with electro less gold plating.

1.2.4. Nanorods

The surface plasmon resonance of a nanorod splits into two distinct modes known as the ‘longitudinal’ and ‘transverse’ modes. Excitation of the longitudinal mode results from electron oscillation along the long nanorod axis, while transverse mode electrons oscillate along the short axis of the nanorods.[90] The longitudinal response, in particular, is sensitive to the aspect ratio, which is the ratio of the length of the long axis to the short axis and as the aspect ratio is increased the longitudinal plasmon peak position red-shifts into the infrared part of the spectrum. On the other hand the transverse resonance blue-shifts as the aspect ratio of the nanorod is increased to the point where the resonance position corresponds to that of a sphere with the same diameter as the nanorod.

As with nanoshells the ability to tune the plasmon peak position of nanorods has also been demonstrated experimentally.[31, 91-97] For example Yu *et al.*[91] saw a longitudinal plasmon peak shift to wavelengths of 600, 710 and 873 nm as the aspect ratio of their gold rods was increased from 1.8 to 3.0 and then 5.2, respectively.

Murphy and co-workers demonstrated that the rod aspect ratio depended on the size and nature of the seed[95] as well as the nature of the surfactant.[94] When they varied the C_nTAB chain length during the seed-mediated growth process from n = 10, 12, 14 and 16 they increased the aspect ratio of the rods. The use of C_{10}TAB resulted in solid gold spheres with a surface plasmon at 528 nm. As n was increased, the aspect ratio of the rods increased and the transverse plasmon blue shifted slightly to around 520 nm and the longitudinal plasmon peak shifted from 820 nm (aspect ratio of 5 ± 2 with C_{12}TAB) to around 1800 – 2200 nm (aspect ratio of 17 ± 3 with C_{14}TAB) and then beyond 2200 nm for 23 ± 4 aspect ratio rods with C_{16}TAB.[94]

Payne *et al.*[93] observed multiple higher order plasmon resonances in colloidal suspensions of gold rods with fixed diameter (85 nm) with varying lengths (96 nm, 641 nm, 735 nm and 1175 nm).

Wet chemistry techniques such as template, electrochemical and seed-mediated methods are used to synthesise nanorods. Martin[98] developed a template synthesis technique whereby the desired rod material is electrochemically deposited into uniform diameter, cylindrical pores of a nanoporous membrane. To retrieve the individual rods the membrane is selectively dissolved and the rods are dispersed in a solution such as water or an organic solvent.[23] Using this technique Cepak *et al.*[92] deposited gold into polycarbonate filtration membranes producing rods of varying aspect ratio with diameters of 40 and 90 nm. More recently Payne *et al.*[93] used the same technique to synthesise gold rods with an average diameter of around 85 nm with varying aspect ratios by electrochemically depositing gold into anodic aluminium oxide templates. This technique does have the disadvantage of producing a low yield.[23]

Yu *et al.*[91] developed an electrochemical synthesis technique where two 3 x 1 x 0.05 cm electrodes, one made of gold (anode) and the other made of palladium (cathode) were immersed in an electrolytic solution containing a cationic surfactant,

cetyltrimethylammonium bromide (CTAB) and a rod-inducing cosurfactant, tetraoctylammonium bromide (TC_8AB). Synthesis occurs under ultrasonication and the bulk gold metal is converted from the anode to produce gold rods at the cathode surface. Using this method they produced gold rods with a mean transverse diameter of 10 nm with aspect ratios of 2.6 and 7.6.

Jana *et al.*[31] use a seed-mediated growth technique to synthesis gold rods. A growth solution containing chloroauric acid ($HAuCl_4$), CTAB and ascorbic acid is prepared. Then a seed solution of 3.5 nm gold particles is prepared by combining chloroauric acid ($HAuCl_4$) and tri-sodium citrate ($Na_3C_6H_5O_7$), after which time sodium borohydride ($NaBH_4$) is added. The ascorbic acid within the growth solution is too weak to reduce the chloroauric acid ($HAuCl_4$) in the presence of the CTAB, however the addition of the seed solution to the growth solution causes very fast reduction of the chloroauric acid ($HAuCl_4$) and the growth of rods. Wu *et al.*[99] report that replacement of the capping agent of the gold particles in the seed solution with CTAB as opposed to tri-sodium citrate ($Na_3C_6H_5O_7$) increases the yield of nanorods, with an average aspect ratio of 19, to over 90 %. Moreover, production of by-products such as triangular nanoplates is reduced.

When using the seed-mediated method, the mechanism of rod growth is unclear.[23] Nevertheless the ability to control nanorod aspect ratio, monodispersity and yield have been demonstrated by many groups to be greatly influenced by the size and stability of the seed along with the nature and concentration of the surfactant.[23] For example Gao *et al.*[94] showed that as the chain length of the C_nTAB was increased, the aspect ratio of the rods also increased and Jana *et al.*[31] showed that using a three step seed-mediated synthesis process produces larger aspect ratio rods (13 ± 2 aspect ratio) than those produced by a one step seed-mediated process (4.6 ± 1 aspect ratio).

Size control after nanorod growth is also possible.[100] Recently Tsung *et al.*[101] and Kou *et al.*[102] demonstrated anisotropic shortening and transverse overgrowth of gold nanorods through oxidation[103] with H_2O or the addition of cysteine to the nanorod solution. Cysteine carries a thiol group at one end and an carboxyl-amino zwitterionic group at the other end,[103] as such, the cysteine can bind preferentially to the nanorods ends and induce transverse overgrowth on the side of the nanorods.

1.2.5. Dimers and one-dimensional chains of nanoparticles

The optical properties of dimers, chains and other arrays can be thought of, at least to a certain degree of approximation, in two regimes. Far-field where the inter-particle gaps are large and there is little overlap between the near-fields of the particles. Diffractive type effects can be seen in this regime when the inter-particle gaps are similar to the wavelength of the incident light and the individual particles have significant scattering cross-sections.[63, 104-106] Recently Zou and Schatz[104] showed that very large and narrow resonances positioned in the infrared part of the spectrum and giant enhancements in the electromagnetic fields can be produced by large chains of 100 nm diameter silver nanospheres with very large inter-particle gaps for polarisation perpendicular to the chain axis.

In the near-field regime the inter-particle gap is sufficiently small so that the near-fields of the particles are coupled. The plasmon resonance in this regime can be tuned deep into the infrared by decreasing the inter-particle gap and very strong enhancement of the electric field between the particles can be achieved.[62]

A significant amount of research has focused on dimers[107-116] while studies on long chains (> than 50 particles) have generally focused on their potential applications as substrates for biological sensors that utilise SERS[104-106, 117] or propagation studies for their potential use as waveguides[118, 119] in both cases with inter-particle gaps close to or larger than the wavelength of the incident light. Quinten and Kreibig[120] have performed T-matrix calculations in the near-contact regime on chains and other arrangements containing 30 silver particles, however their calculations considered the dipole and quadrupole contributions only.

An exact expression for the effective permittivity for cubic lattices of spheres has been derived by McKenzie and McPhedran[121] based upon the Rayleigh treatment. The authors demonstrate that many orders are required to reproduce the correct divergence of the permittivity as the conducting spheres approach contact. A multiple-scattering method has been applied to clusters containing up to five aluminium nanospheres by García de Abajo,[122] and a review of light scattering by two-dimensional periodic arrays of particles and holes has been given by the same author.[123] More recently, Sainidou and García de Abajo have demonstrated a planar metamaterial with large effective permittivity composed

of an array of nearly touching particles.[124] In this work the authors show that these nanoparticle based metamaterials are capable of supporting localised plasmonic modes.

The dimer is an interesting and comparatively well-studied problem.[61, 62, 125] The dipole resonance shifts to longer and longer wavelengths as the spheres approach each other and higher order modes continue to appear at shorter wavelengths. The point of contact is a singularity. As shown recently by Romero *et al*.[62] when the contact point is reached an additional mode is possible where charge is transferred between the two spheres. In practice, other effects such as electron tunnelling or necking between the two particles may dominate in the near contact region. Nevertheless, the predicted shift in the resonance with decreasing particle gap has been measured experimentally between gold spheres by Rechberger *et al*.[62] and between gold nanoshells by Lassiter *et al*.[126]

It has been proposed that the strong distance-dependence of the resonance wavelength enables dimers to be used as "plasmon rulers" [107, 127, 128] for measuring distance in objects such as cells. Jain *et al*. [107] have recently reported a universal scaling behaviour for the shift in the resonance of particle dimers and have derived, from optical measurements and calculations, a universal plasmon ruler equation. Lithographical techniques were used to synthesise nanodisc pairs with varying inter-particle gaps. For polarisation parallel to the dimer axis the fractional plasmon wavelength shift was observed to decay exponentially with increasing inter-particle gap, with a decay length of 0.2 in units of particle size. Furthermore, the authors found that this decay constant applies to nanoparticles with different sizes or shapes, or particles made from different materials.

Wet chemistry techniques are commonly employed to synthesise one-dimensional chains from gold nanoparticles, where the aim is to produce highly anisotropic chains with controlled inter-particle spacings. Synthesising these structures in solution is advantageous as it is relatively fast, when compared with lithographical techniques, and minimises unwanted binding of nanoparticles to the substrate.[129] Warner and Hutchison[129] used DNA as a scaffold for the assembly of extended one-dimensional chains. Gold nanospheres, with an average diameter of about 2 nm, were functionalised with a cationic head group in the ligand shell, which enabled the self-assembly of the nanospheres onto the negatively

charged phosphate backbone of the DNA scaffold. This produced one-dimensional chains of up to 1 micron in length with an average inter-particle spacing of about 1.4 nm.

Larger chains of 13 nm diameter gold particles with lengths ranging from 1 – 5 microns, containing of 80 – 380 particles, have been reported by Lin *et al.*[130] In this case self-assembly of the particles is triggered by exchanging the citrate ions adsorbed on the surface of the gold nanoparticle with the ditopic molecule, mercaptoethyl alcohol (MEA). The replacement of the negatively charged citrate ions with neutral MEA molecules reduces the electrostatic repulsion between the gold nanoparticles and allows the formation of chain assemblies.

Control over both chain length and inter-particle spacing is essential and the former has been reported by Liao *et al.*[131] where chains were formed in ethanol due to electrostatic interaction and coagulation of citrate stabilised 10 nm diameter gold particles. Only single particles were present for low particle concentrations of 5 mg/ml, however average chain lengths of 26 particles could be produced with concentrations of 40 mg/ml. Moreover, coagulation of the particles meant that there was no inter-particle spacing within the chains.

Control over inter-particle separation has been demonstrated by Sarder *et al.*[132] Asymmetrically functionalised gold nanospheres with diameters of 10 and 30 nm were synthesised and used as building blocks to produce chains of 14-18 particles by using a polymer template. Inter-particle spacing could be controlled by changing the length of the ligands. For example, inter-particle spacings of about 2.7 nm were reported for the 11-mercapto-1-undecanol (MUOH) ligand, whereas when a longer ligand, 16-hydroxy-1-hexadecanethiol (HHDT) is used, inter-particle spacing increases to about 3.3 nm. Inter-particle spacing was further increased to about 5.4 nm when 1-mercaptoundecyl tetra(ethylene glycol) (MUTEG) was used.

Lithography is also a common synthesis technique for dimers[107, 108] and short chains.[133] It has the advantage of allowing precise control over particle size and inter-particle separation however, synthesis time is significantly slower than with wet chemistry techniques. It is for this reason that this technique is generally reserved for producing structures that can be compared directly with optical property calculations using DDA[107, 108]

or T-matrix[133] methods in order to gain a better understanding of the fundamental physics associated with dimers and chains.

1.2.6. Gold nanoparticle colloidal crystals

Gold nanoparticle colloidal crystals are long-range ordered superlattices[134] assembled from gold nanoparticles. These structures exhibit an optical response that combines both the size-dependent properties of the individual particles as well as the collective properties from the interactions between them.[135] This enables the optical response of a colloidal crystal to be tuned to a particular wavelength by varying the particle size, shape and inter-particle spacing.

Currently one of the most active areas of research investigates the use of colloidal crystals as optically active substrates for SERS.[7, 136, 137] Upon optical excitation, SERS enhances the Raman scattering cross-section for molecules adsorbed onto the particle surfaces. This is due to the large enhancement of the electric field at the surface of the particle, which can be achieved when the inter-particle spacing is in the near-field regime. These areas are known as 'hot spots' and have potential in biological applications.[136] Wang *et al.*[137] have demonstrated this SERS effect by synthesising superlattices of gold nanoparticles of 50 nm diameter with inter-particle spacings of less than 10 nm. The SERS substrates were formed by allowing a colloidal droplet of CTAB-stabilised gold nanoparticles to dry on an Indium-doped Tin Oxide (ITO) glass substrate. This allowed the formation of a Hexagonally Close-Packed (HCP) monolayer of gold nanoparticle arrays. Qualitative evaluation of the SERS substrate's performance was possible through the use of a non-resonant molecule, p-marcaptoaniline (pMA). Empirical enhancement factors above 1×10^{8} were observed with 785 nm excitation. Moreover, the pMA monolayer can serve as potential cross-linking agents for the attachment of SERS-based recognition molecules.[137]

Considerable effort is currently focused on synthesising colloidal crystals of gold nanoparticles and for larger two- and three-dimensional crystal structures templating[11, 138-141] and self-assembly[9, 142-146] techniques have been reported as successful routes for synthesis. The aim is to produce ordered superlattices, whereby the properties of the lattice can be controlled through variation of the particle size and by the chemical nature of the

ligands used to join the particles. Control over these two parameters allows the formation of highly regular structures with long-range order and periodicity. [147] Recently Chen *et al.*[148] demonstrated precise control over the inter-particle spacing in two-dimensional gold nanoparticle superlattices through variation of the stabilising ligand chain length. Alkanethiolate-stabilised gold nanoparticles were self-assembled into highly ordered two-dimensional structures and the inter-particle spacing was controlled with alkyl chains with lengths ranging between C_{12} (1-dodecanethiolate), C_{14} (1-tetradecanethiolate), C_{16} (1-hexadecanethiolate) to C_{18} (1-octadecanethiolate). Control over the dewetting temperature of the solvent allowed the formation of HCP superlattices with a single domain extending over 1 mm^2 when using the C_{18} chain. The inter-particle spacing l was found to be linearly dependent on the length (nm) of the alkyl chains such that $l = 0.83 + 0.122n$ where n is the number of carbon atoms in the chain. Moreover, inter-particle-spacing-dependent red-shifts of the plasmon resonance were confirmed for different chain lengths.

Colloidal crystals have also been shown to form preferentially using particles with no stabilising agent. In a facile approach Fink *et al.*[147] synthesised naked gold particles with diameters between 3 and 5 nm, which preferentially form two-dimensional superlattices upon evaporation. A phase-transfer reagent of quaternary ammonium bromide salt ($R_4N^+Br^-$) is adsorbed onto the particles during synthesis forming surface ion pairs, which provides particle stabilisation. Fink *et al.*[147] propose that the formation of the superlattices is due to the presence of ionic dipoles on the gold particles.

Three-dimensional colloidal crystals have also been produced by many groups. Indeed Yao *et al.*[149] have produced structures containing five-fold symmetry through the use of N-acetylglutathion (NAG) protected gold particles. The use of NAG as a capping agent allows the formation of the superlattices through hydrogen bonding between carboxylic acid molecules. These hydrophilic particles form colloidal crystals at an air/water interface through the addition of concentrated hydrochloric acid. Pentagonal rod, decahedron and icosahedron structures were formed using this technique. Using a similar technique Nishida *et al.*[150] have prepared fluorescent micron-sized three-dimensional colloidal crystals from hydrophilic gold nanoparticles of 3 nm diameter functionalised with a fluorescein label. The synthesis of fluorescent gold nanoparticle colloidal crystals is also important for biological applications. The colloidal crystals form at an air/water interface

under highly acidic conditions. The particles form superlattices through hydrogen bonding of the mercaptosuccinic acid (MSA)-protected gold particles.

Nykypanchuk *et al.*[151] and Park *et al.*[152] use DNA-functionalised gold nanoparticles to synthesise colloidal crystal structures. Park *et al.*[152] synthesised FCC and BCC crystal structures through the functionalisation of 15 nm diameter gold nanoparticles with DNA. The gold nanoparticle-DNA conjugates could be assembled into different crystal structures (FCC or BCC) by changing the sequence of the DNA linkers.

Recently Zheng *et al.*[153] developed a very simple technique to synthesise micron-sized three dimensional gold nanoparticle colloidal crystals. Dodecanethiol-capped gold nanoparticles of approximately 6 nm in diameter were prepared and a carbon-coated copper Transmission Electron Microscope (TEM) grid was dipped into the solution and allowed to dry over two hours. Two-dimensional long-range ordered superlattices were formed using this approach. To make larger three-dimensional colloidal crystals the TEM grid was immersed in the colloid, sealed and cooled for two days, whereupon tens-of-microns sized colloidal crystals were produced with FCC structure and a lattice constant of 11.3 nm. Zheng *et al.*[153] report that crystallisation is achieved through cooling of the colloid or by diffusing a polar solvent into the mixture.

In a very simple method Compton and Osterloh[154] form colloidal crystals using a two-step nucleation process whereby disordered gold nanoparticle aggregates are initially formed followed by the ordering process, which is driven by a lowering of the free energy associated with the structure. The gold nanoparticle aggregate clusters were made by adding dodecanethiol to a solution of oleylamine-stabilised nanoparticles in chloroform. The dodecanethiol displaces the amine and initiates aggregation because the length of the thiol is shorter than that of the amine and is less soluble in chloroform. Klajn *et al.*[155, 156] have extended this technique to allow light-induced assembly of gold nanoparticle colloidal crystals. Dithiol ligands were attached to the surface of the gold nanoparticles and photoisomerisation of these ligands allowed light-induced self-assembly of the aggregate clusters into three-dimensional micron-sized colloidal crystals and vice versa. The application or removal of UV irradiation had the effect of either increasing or decreasing

the nanoparticle binding energies sufficiently to allow the formation of crystals or aggregate clusters.

Chapter 2

2. Theory

This chapter is dedicated to the description of the mathematical basis behind the different techniques used to calculate the optical properties of geometrically varying nanoparticles and structures. Invariably the choice of technique is determined by the shape of the nanoparticle with spherically symmetrical particles such as spheres, coated spheres (shells) and small ellipsoids allowing analytical solutions while numerical techniques, often based on the DDA, are employed for those particles that are not spherically symmetrical such as hemispherically capped rods. Within this thesis both analytical and numerical techniques have been employed and table 1 names the techniques used for the varying particle geometries.

Nanoparticle Geometry	Mathematical Technique
Spheres	Mie theory[68], analytical solution
Coated spheres or shells	Mie theory[68], analytical solution
Small ellipsoids (prolate spheroids)	Gans theory[24], analytical solution
Hemispherically capped rods	DDA (DDSCAT)[157], numerical solution
Chains or clusters of spheres	T-matrix[158, 159], analytical solution

Table 2.1. Description of the different mathematical techniques employed to calculate the optical response of varying geometry particles.

Section 2.1 and 2.2 will describe the mathematical basis of Mie and Gans theory, respectively. Section 2.3 will focus on the DDSCAT software package that was used to implement the DDA technique when modelling hemispherically capped rods. Finally, the T-matrix technique for fixed and orientationally averaged radiation will be discussed in section 2.4.

2.1. Mie Theory

In 1908 Gustav Mie[68] described an analytical solution to Maxwell's equations for the scattering of electromagnetic radiation from a homogeneous sphere of arbitrary radius and refractive index. This solution has become widely known as Mie theory and has been further modified to allow calculation of scattering from other particles such as shells, small ellipses and infinite cylinders.

2.1.1. Spheres

The mathematical basis of Mie theory for a sphere forms an integral part of the shell solution and the T-matrix formalism. The aim is to calculate the amount of light scattered and absorbed by a homogeneous, isotropic sphere of radius a from an incident plane polarised wave which is written in spherical coordinates as[13]

$$\mathbf{E}_i = E_o e^{ikr\cos\theta}\,\hat{\mathbf{e}} \qquad 2.1$$

where E_o is the amplitude of the incident wave, k is the wavenumber, $k = \frac{2\pi N}{\lambda}$ with N the refractive index $(n + ik)$ of the background medium, which is assumed to be constant and non-absorbing, λ is the wavelength and $\hat{\mathbf{e}}$ depends upon the spherical polar coordinates r, θ and ϕ such that[13]

$$\hat{\mathbf{e}} = \sin\theta\cos\phi\,\hat{\mathbf{e}}_r + \cos\theta\cos\phi\,\hat{\mathbf{e}}_\theta - \sin\phi\,\hat{\mathbf{e}}_\phi \qquad 2.2$$

Expanding the incident plane wave, equation 2.1, in vector spherical harmonics gives[13]

$$\mathbf{E}_i = E_o \sum_{n=1}^{\infty} i^n \frac{2n+1}{n(n+1)} \left(\mathbf{M}^1_{o\ln} - i\mathbf{N}^1_{e\ln} \right) \qquad 2.3$$

where **M** and **N** are the vector spherical harmonics, e and o indicate even and odd polarisation, $-n \le l \le n$ and n is the number of multipole orders. Where $n = 1, 2, 3.....$ correspond to the dipole, quadrupole and octupole terms, respectively.

As the incident field has been expanded as an infinite series of vector spherical harmonics, equation 2.3, the same can be done to the scattered field as per

$$\mathbf{E}_s = \sum_{n=1}^{\infty} E_n \left(i a_n \mathbf{N}^3_{e\ln} - b_n \mathbf{M}^3_{o\ln} \right) \qquad 2.4$$

where E_n can be defined by

$$E_n = \frac{i^n E_0 (2n+1)}{n(n+1)} \qquad 2.5$$

The incident wave excites partial oscillations of the free electrons within the sphere. These partial oscillations and their associated fields are commonly described as the scattering coefficients a_n and b_n of the sphere.[160] Where a_n describes the amplitude of the magnetic oscillations and b_n describes the amplitude of the electric oscillations such that

$$a_n = \frac{m\psi_n(mx)\psi_n'(x) - \psi_n(x)\psi_n'(mx)}{m\psi_n(mx)\xi_n'(x) - \xi_n(x)\psi_n'(mx)} \qquad 2.6$$

$$b_n = \frac{\psi_n(mx)\psi_n'(x) - m\psi_n(x)\psi_n'(mx)}{\psi_n(mx)\xi_n'(x) - m\xi_n(x)\psi_n'(mx)} \qquad 2.7$$

where x is the size parameter, $x = ka = \frac{2\pi Na}{\lambda}$ and $m = \frac{k_1}{k} = \frac{N_1}{N}$ with N_1 is the refractive index of the particle.

Equations 2.6 and 2.7 can be solved by using the nth order Ricatti-Bessel functions, $\psi_n(\rho)$ and $\xi_n(\rho)$

$$\psi_n(\rho) = \rho j_n(\rho) \tag{2.8}$$

$$\xi_n(\rho) = \rho h_n^1(\rho) \tag{2.9}$$

with the prime indicating the derivative with respect to the argument and $\psi_n'(\rho)$ and $\xi_n'(\rho)$ satisfy the recurrence relations

$$\psi_n'(\rho) = \psi_{n-1}(\rho) - \frac{n\psi_n(\rho)}{\rho} \tag{2.10}$$

$$\xi_n'(\rho) = \xi_{n-1}(\rho) - \frac{n\xi_n(\rho)}{\rho} \tag{2.11}$$

where ρ is either mx or x and it is assumed that the magnetic permeability of the sphere, μ_1 and the surrounding medium, μ is equal to 1. The standard Bessel functions are related to the spherical Bessel functions by[13]

$$j_n(p) = \sqrt{\frac{\pi}{2\rho}} J_{n+\frac{1}{2}}(\rho) \tag{2.12}$$

$$y_n(p) = \sqrt{\frac{\pi}{2\rho}} Y_{n+\frac{1}{2}}(p) \tag{2.13}$$

Once the scattering coefficients a_n and b_n are known it is possible to calculate measurable quantities associated with extinction and scattering from a sphere. These include particle scattering C_{sca} and extinction C_{ext} cross-sections, which can be calculated using[13]

$$C_{sca} = \frac{2\pi}{k^2} \sum_{n=1}^{\infty} (2n+1)(|a_n|^2 + |b_n|^2) \tag{2.14}$$

$$C_{ext} = \frac{2\pi}{k^2} \sum_{n=1}^{\infty} (2n+1)\,\mathrm{Re}\{a_n + b_n\} \tag{2.15}$$

The absorption cross-section is defined as $C_{abs} = C_{ext} - C_{sca}$.

Generally the calculated cross-sections are normalised to the cross-sectional area such that $Q = \frac{C}{\pi a^2}$. These quantities are known as efficiencies and they provide an effective parameter against which different sized particles can be compared. If, for example a calculated efficiency such as Q_{abs} is greater than 1, the amount of light absorbed by the particle is larger than the particle geometrical cross-section presented to the incident light.

Noble metal spherical particles have the ability to absorb light strongly at visible wavelengths. The conditions required for such strong absorption can be easily understood if we examine the particle within the quasi-static regime. That is where the particle is considered to be small enough when compared to the incident wavelength, with $a << \lambda$, so as to enable the incident field within and surrounding the particle to be treated as static. In this regime phase retardation and contributions from higher order modes are neglected and equation 2.15 can be simplified to contain only the dipole mode and becomes[14]

$$C_{ext} = \frac{24\pi^2 a^3 \varepsilon^{\frac{2}{3}}}{\lambda} \frac{\varepsilon''}{\left[\varepsilon' + 2\varepsilon_m\right]^2 + \varepsilon''^2} \qquad 2.16$$

where the dielectric constant of the sphere, $\varepsilon = \varepsilon' + i\varepsilon''$ and ε_m is the dielectric constant of the surrounding medium, which is assumed to be constant and non-absorbing.

Equation 2.16 shows that the resonance peak position occurs when $\left[\varepsilon' + 2\varepsilon_m\right]^2 + \varepsilon''^2 = 0$. So providing ε'' is small resonance occurs when $\varepsilon' = -2\varepsilon_m$. This happens in the visible regime for gold spheres in vacuum. Equation 2.16 considers only the dipole approximation and therefore the resonance peak position, for all metals, is considered to be independent of particle size. This is true for metals such as gold and silver, however not quite correct for a metal such as potassium.[20]

A correction term has been derived from Mie theory that describes the shift in the resonance as a function of particle size and dielectric function[20]

$$\varepsilon' = -2\varepsilon_m \left(\frac{-12}{5} \right) \frac{4\pi^2 a^2 \varepsilon_m^2}{\lambda^2} \qquad 2.17$$

Equation 2.17 was derived by expanding j_n and y_n as a power series and retaining several terms. If the derivative of equation 2.17 is taken and the constants removed then an expression is obtained which describes the plasmon resonance shift with particle size and the gradient of the dielectric function[20]

$$\frac{\delta\lambda}{\delta a} \propto \frac{-\delta\lambda}{\delta\varepsilon'} = \frac{-1}{\frac{\delta\varepsilon'}{\delta\lambda}} \qquad 2.18$$

Equation 2.18 shows that the magnitude of the plasmon position for a given radius is inversely proportional to the gradient of the real part of the dielectric function around $\varepsilon' = -2\varepsilon_m$.

For gold the gradient of the dielectric function $\varepsilon' = -2\varepsilon_m$ is quite steep (-65 μm^{-1}) and as such the plasmon peak position does not shift greatly, only 8 nm, as the particle radius is increased from 20 to 40 nm.[20] Whereas the dielectric function of a metal such as potassium has a very flat gradient around $\varepsilon' = -2\varepsilon_m$ (-10 μm^{-1}) and as such the plasmon peak position shifts a total of 33 nm as the particle radius is increased from 20 to 40 nm as shown in figure 2.1.[20]

Therefore, the minimal shift in the plasmon peak position with increasing particle radius for gold spheres is coincidental and not because the quasi-static regime is appropriate in this size regime.

However, all of the work described within this thesis is based on either gold or silver particles and the applicability of the quasi-static regime, fortuitous though it may be, is nevertheless a convenient way to describe the mathematical formalism underlying plasmon resonance production for several different shaped particles and will continue to be used in the following sections for shells and ellipsoids.

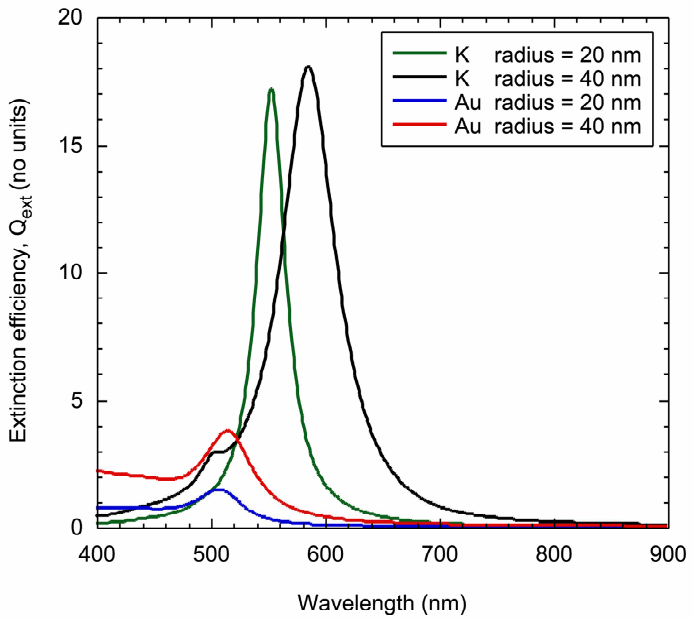

Figure 2.1. Plasmon peak position shift with increasing radii for gold and potassium spheres.

2.1.2. Coated spheres or shells

The solution to the scattering problem for a sphere with a concentric spherical shell, henceforth to be referred to as a shell, was first proposed by Aden and Kerker.[21] The mathematical basis of which is the same as the scattering from a sphere, however in this case the scattering coefficients a_n and b_n depend upon the constituent refractive indices of the core and shell.

Therefore if the same plane polarised plane wave described by equation 2.3 is incident on the shell of inner radius a and outer radius b and the scattered field is described by equation 2.4 then a_n and b_n can be calculated using[13]

$$a_n = \frac{\psi_n(y)[\psi_n'(m_2 y) - A_n\chi_n'(m_2 y)] - m_2\psi_n'(y)[\psi_n(m_2 y) - A_n\chi_n(m_2 y)]}{\xi_n(y)[\psi_n'(m_2 y) - A_n\chi_n'(m_2 y)] - m_2\xi_n'(y)[\psi_n(m_2 y) - A_n\chi_n(m_2 y)]} \qquad 2.19$$

$$b_n = \frac{m_2\psi_n(y)[\psi_n'(m_2 y) - B_n\chi_n'(m_2 y)] - \psi_n'(y)[\psi_n(m_2 y) - B_n\chi_n(m_2 y)]}{m_2\xi_n(y)[\psi_n'(m_2 y) - B_n\chi_n'(m_2 y)] - \xi_n'(y)[\psi_n(m_2 y) - B_n\chi_n(m_2 y)]} \qquad 2.20$$

where $x = ka$, $y = kb$ with m_1 and m_2 are the refractive indices of the core and coating relative to the surrounding medium and the Riccati-Bessel function $\chi_n(z)$ is $-zy_n(z)$ and $\chi_n'(z)$ is the derivative with respect to the argument. As was the case with the sphere $\mu = \mu_1 = \mu_2 = 1$, where μ_2 is the shell permeability and[13]

$$A_n = \frac{m_2\psi_n(m_2x)\psi_n'(m_1x) - m_1\psi_n'(m_2x)\psi_n(m_1x)}{m_2\chi_n(m_2x)\psi_n'(m_1x) - m_1\chi_n'(m_2x)\psi_n(m_1x)} \quad 2.21$$

$$B_n = \frac{m_2\psi_n(m_1x)\psi_n'(m_2x) - m_1\psi_n(m_2x)\psi_n'(m_1x)}{m_2\chi_n'(m_2x)\psi_n(m_1x) - m_1\psi_n'(m_1x)\chi_n(m_2x)} \quad 2.22$$

In a similar vein to the problem of scattering from a sphere once a_n and b_n are known equations 2.14 and 2.15 can be used to calculate the scattering and extinction cross-sections of the shell, respectively.

Section 2.1.1 described the impressive ability of spheres to absorb light strongly in the visible regime. As described within Chapter 1 the attractiveness of shells lies in the ability to tune their plasmonic response into the infrared regime by varying the shell aspect ratio. To demonstrate mathematically how this is achieved it is once again necessary to consider the shell within the quasi-static regime.

In this regime the extinction cross-section can be calculated from[13]

$$C_{ext} = k\,\mathrm{Im}(\alpha) \quad 2.23$$

where $\mathrm{Im}(\alpha)$ is the complex polarisability of the particle.

The polarisability of a small shell can be described by[13]

$$\alpha = 4\pi b^3 \frac{(\varepsilon_2 - \varepsilon_m)(\varepsilon_1 + 2\varepsilon_2) + f(\varepsilon_1 - \varepsilon_2)(\varepsilon_m + 2\varepsilon_2)}{(\varepsilon_2 + 2\varepsilon_m)(\varepsilon_1 + 2\varepsilon_2) + f(2\varepsilon_2 - 2\varepsilon_m)(\varepsilon_1 - \varepsilon_2)} \quad 2.24$$

where ε_1, ε_2, ε_m are the dielectric functions of the inner core, outer core and surrounding medium, respectively and f is the fraction of the total particle volume occupied by the

core, that is, $f = \left(\frac{a}{b}\right)^3$. The exact position of the maximum absorption peak within the spectrum is determined by the dielectric functions of the shell and surrounding medium.

Equation 2.24 shows that the plasmon peak position occurs when

$$(\varepsilon_2 + 2\varepsilon_m)(\varepsilon_1 + 2\varepsilon_2) + f(2\varepsilon_2 - 2\varepsilon_m)(\varepsilon_1 - \varepsilon_2) = 0 \qquad 2.25$$

If it is assumed that the dielectric function of the surrounding medium is unity, it is possible to write a simple expression for the resonance condition

$$\varepsilon_1 = -2\varepsilon_2\left[\frac{\varepsilon_2(1-f)+(2+f)}{\varepsilon_2(2f+1)+2(1-f)}\right] \qquad 2.26$$

From equation 2.26 it can be seen that the magnitude and position of the plasmon peak within the spectra can be varied by simply varying the aspect ratio and/or the dielectric constant of the core, shell and/or the surrounding medium.

2.2. Gans Theory

2.2.1. Ellipsoids

Section 2.1.2 demonstrated the optically active nature of shells. Rods provide an alternative to shells for achieving a tuneable plasmon response. Unfortunately, however there is no general analytical solution which describes the optical properties of rods. Nevertheless it is common to consider rods as ellipsoids (prolate spheroids) and then model their optical properties using Gans theory.[24]

The possibilities of ellipsoidal nanoparticles were first recognized by Gans[24] in 1912 when he provided an analytical solution for the depolarisation factor for ellipsoids of arbitrary aspect ratio. His theory predicted that the surface plasmon will split into two modes (longitudinal and transverse) as the aspect ratio of the ellipsoid is increased, with the

longitudinal plasmon mode red-shifting significantly and the transverse plasmon blue-shifting slightly.

Synthesised rods are more like hemispherically-capped, right cylinders, or dumbbell shaped[161] and it has been recently found that the end-cap geometry has significant effects on the calculated position of the surface plasmon mode.[162, 163] In section 2.3 DDA will be described as this technique was used to model the optical properties of rods with hemispherically-capped, right cylinder geometries. Nevertheless, the origins of the mode splitting and dependence on aspect ratio may be understood by consideration of the Gans model, which will be described in the quasi-static regime.

The polarisability of an ellipsoid can be described by[13]

$$\alpha_{x,y,z} = 4\pi abc \frac{\varepsilon_1 - \varepsilon_m}{3\varepsilon_m + 3L_{1,2,3}(\varepsilon_1 - \varepsilon_m)} \qquad 2.27$$

where a is the length of the longitudinal axis and b and c correspond to the length of the shorter axes. ε_1, ε_m are the dielectric functions of the spheroid and surrounding medium, respectively and $L_{1,2,3}$ are the geometrical factors. For the ellipsoid where a is the longer axis, $b = c$, $L_2 = L_3$ and the applied electric field is parallel to the x-axis, equation 2.27 becomes

$$\alpha_x = 4\pi abc \frac{\varepsilon_1 - \varepsilon_m}{3\varepsilon_m + 3L_1(\varepsilon_1 - \varepsilon_m)} \qquad 2.28$$

As was the case with the optical response of the shells, the excitation of the plasmon mode follows by setting the denominator of equation 2.28 equal to zero

$$3\varepsilon_m + 3L_1(\varepsilon_1 - \varepsilon_m) = 0 \qquad 2.29$$

This condition is met when

$$\varepsilon_1 = \varepsilon_m \left(1 - \frac{1}{L_1}\right) \qquad 2.30$$

where L_1 is

$$L_1 = \frac{1-e^2}{e^2}\left(-1+\frac{1}{2e}\ln\frac{1+e}{1-e}\right) \qquad 2.31$$

where e is the eccentricity of the ellipse, which is described by $e^2 = 1-(\frac{b}{a})^2$. The ellipse polarisability is, once again, directly related to the extinction cross section C_{ext} by equation 2.23.

From equation 2.30 it can be seen that the magnitude and position of the plasmon peak within the spectra can be varied by simply varying the aspect ratio and/or the dielectric constant of the ellipsoid and/or the surrounding medium.

2.3. Discrete Dipole Approximation (DDA)

While analytical solutions for the optical properties of metal spheres, shells and small ellipsoids are available, there is no generally applicable analytical solution for arbitrary-shaped nanoparticles such as hemispherically-capped rods and it is therefore necessary to resort to numerical calculations based on the DDA.[164-166]

DDA was first developed in 1973 by Purcell and Pennypacker[167] as a numerical technique to calculate the absorption and scattering of electromagnetic radiation from arbitrary shaped targets. This technique is relatively popular based largely on its ease of use and free availability in software packages such as DDSCAT.[157]

The DDA technique represents the target by an array of N dipoles within a cubic grid as shown in figure 2.1. It then calculates the polarisability, α_i of each dipole based upon the dipole dielectric properties and position within the target r_i. After the dipole polarisabilities have been calculated it is then possible to calculate the target absorption C_{abs} and scattering, C_{sca} cross-sections as detailed below.[96, 164, 168-170]

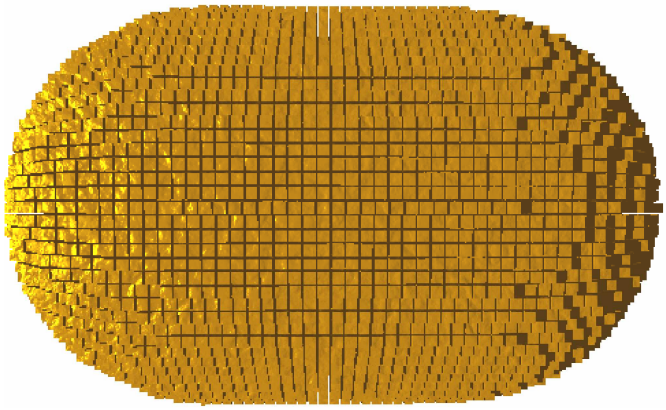

Figure 2.2. A hemispherically-capped rod represented by an array of dipoles in a cubic lattice.

If the index $i = 1,.....N$ represents each dipole within a cubic lattice then the instantaneous dipole moment, P_i is[96]

$$P_i = \alpha_i . E_{loc,i} \qquad 2.32$$

where α_i is the dipole polarisability tensor and the electric field $E_{loc,i}$ is the sum of the incident electric field $E_{inc(r_i,t)}$ and the radiated electric field $E_{dip,i}$ from the surrounding $N-1$ dipoles[96]

$$E_{loc,i} = E_{inc(r_i,t)} + E_{dip,i} \qquad 2.33$$

with

$$E_{inc(r_i,t)} = E_o e^{i(kr_i - \omega t)} \qquad 2.34$$

where E_o is the amplitude of the electric field, k is the wavenumber, r_i is the position vector, ω is the angular frequency and t is time.

Equation 2.35 represents the contribution to the incident electric field made by the radiated electric field from dipole P_j at position r_j within the $3N \times 3N$ matrix A_{ij}[168]

$$E_{dip,i} = \sum_{j \neq i} A_{ij} . P_j \qquad 2.35$$

$$\therefore E_{loc,i} = E_o e^{i(kr_i - \omega t)} - \sum_{j \neq i} A_{ij} . P_j \qquad 2.36$$

Each element A_{ij} is defined by the equation for an electric field from a radiating or oscillating dipole[96, 168]

$$A_{ij} . P_j = \frac{e^{ikr_{ij}}}{r_{ij}^3} \left\{ k^2 r_{ij} \times (r_{ij} \times P_j) + \frac{(1 - ikr_{ij})}{r_{ij}^2} [r_{ij}^2 P_j - 3 r_{ij} (r_{ij} . P_j)] \right\} \qquad 2.37$$

where $i \neq j$.

Substituting equation 2.36 into 2.32 and simplifying to find $E_{inc(r_i,t)}$ gives a set of $3N$ linear equations[168]

$$E_{inc(r_i,t)} = \frac{P_i}{\alpha_i} + \sum_{j \neq i} A_{ij} . P_j \qquad 2.38$$

DDSCAT version 6.1 developed by Draine and Flatau[157] was used for the entire set of nanorod calculations presented in Chapter 6. The Parallel Iterative Methods (PIM)[157] package within DDSCAT uses iteration of the Preconditioned BiConjugate Gradient with Stabilisation (PBCGST) algorithm to solve equation 2.38 for P_i. Once P_i is known C_{abs} and C_{sca} can be calculated from equations 2.39[96] and 2.40[164], respectively.

$$C_{abs} = \frac{4\pi k}{|E_{inc}|^2} . \sum_{i=1}^{N} \left\{ \mathrm{Im}[P_i . (\alpha_i^{-1})^* P_i^*] - \frac{2}{3} k^3 |P_i|^2 \right\} \qquad 2.39$$

$$C_{ext} = \frac{4\pi k}{|E_{inc}|^2} . \sum_{i=1}^{N} \mathrm{Im}(E_{inc,i}^* . P_i) \qquad 2.40$$

In the first implementation of DDA the Clausius-Mossotti-Relation (CMR)[169] was used to calculate the dipole polarisabilities based upon the complex part of the refractive index *m* such that

$$\alpha_{CMR} = \frac{3d^3}{4\pi}\left(\frac{m^2 - 1}{m^2 + 2}\right) \qquad 2.41$$

where d is the inter-dipole spacing. This approach is exact in the quasi-static regime however, it is not exact at finite wavelengths because equation 2.41 does not consider radiative reaction.

In 1993 Draine[165] introduced the Lattice-Dispersion-Relation (LDR) which required that the polarisability of dipoles on an infinite lattice give the same dispersion relation as a continuum medium.[169] In the LDR approach, the radiative reaction correction occurs naturally and the polarisability is given by

$$\alpha_{LDR} = \frac{\alpha_{CMR}}{1 + (\frac{\alpha_{CMR}}{d^3})[(b_1 + m^2 b_2 + m^2 b_3 S)(kd)^2 - (\frac{2}{3})i(kd)^3]} \qquad 2.42$$

where $b_1 = -1.8915316$, $b_2 = 0.1648469$, $b_3 = -1.7700004$ and $S = \sum_j (a_j e_j)^2$ with a and e the unit and polarisation vectors, respectively and the directions $j = 1, 2, 3$ corresponding to the dipole lattice axes.

Unfortunately however, the accuracy of the polarisabilities calculated from equation 2.42 decrease for two reasons, both of which require corrections. The first correction must be applied for finite wavelength errors, these occur because $kd \to 0$ is never true. Secondly, local field effects must be corrected. Local field effects arise in the quasi-static regime when a static electric field is applied to a collection of dipoles and each dipole will have an induced polarisability, which will depend upon the applied field as well as the field from all of the other induced dipoles. This means that all dipoles will not have the same effective polarisability.[171] The local field effect is amplified for fine dipole lattice discretisations and these are necessary when the imaginary part of the refractive index is

≥ 2 as is the case for large aspect ratio rods when the plasmon peak position is in the infrared regime.

In 2004 Collinge[169] developed the Surface-Corrected-Lattice-Dispersion-Relationship (SCLDR) which is a modified version of the LDR which accounts for both finite wavelengths and local field effects. Unfortunately, the SCLDR can only be applied to targets with an analytical solution in the electrostatic limit.[171] As such SCLDR could not be used for the hemispherically capped nanorod calculations.

Consequently the only way to ensure the accuracy of the DDA technique is to increase the number of dipoles to such a point where the results converge. When using DDSCAT[157] the authors recommend that the inter-dipole spacing d be small compared to any structural lengths in the target and the wavelength λ of the incident light. The second criteria is satisfied with a high degree of accuracy if $|m|kd < 0.5$. The difficulty here is that as the number of dipoles within the target increases so does the computational time. So a compromise must be met between calculation accuracy and computational expense. Convergence was confirmed for the nanorod calculations presented in Chapter 6 and it was found that an inter-dipole spacing of approximately 1 nm was sufficient for convergence. The use of the non-surface corrected LDR causes DDSCAT to slightly underestimate absorption efficiencies, however since large absorption efficiencies are sought, an underestimation is less problematic than an overestimation.

DDSCAT was considered for modelling dimers of gold spherical particles however, it became problematic when trying to use enough dipoles to adequately resolve the inhomogeneous electric fields between particles when the inter-particle spacing was small. Figure 2.3 shows the extinction efficiencies calculated using both the DDA and T-matrix technique for a dimer containing 12 nm diameter particles with an inter-particle spacing of 1 nm. Extinction was calculated with light polarised parallel to the dimer axis and the wavevector perpendicular to the dimer axis. The number of dipoles used to represent the 1 nm inter-particle gap was increased from two to six and it can be seen from figure 2.3 that the results do not converge with that of the T-matrix.

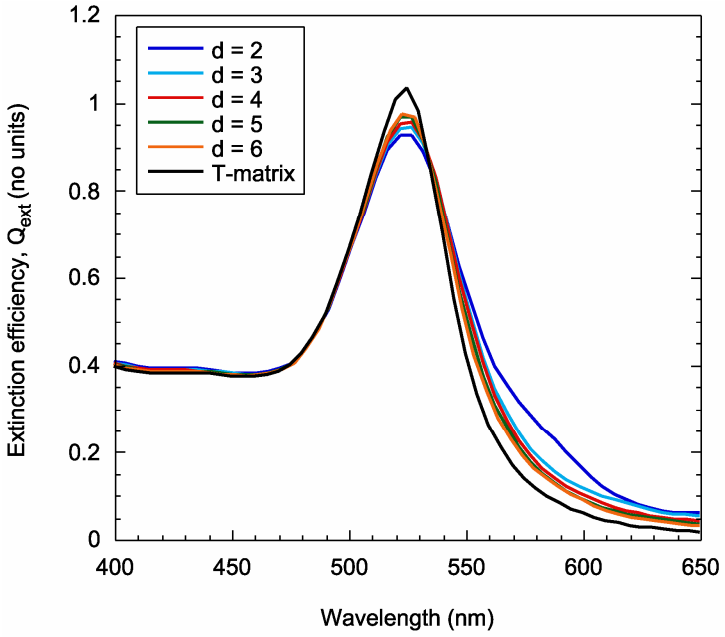

Figure 2.3. Extinction efficiency calculations using both DDSCAT and the T-matrix technique for a dimer of 12 nm diameter spherical gold particles with an inter-particle spacing of 1 nm. The DDSCAT calculations were performed with increasing numbers of dipoles d .

Moreover, the time taken for the DDA calculation containing six dipoles in the inter-particle gap was approximately 141 hours, whereas the T-matrix calculation was completed in just over 3 seconds. Both of these calculations were performed between the wavelengths of 400 and 700 nm in 5 nm steps. Therefore, the T-matrix technique was implemented to model the optical response of dimers, chains and three-dimensional structures of spherical particles, the mathematical basis of which is outlined in the following section.

2.4. T-matrix

The T-matrix technique provides an analytical solution to the scattering problem from a cluster of spheres. The T-matrix code developed by Mackowski *et al.*[158, 159] was used to calculate the scattering properties of a cluster with a finite number of gold particles for both fixed and orientationally averaged incident radiation.

The T-matrix technique calculates the scattered field from the cluster as a superposition[172] of the individual fields scattered from each of the spheres within the cluster. The individual fields scattered from the spheres are expressed in terms of vector spherical harmonics and with the use of addition theorems, where the vector spherical harmonic about one origin can be expressed as vector spherical harmonics about another origin, a set of equations for the scattered-field expansion coefficients for the entire cluster are created.[158]

The scattered field from a cluster of spheres $\mathbf{E}_s$ is represented by the superposition of the scattered fields from each of the spheres within the cluster[158, 159]

$$\mathbf{E}_s = \sum_{i=1}^{Ns} \mathbf{E}_{i,s} \tag{2.43}$$

where N_s is the number of spheres within the cluster.

The scattered field from an individual sphere within the cluster is represented by an expansion of vector spherical harmonics written about the origin of the *ith* sphere as

$$\mathbf{E}_{i,s} = \sum_{n=1}^{\infty} \sum_{m=-n}^{n} \left[a_{mn}^{i} \mathbf{N}_{mn}^{(3)}\left(kr^{i}, \theta^{i}, \phi^{i}\right) + b_{mn}^{i} \mathbf{M}_{mn}^{(3)}\left(kr^{i}, \theta^{i}, \phi^{i}\right) \right] \tag{2.44}$$

where k is the wavenumber and a_{mn}^{i} and b_{mn}^{i} are the expansion coefficients and $\mathbf{N}_{mn}^{(3)}$ and $\mathbf{M}_{mn}^{(3)}$ are vector harmonics. The superscript (3) denotes spherical Hankel functions. Boundary conditions for the electric and magnetic fields at the surface of each sphere in the cluster must be applied in order to calculate a_{mn}^{i} and b_{mn}^{i}.

The field at the surface of the *ith* sphere is a combination of the incident field expressed as

$$\mathbf{E}_{i,0} = -\sum_{n=1}^{\infty} \sum_{m=-n}^{n} \left[p_{mn}^{i} \mathbf{N}_{mn}^{(1)}\left(kr^{i}, \theta^{i}, \phi^{i}\right) + q_{mn}^{i} \mathbf{M}_{mn}^{(1)}\left(kr^{i}, \theta^{i}, \phi^{i}\right) \right] \tag{2.45}$$

and the scattered field from the other spheres within the cluster. The coefficients p_{mn}^{i} and q_{mn}^{i} are determined from the propagation direction and the polarisability of the incident field.

The scattered radiation from the remaining $N_s - 1$ spheres must be incorporated into the boundary conditions. To do this the scattered field expansions must be rewritten in terms of vector harmonics about the origin of the *ith* sphere. To do this addition theorems must be employed.

When $r^i < R^{ij}$, where R^{ij} is the centre-to-centre distance from the sphere j to sphere i the addition theorem is

$$\mathbf{M}_{mn}^{(3)}(kr^j,\theta^j,\phi^j) = \sum_{l=1}^{\infty}\sum_{k=-l}^{l}\begin{bmatrix} A_{mnkl}^{(3)}\left(kR^{ij},\Theta^{ij},\Phi^{ij}\right)\mathbf{M}_{kl}^{(1)}\left(kr^i,\theta^i,\phi^i\right) \\ + B_{mnkl}^{(3)}\left(kR^{ij},\Theta^{ij},\Phi^{ij}\right)\mathbf{N}_{kl}^{(1)}\left(kr^i,\theta^i,\phi^i\right)\end{bmatrix} \qquad 2.46$$

$$\mathbf{N}_{mn}^{(3)}(kr^j,\theta^j,\phi^j) = \sum_{l=1}^{\infty}\sum_{k=-l}^{l}\begin{bmatrix} A_{mnkl}^{(3)}\left(kR^{ij},\Theta^{ij},\Phi^{ij}\right)\mathbf{N}_{kl}^{(1)}\left(kr^i,\theta^i,\phi^i\right) \\ + B_{mnkl}^{(3)}\left(kR^{ij},\Theta^{ij},\Phi^{ij}\right)\mathbf{M}_{kl}^{(1)}\left(kr^i,\theta^i,\phi^i\right)\end{bmatrix} \qquad 2.47$$

A and B are the addition coefficients which depend entirely on the distance and direction between spheres j and i from $kR^{ij},\Theta^{ij},\Phi^{ij}$.

Therefore, through the use of addition theorems the interacting scattered fields are transformed into expansions about the origin of the *ith* sphere, allowing analytical formulation of the boundary conditions at the surface of that sphere.

From this a system of equations for the scattered coefficients are created

$$a_{mn}^{i} = \bar{a}_n^i\left\{p_{mn}^{i} - \sum_{\substack{j=1\\ j\neq i}}^{N_s}\sum_{l=1}^{N_t^j}\sum_{k=-l}^{l}\left[A_{klmn}^{(3)}\left(kR^{ij},\Theta^{ij},\Phi^{ij}\right)a_{kl}^{j} + B_{klmn}^{(3)}(kR^{ij},\Theta^{ij},\Phi^{ij})b_{kl}^{j}\right]\right\} \qquad 2.48$$

$$b_{mn}^{i} = \bar{b}_n^i\left\{q_{mn}^{i} - \sum_{\substack{j=1\\ j\neq i}}^{N_s}\sum_{l=1}^{N_t^j}\sum_{k=-l}^{l}\left[A_{klmn}^{(3)}\left(kR^{ij},\Theta^{ij},\Phi^{ij}\right)b_{kl}^{j} + B_{klmn}^{(3)}(kR^{ij},\Theta^{ij},\Phi^{ij})a_{kl}^{j}\right]\right\} \qquad 2.49$$

where $\bar{a}_n^i$ and $\bar{b}_n^i$ are the scattering coefficients from equations 2.6 and 2.7, respectively.

Equations 2.48 and 2.49[158] can be combined into

$$\mathbf{a}_{mnp}^{i} + \bar{\mathbf{a}}_{np}^{i} \sum_{\substack{j=1 \\ j \neq 1}}^{Ns} \sum_{l=1}^{No,i} \sum_{k=-l}^{l} \sum_{q=1}^{2} H_{mnpklq}^{ij} \mathbf{a}_{klq}^{j} = \bar{\mathbf{a}}_{np}^{i} \mathbf{p}_{mnp}^{i} \qquad 2.50$$

where H^{ij} is the matrix formed from the vector harmonic addition coefficients (using Hankel functions) based on the distance and direction of the translation from origin j to i with elements given by

$$H_{mn1kl1}^{ij} = H_{mn2kl2}^{ij} = A_{klmn}^{(3)}\left(kR^{ij}, \Theta^{ij}, \Phi^{ij}\right) \qquad 2.51$$

$$H_{mn1kl2}^{ij} = H_{mn2kl1}^{ij} = B_{klmn}^{(3)}\left(kR^{ij}, \Theta^{ij}, \Phi^{ij}\right) \qquad 2.52$$

Inversion of equation 2.50 leads to

$$\mathbf{a}_{mnp}^{i} = \sum_{j=1}^{Ns} \sum_{l=1}^{No,i} \sum_{k=-l}^{l} \sum_{q=1}^{2} T_{mnpklq}^{ij} \mathbf{p}_{klq}^{j} \qquad 2.53$$

where N_0 are the number of expansion orders, $\mathbf{p}^j$ denote the expansion coefficients for the plane, linearly polarised incident wave at the origin of the *ith* sphere and the T-matrix T_{mnpklq}^{ij} represents the scattered fields from each sphere within the cluster. To calculate the scattered field from the entire cluster the superimposed fields from the cluster need to be transformed into a single field based upon a single coordinate origin.

The expansion coefficients for the incident field $\mathbf{p}^i$ at the origin of the *ith* sphere can be obtained by translating the incident-field coefficients expanded about the cluster origin $\mathbf{p}^i$ to the origin of the *ith* sphere through:

$$\mathbf{p}_{mnp}^{i} = J_{mnpklq}^{iO} \mathbf{p}_{klq}^{O} \qquad 2.54$$

where the elements within J matrix represent the Bessel-function-based addition coefficients.

Now, in a similar way the total scattered field from all spheres can be expressed as a single expansion about the cluster origin by translation of the fields from the spheres to the cluster origin. Therefore the expansion coefficients for the total scattered field are given by

$$\mathbf{a}^{O}_{mnp} = \sum_{i=1}^{Ns} J^{Oi}_{mnpklq} \mathbf{a}^{i}_{klq} \qquad 2.55$$

After combining all equations

$$\mathbf{a}^{O}_{mnp} = \sum_{i,j} J^{Oi}_{mnpm'n'p'} T^{ij}_{m'n'p'k'l'q'} J^{jO}_{k'l'q'klq} \mathbf{p}^{O}_{klq}$$

$$\therefore \mathbf{a}^{O}_{mnp} = T^{O}_{mnpklq} \mathbf{p}^{O}_{klq} \qquad 2.56$$

We now have a cluster transition matrix T^O which treats the entire cluster of spheres as a single particle with a single origin and relates the incident field to the scattered-field expansion coefficients.

The incident-field coefficients of the *ith* sphere can be expanded by

$$\left(p^{i}_{mn}, q^{i}_{mn}\right) = \left(p_{mn}, q_{mn}\right) \exp i\left[Z^{i} \cos\beta + (\sin\beta) \times (X^{i} \cos\alpha + Y^{i} \sin\alpha)\right] \qquad 2.57$$

$$p_{mn} = -i^{n+1} \frac{1}{E_{mn}} \left[\tau_{mn}(\beta) \cos\gamma - i\pi_{mn}(\beta) \sin\gamma\right] \times \exp(-im\alpha) \qquad 2.58$$

$$q_{mn} = -i^{n} \frac{1}{E_{mn}} \left[\tau_{mn}(\beta) \sin\gamma + i\pi_{mn}(\beta) \cos\gamma\right] \times \exp(-im\alpha) \qquad 2.59$$

with X^i, Y^i and Z^i denoting the origin of the *ith* sphere with respect to the cluster origin $E_{mn} = \frac{n(n+1)}{2n+1} \frac{(n+m)!}{(n-m)!}$ and α, β and γ are the Euler angles of rotation of the incident field from a z-propagating, x-polarised state.

$$\tau_{mn}(\beta) = \frac{d}{d\beta} P^{m}_{n}(\cos\beta) \qquad 2.60$$

$$\pi_{mn}(\beta) = \frac{m}{\sin\beta} P_n^m(\cos\beta) \qquad 2.61$$

where P_n^m are the associated Legendre functions.

2.4.1. Calculation of the cluster extinction cross-section, C_{ext}

There are two ways to calculate C_{ext} for fixed orientation radiation. The first is to calculate C_{ext} for a single sphere using

$$C_{ext}^{i} = \frac{4\pi}{k^2} \mathrm{Re}\left(E_{mn} \mathbf{P}_{mnp}^{i*} \mathbf{a}_{mnp}^{i}\right) \qquad 2.62$$

and then calculate C_{ext} for the entire cluster as the sum of all the spheres in the cluster

$$C_{ext} = \sum_{i=1}^{N_s} C_{ext}^{i} \qquad 2.63$$

The second method is to calculate C_{ext} for the entire cluster from the single-scattered field expansion by combining equations 2.55 and 2.56 to get

$$C_{ext} = \frac{4\pi}{k^2} \mathrm{Re}\left\{E_{mn} \mathbf{p}_{mnp}^{O*} T_{mnpklq}^{O} \mathbf{p}_{klq}^{O}\right\} \qquad 2.64$$

Implementing equation 2.64 is non-trivial because it requires the transformation of the sphere centred T-matrix to the cluster centred T-matrix.

For orientationally averaged radiation equation 2.64 must be integrated over all incident directions and polarisations. To do this the following integral relation must be employed

$$\frac{1}{8\pi^2} \int_0^{2\pi}\int_0^{\pi}\int_0^{2\pi} \mathbf{p}_{mnp}^{*} \mathbf{p}_{klq} d\gamma \cos\beta d\beta d\alpha = \frac{1}{2E_{mn}} \delta_{km} \delta_{\ln} \delta_{pq} \qquad 2.65$$

where δ is the Kroneker delta function. Therefore,

$$\overline{\mathrm{C}}_{\mathrm{ext}} = \frac{2\pi}{k^2}\,\mathrm{Re}\,T^{0}_{mnpmnp} \qquad 2.66$$

To use equation 2.66 it is necessary to transform the sphere-centred T-matrix into the cluster-centred T-matrix using equation 2.56. However, this can lead to a large increase in the number of expansions required when the spheres are separated by large distances. Therefore it is more convenient to use the sphere-centred T-matrix and to do this equation 2.56 is substituted into equation 2.66 to give

$$\overline{\mathrm{C}}_{\mathrm{ext}} = \frac{2\pi}{k^2}\,\mathrm{Re}\left(J^{0i}_{mnpm'n'p'}T^{ij}_{m'n'p'k'l'q'}J^{j0}_{k'l'q'mnp}\right) \qquad 2.67$$

Equation 2.67 can be further reduced by using two properties of the J matrix. Firstly

$$E_{mn}J^{ij*}_{mnpklq} = E_{kl}J^{ji}_{klqmnp} \qquad 2.68$$

Secondly, translation from i to j' and then from j' to j is the same as translation from i to j. Therefore

$$\sum_{n'=1}^{\infty}\sum_{m'=-n'}^{n'}\sum_{p'=1}^{2}J^{jj'}_{mnpm'n'p'}J^{j'i}_{m'n'p'klq} = J^{ji}_{mnpklq} \qquad 2.69$$

From this equation 2.67 can now be expressed in terms of the sphere-centred T-matrix such that

$$\overline{\mathrm{C}}_{\mathrm{ext}} = \frac{2\pi}{k^2}\,\mathrm{Re}\left(J^{ji}_{klqmnp}T^{ij}_{mnpklq}\right) \qquad 2.70$$

2.4.2. Calculation of the cluster scattering cross-section, $\mathrm{C}_{\mathrm{sca}}$

For fixed radiation $\mathrm{C}_{\mathrm{sca}}$ is given by

$$\mathrm{C}_{\mathrm{sca}} = \frac{4\pi}{k^2}E_{mn}\mathbf{a}^{0*}_{mnp}\mathbf{a}^{0}_{mnp} \qquad 2.71$$

Again, equation 2.66 requires transformation of the sphere-centred T-matrix to the cluster-centred T-matrix. However, using the *J* properties of equations 2.68 and 2.69 and substituting equation 2.55 into 2.71

$$\mathrm{C}_{\mathrm{sca}} = \frac{4\pi}{k^2}\,\mathrm{Re}\left(E_{kl}\,\mathbf{a}^{i*}_{klq}\,J^{ij}_{kjqmnp}\,\mathbf{a}^{j}_{mnp}\right) \tag{2.72}$$

with further expansion

$$\mathrm{C}_{\mathrm{sca}} = \frac{4\pi}{k^2}\,E_{mn}\left[\mathbf{a}^{i*}_{mnp}\,\mathbf{a}^{i}_{mnp} + 2\,\mathrm{Re}\left(\mathbf{a}^{i*}_{mnp}\,J^{ij}_{mnpkjq}\,\mathbf{a}^{j}_{klq}\right)\right] \tag{2.73}$$

The first and second terms of equation 2.73 are the independent (single sphere) and dependent (multiple sphere) contributions to the scattering from the entire cluster.

For orientationally averaged scattering equations 2.53 and 2.54 are substituted into equation 2.72 and the incident field is then integrated over all incident angles using the integral relationship of equation 2.65 giving

$$\overline{\mathrm{C}}_{\mathrm{sca}} = \frac{2\pi}{k^2}\,\mathrm{Re}\left\{\frac{E_{mn}}{E_{kl}}\left[J^{ii'}_{mnpuvw}\,T^{i'j}_{uvwklq} \times \left(T^{ij'}_{mnpu'v'w'}\,J^{j'j}_{u'v'w'klq}\right)^{*}\right]\right\} \tag{2.74}$$

The extinction efficiencies are based on normalising the cross-sections to the volume-mean radius of the cluster.

Chapter 3

3. Gold nanoparticle colloidal crystals

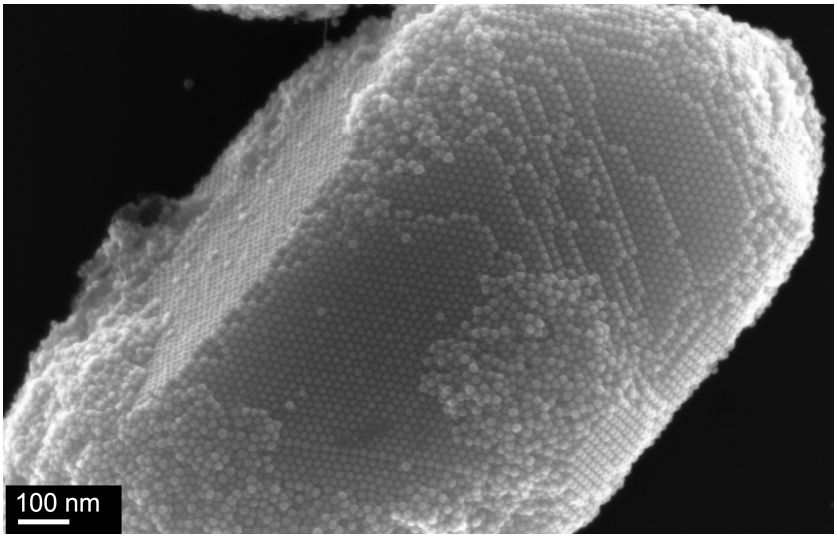

Figure 3.1. A three-dimensional micron-sized colloidal crystal synthesised from 15 nm diameter spherical gold nanoparticles.

This chapter will describe a technique that was developed for the controlled assembly of colloidal crystals from spherical gold nanoparticles.[i] An example is shown in figure 3.1. Irradiation of a gold colloid suspension with a 514 nm laser at 480 mW deposited micron-sized three-dimensional colloidal crystals on a glass slide without the use of templates or pre-functionalised substrates. The deposition location is controlled by the position of laser

[i] The majority of the work presented in this chapter has been published as a paper entitled, "Laser-induced assembly of gold nanoparticles into colloidal crystals" by N. Harris, M.J. Ford, M.B. Cortie and A.M. McDonagh, in Nanotechnology, 2007, **18**, 365301.

irradiation and an array of colloidal crystal structures can be created by translation of the glass substrate under the laser beam. Control experiments and calculations show that localised heating of the gold nanoparticles may be one of the underlying mechanisms of colloidal crystal formation.

This chapter will also describe the effect of particle order and disorder on the calculated optical extinction spectra of three-dimensional structures. Individual Simple Cubic (SC), Body Centred Cubic (BCC) and Face Centred Cubic (FCC) structures, and chains of these same structures, where spherical gold nanoparticles replace the atoms within the crystal, are modelled using the T-matrix technique. In addition, hexagonally- and spherically-shaped FCC colloidal crystals containing approximately 100 gold nanoparticles are modelled. Both the single FCC structure and the spherically-shaped 100 particle FCC colloidal crystal are disordered and compared against their ordered counterparts. The ordered structures produce an additional extinction peak that is not present in the disordered structures. Suppression of the additional extinction peak results from inter-particle spacings that are no longer well-defined in the disordered structures. This has the effect of reducing the extent of hybridisation between particle plasmon modes, whereas hybridisation is enhanced in the ordered structure due to the finite set of well-defined inter-particle spacings.

3.1. Synthesis of three-dimensional gold nanoparticle colloidal crystals

3.1.1. Methods

Oleylamine-stabilised gold nanoparticles with a hydrodynamic diameter of approximately 15 nm were prepared in toluene according to the modified procedure described by Hiramatsu and Osterloh.[18] Briefly, 100 mg of tetrachloroauric acid combined with 2.4 ml of oleylamine and 5.8 ml of toluene was quickly injected into a boiling solution of 5.8 ml of oleylamine and 98 ml of toluene. Heating was stopped after 2 hours and 200 ml of ethanol was added to precipitate the particles. The resultant particles were then

isolated by centrifugation, washed three times with 50 ml of methanol to remove unreacted starting materials and allowed to dry to yield a black powder.

Particle characterisation was performed using a Zeiss Supra 55VP LEO Scanning Electron Microscope (SEM) and a FEI XL30 Environmental Scanning Electron Microscope (ESEM). UV-visible absorption spectra were measured using a mini-1240 Shimadzu and a Cary 5E spectrophotometer. Dynamic Light Scattering (DLS) measurements were performed using a Malvern Zetasizer Nanoseries particle sizer.

Methyl Methacrylate (MMA) (Aldrich 99%) was washed with 10% aqueous sodium hydroxide to remove the polymerisation inhibitor, then MilliQ water and dried with anhydrous sodium sulphate. 4 mg of gold nanoparticle powder was then added to 10 ml of MMA and sonicated for 1 minute to disperse the particles. The MMA-dispersed particles were characterised by an SEM, UV-visible spectroscopy and DLS.

The gold nanoparticle colloid in MMA was poured into a 5 cm diameter Petri dish containing a glass microscope slide so that the depth of the liquid containing the gold nanoparticle in MMA colloid was approximately 5 mm. A 514 nm continuous wave Coherent Innova 70 argon ion laser was used within this experiment.

The Petri dish was mounted on an X-Y stage and a region of the glass slide was irradiated with 480 mW with a 1 mm spot size for two minutes. The sample was then moved 0.5 mm and the procedure repeated until an array of dots covering an area of approximately 4 mm x 0.5 mm was created. Figure 3.2 shows a schematic diagram of the experimental setup. The arrays were then examined using an SEM and EDS.

These experiments were also performed with methyl isobutyrate and ethyl acetate with identical results.

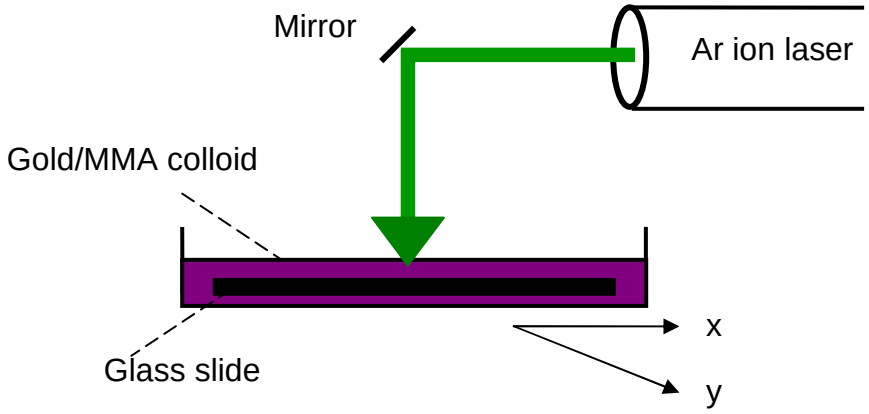

Figure 3.2. Schematic diagram of the experimental setup. A 514 nm Argon ion laser irradiates a gold nanoparticle in MMA colloid. An X-Y stage was used to translate the substrate.

3.1.2. Results

Figure 3.3 shows a representative SEM image of nanoparticles from the toluene colloid.

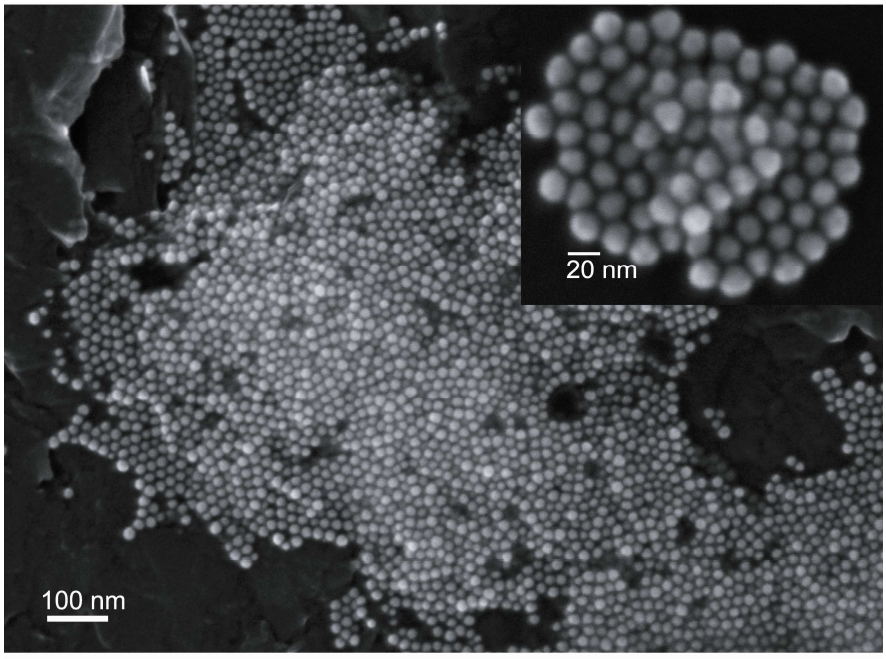

Figure 3.3. Oleylamine-protected gold nanoparticles imaged with an accelerating voltage of 20 kV and a working distance of 3 mm (main image) and 2 mm (insert image).

The 15 nm hydrodynamic diameter of the gold nanoparticles, measured using DLS, includes the ligand shell, which is 2.3 nm for oleylamine[154] so the actual diameter of the metal component of the particle is 10.4 nm. Figure 3.4(a) shows the UV-visible absorbance spectrum of the gold nanoparticle colloid in toluene, along with the calculated absorption efficiency, Q_{abs} of a 10.4 nm diameter (metal only) particle in toluene, calculated using Mie theory[68] and a frequency independent refractive index of 1.496. Both graphs have been normalised so they have a peak value of 1.

DLS was used to measure the size distribution of the gold nanoparticle in toluene colloid the results of which are shown in figure 3.4(b).

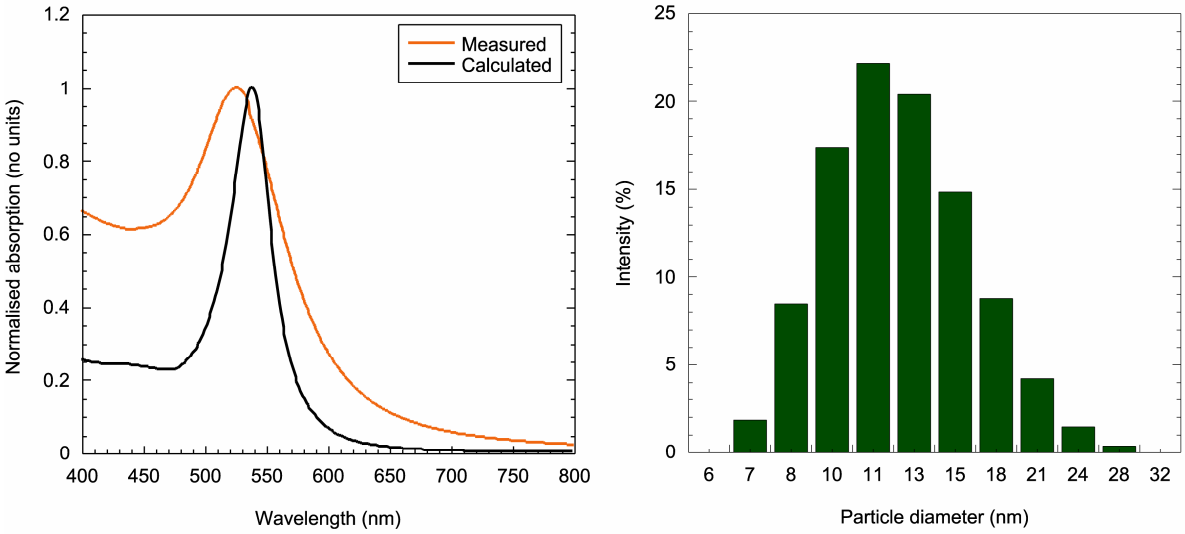

Figure 3.4. (a) Measured absorbance spectrum of the gold nanoparticle in toluene colloid before particle precipitation obtained with a mini-1240 Shimadzu UV-visible-NIR spectrophotometer and calculated Q_{abs} of a 10.4 nm diameter gold nanoparticle in toluene. **(b)** Histograms indicating the size distribution of the gold nanoparticle in toluene colloid before particle precipitation.

Figure 3.5(a) shows the measured and calculated UV-visible spectra after the gold nanoparticles were re-suspended in MMA. The measured size distribution of the gold nanoparticles in MMA colloid is shown in figure 3.5(b).

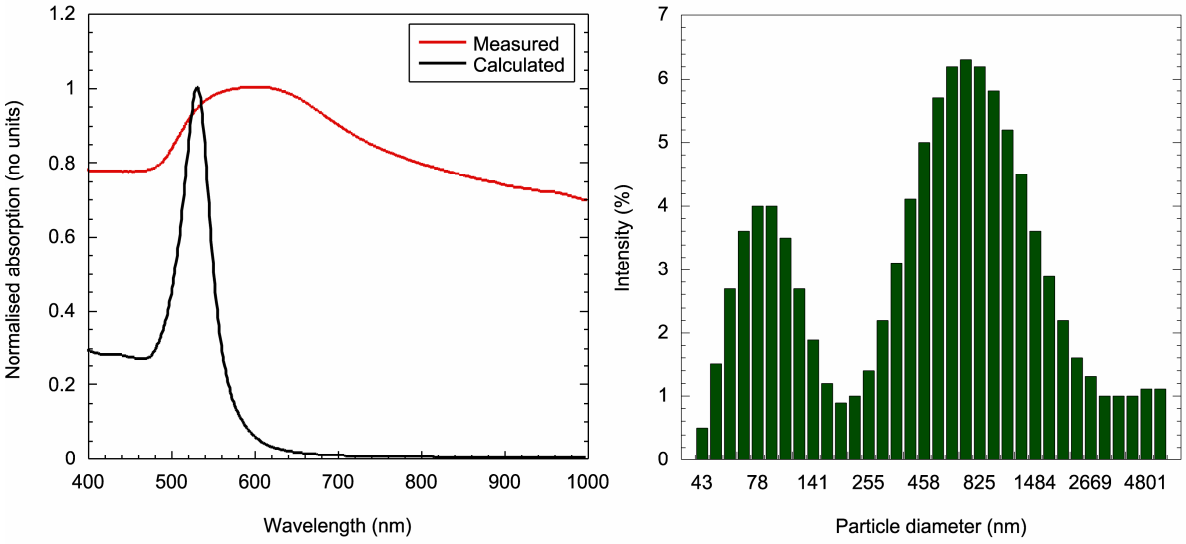

Figure 3.5. (a) Measured absorbance spectrum of 4 mg of dried gold nanoparticles re-suspended in 10 ml of MMA obtained with a mini-1240 Shimadzu UV-visible-NIR spectrophotometer and calculated Q_{abs} of a 10.4 nm diameter gold nanoparticle in MMA. **(b)** Histograms indicating the size distribution of the gold nanoparticle in MMA colloid.

Figure 3.6 shows SEM images of the gold nanoparticle structures, or supraspheres[154-156] after the nanoparticles were re-suspended in MMA.

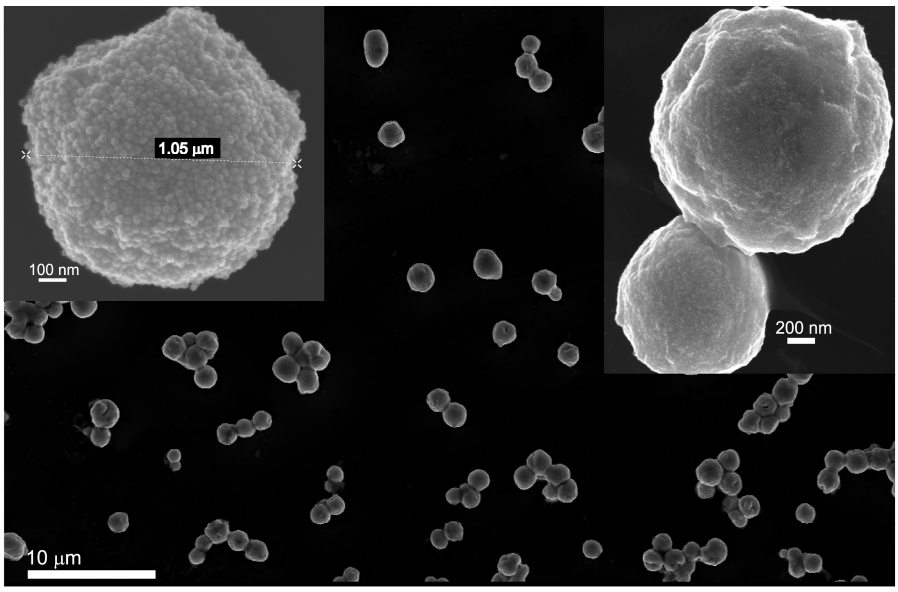

Figure 3.6. Gold nanoparticle structures (supraspheres) in MMA imaged with an accelerating voltage of 20 kV and a working distance of 3 mm.

Figure 3.7 shows ESEM images of an array of crescent-shaped dot structures formed on the glass slide after irradiation. Each crescent-shaped dot is formed from a single laser exposure of two minutes. Translation of the substrate using an X-Y stage allowed a 4 mm x 0.5 mm array to be prepared where each dot is approximately 300 microns in diameter, significantly smaller than the laser spot size of 1 mm, as can be seen from figure 3.7(a). The Gaussian beam profile of the laser presumably provides insufficient intensity towards the edges of the exposed region to cause formation of the colloidal crystals. Figures 3.7(b) and (c) show that the 300 micron structures are composed of smaller 2 – 3 micron-sized structures.

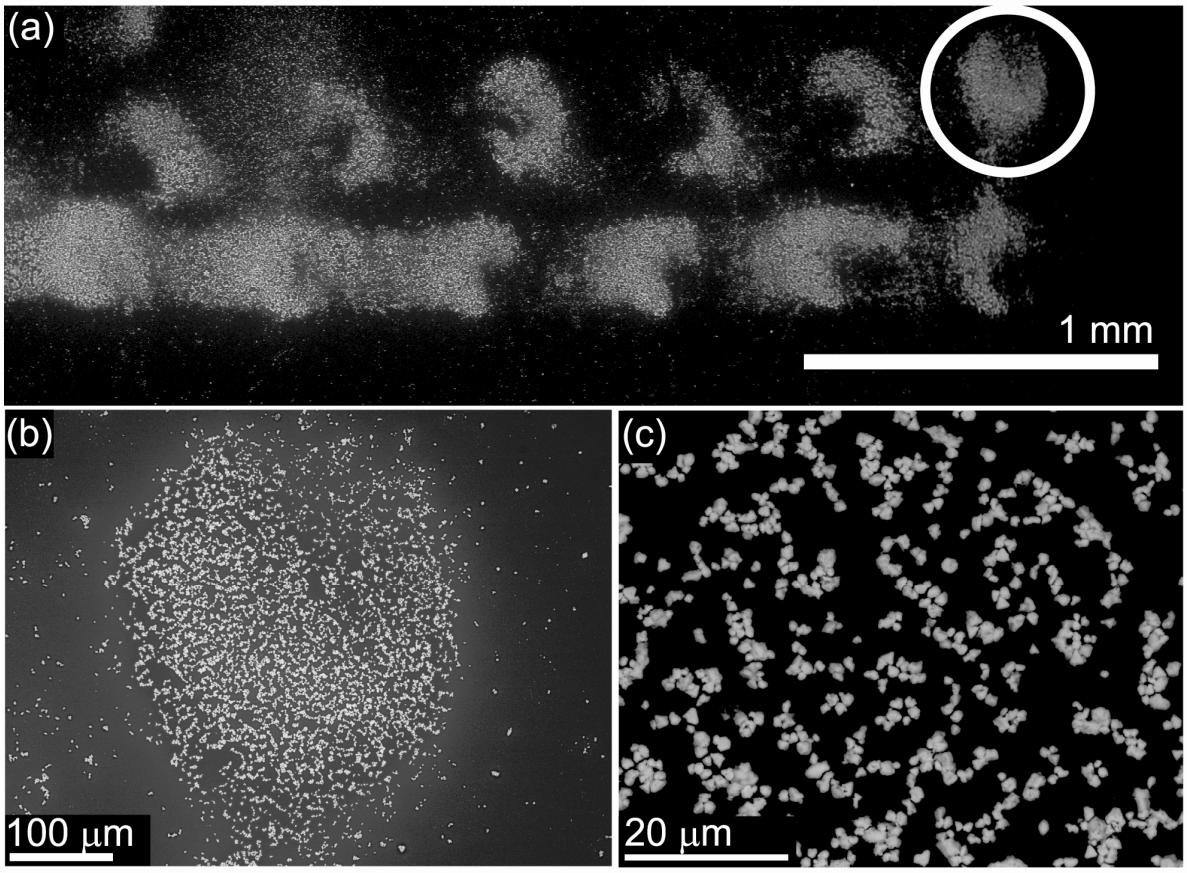

Figure 3.7. Images of laser-induced colloidal crystals deposited on a glass microscope slide **(a**) array of dots, **(b)** circled dot in (a) magnified 387x and **(c**) same dot magnified 3098x. All images were taken in low-vacuum mode with an accelerating voltage of either 20 kV or 30 kV and a working distance of 10.4 mm. All samples were imaged on the glass microscope slide and remained uncoated.

Higher magnification SEM images reveal that these structures are, in turn, micron-sized colloidal crystals that contain FCC packed gold particles terminated by (111) and (100) planes allowing the formation of hexagonal and pyramidal structures as shown in figure 3.8. The flaring in the images is due to charging of the glass slide while imaging.

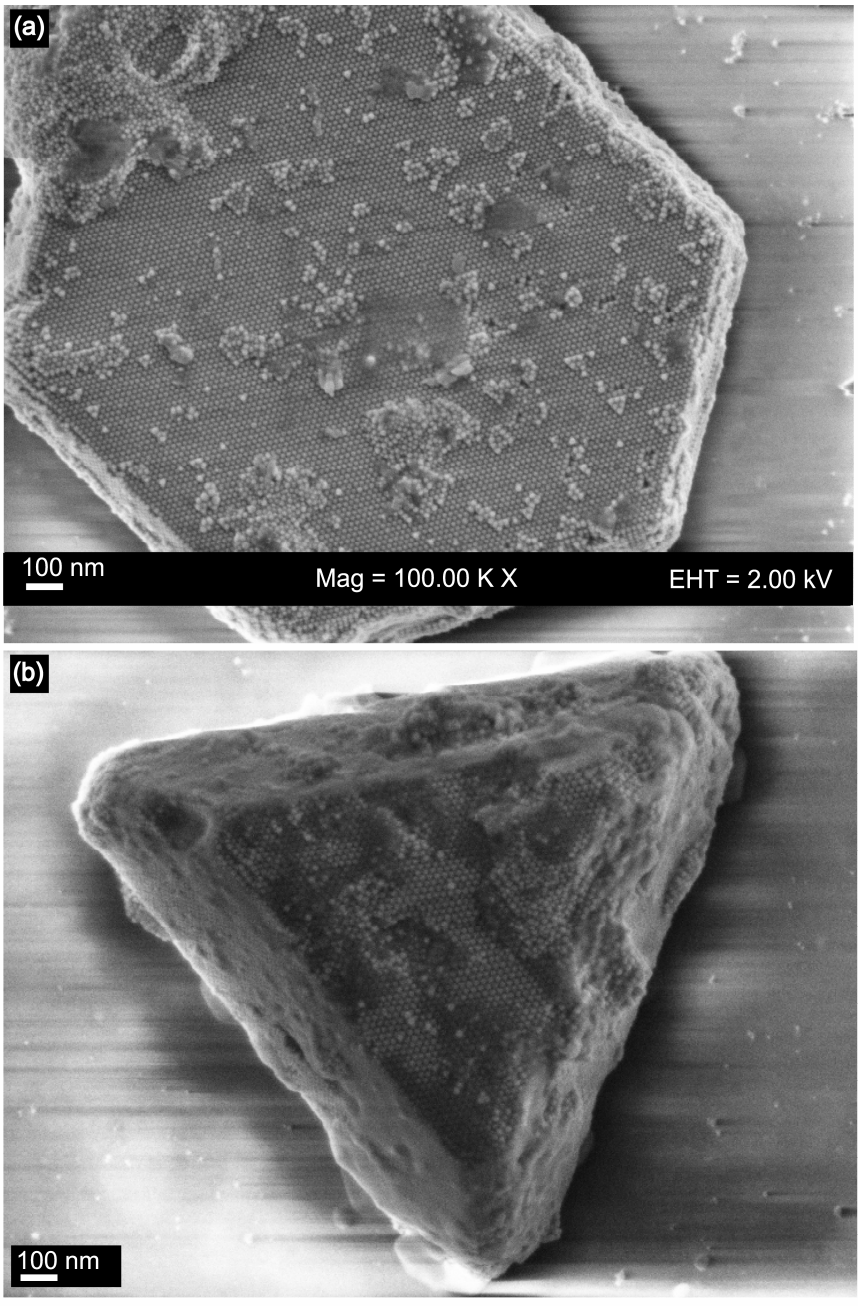

Figure 3.8. Colloidal crystals imaged with an accelerating voltage of 2 kV and a working distance of 2 mm.

Notably, these structures span several hundred particle diameters and exhibit very long-range order with few defects apparent.

Energy Dispersive Spectroscopy (EDS) measurements, figure 3.9, on the crescent-shaped structures show gold signals assigned to the gold nanoparticles and silicon, oxygen, sodium and potassium signals assigned to the glass substrate.

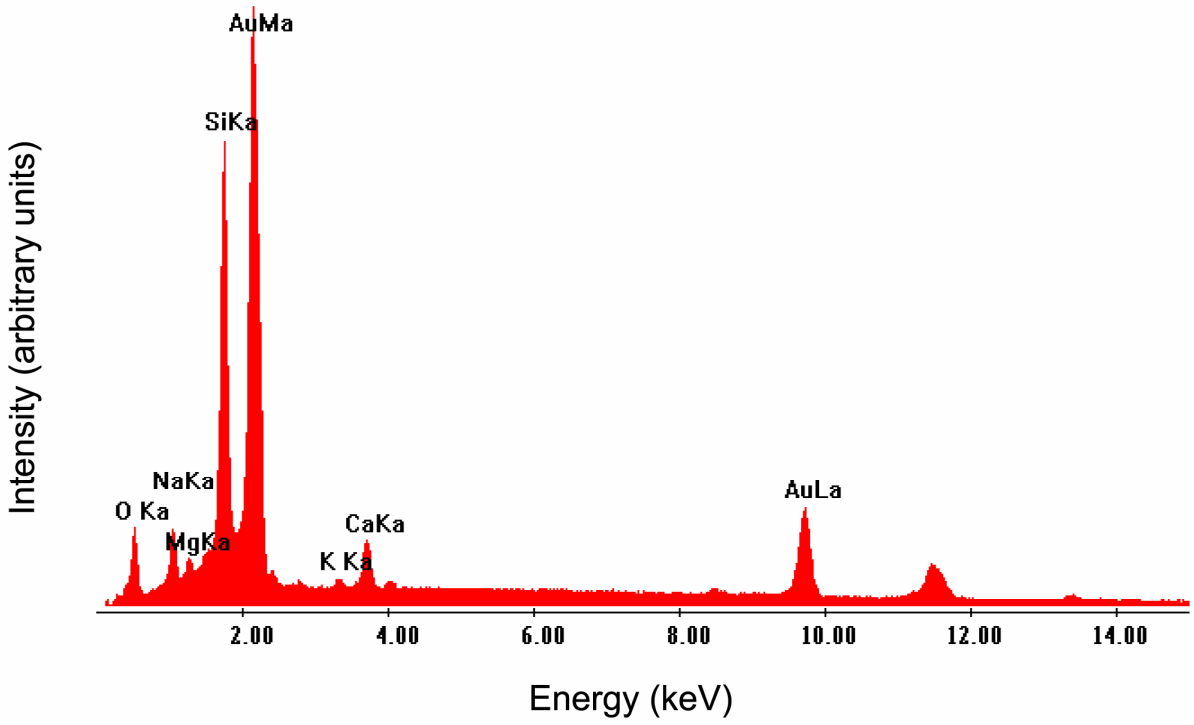

Figure 3.9. EDS of one of the crescent-shaped dot structures shown in figure 3.7(a). EDS performed with a FEI XL30 ESEM operating in low-vacuum mode with an accelerating voltage of 25 kV.

The UV-visible absorption spectrum of the 4 mm x 0.5 mm array of colloidal crystal structures on the glass slide is shown in figure 3.10. It can be seen that the observed spectrum is noisy, which is to be expected due to the insensitivity of the UV-visible spectrophotometer when measuring the low concentration of gold structures. Nevertheless there is a very broad observable plasmon resonance due to the aggregated individual nanoparticles in MMA at around 600 nm (compare to insert in figure 3.10).

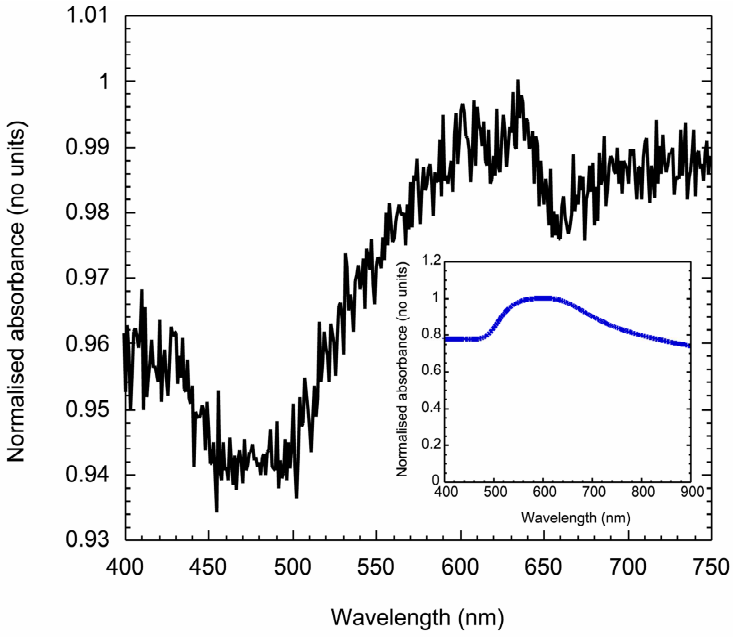

Figure 3.10. UV-visible absorbance spectrum of the 4 mm x 0.5 mm array obtained with a Cary 5E UV-visible-NIR spectrophotometer using a plain microscope slide for baseline correction. Insert shows the measured absorbance spectrum of 4 mg of dried gold nanoparticles re-suspended in 10 ml of MMA from figure 3.5(a).

Investigation of the mechanism responsible for suprasphere formation has revealed that oxidation during the original colloid synthesis is not a factor because experiments performed under an inert atmosphere (N_2) gave identical results.

Polymerisation of MMA is also not a factor as the supraspheres also form in methyl isobutyrate, which is a saturated analogue of MMA that cannot polymerise. Moreover, it has been found that the supraspheres will form in solvents with an ester group, such as ethyl acetate. See figure 3.11 for the molecular structure of MMA, methyl isobutyrate and ethyl acetate.

The effect of the solvent in the formation of the colloidal crystals was investigated by re-suspending the particles in toluene to determine whether washing the particles affects particle aggregation once they were re-suspended in another solvent. The measured spectra of the original and the re-suspended colloid, figure 3.12(a), shows that an insignificant amount of aggregation has occurred.

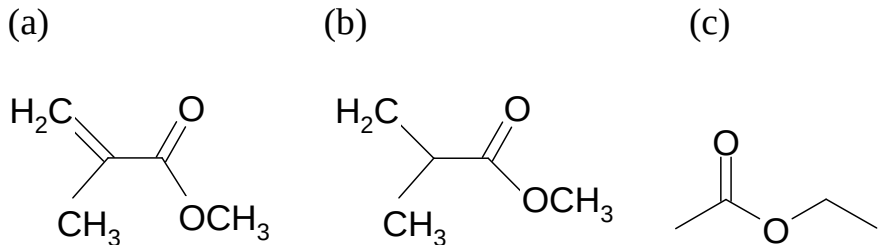

Figure 3.11. Molecular structure of **(a)** MMA, **(b)** methyl isobutyrate and **(c)** ethyl acetate.

Size distribution analysis (see figure 3.12(b)) reveals that the extent of the aggregation is significantly less than when the particles are re-suspended in MMA. Moreover, figure 3.13(a) shows a representative image of the particles after re-suspension in toluene and there is no indication of the presence of supraspheres.

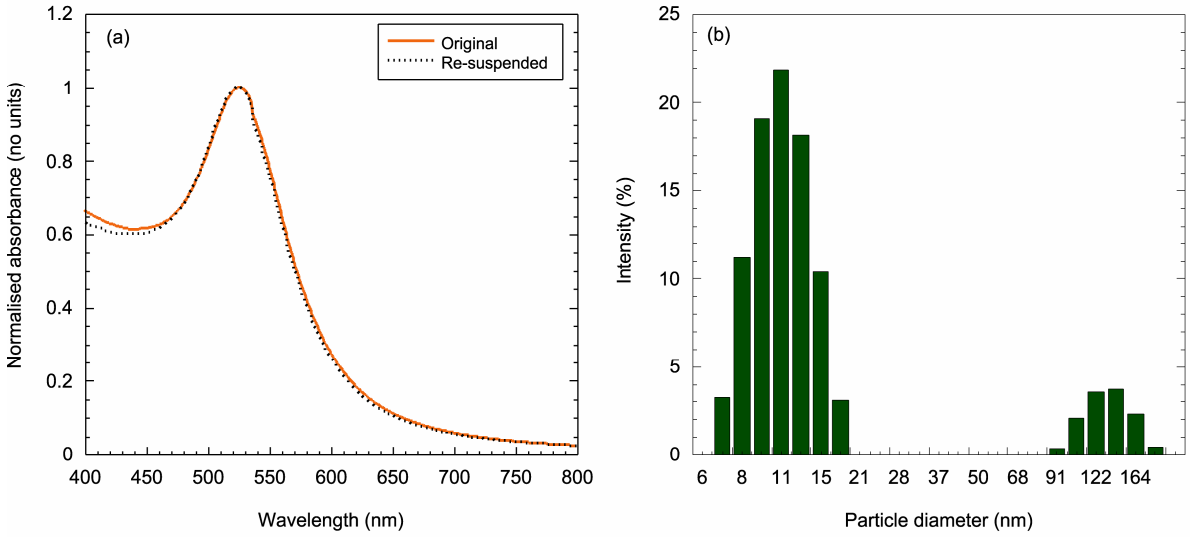

Figure 3.12. (a) Measured absorbance comparison between original toluene colloid and particles re-suspended in toluene obtained with a mini-1240 Shimadzu UV-visible-NIR spectrophotometer. **(b)** DLS size distribution of particles re-suspended in toluene.

Further laser irradiation experiments were performed on a colloid containing 4 mg of gold particles re-suspended in 10 ml of toluene. A representative image of the sample after laser irradiation is shown in figure 3.13(b). Large areas of nanoparticle aggregates of several layers are evident; in some areas, 500 nm thick aggregates were formed. Importantly, there is no evidence of close-ordered packing.

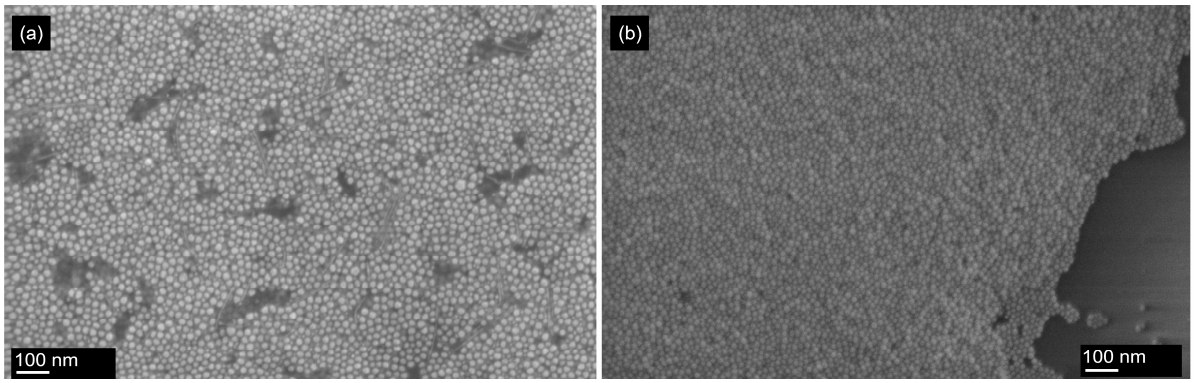

Figure 3.13. SEM images of **(a**) dried gold particles re-suspended in toluene on a silicon wafer and **(b)** dried gold particles re-suspended in toluene after laser irradiation on glass. Both samples were imaged with an accelerating voltage of 20.0 kV and a working distance of 2 mm.

Several experiments were performed to investigate thermal effects. Firstly, glass substrates with droplets of the gold nanoparticle in MMA colloid were heated in an oven at 150^{o}C for 20 minutes, figure 3.14(a). Inspection using an SEM shows that the gold nanoparticles are attached to large blocks of PMMA and no particle ordering is evident. One explanation for this observation is that the MMA rapidly polymerises to PMMA and fixes the position of the particles, prohibiting ordering into crystalline structures. Moderate heating of the gold nanoparticle in MMA colloid in a test tube at 80^{o}C in a water bath for 40 minutes produces a different result, figure 3.14(b). In this case, large aggregates of gold nanoparticles form with a small number of areas exhibiting short-range ordering over an area of between 500 to 800 nm.

Similar behaviour may be observed when several droplets of gold nanoparticles in MMA were evaporated quickly at room temperature (see figure 3.15(a)). In both cases, the facets that are characteristic in crystals are not evident.

Allowing 2 ml of gold nanoparticle in MMA colloid to evaporate slowly, over several hours, at room temperature from a vial containing a piece of silicon wafer produces three-dimensional colloidal crystals on the same scale as those produced through laser irradiation. An example is shown in figure 3.15(b).

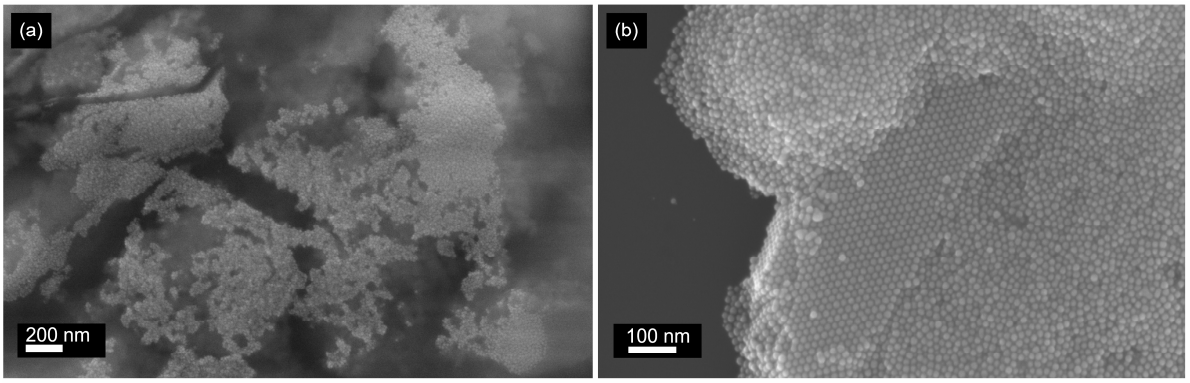

Figure 3.14. Images of gold nanoparticles in MMA colloid **(a)** on a glass slide after 20 minutes in an oven at 150^{o}C and **(b)** heated to 80^{o}C for 40 minutes. Both figures were imaged **(a)** in low-vacuum mode with an accelerating voltage of 20 kV, a working distance of 5 mm **(b)** in high-vacuum mode with an accelerating voltage of 2 kV and a working distance of 2 mm. Specimens were uncoated.

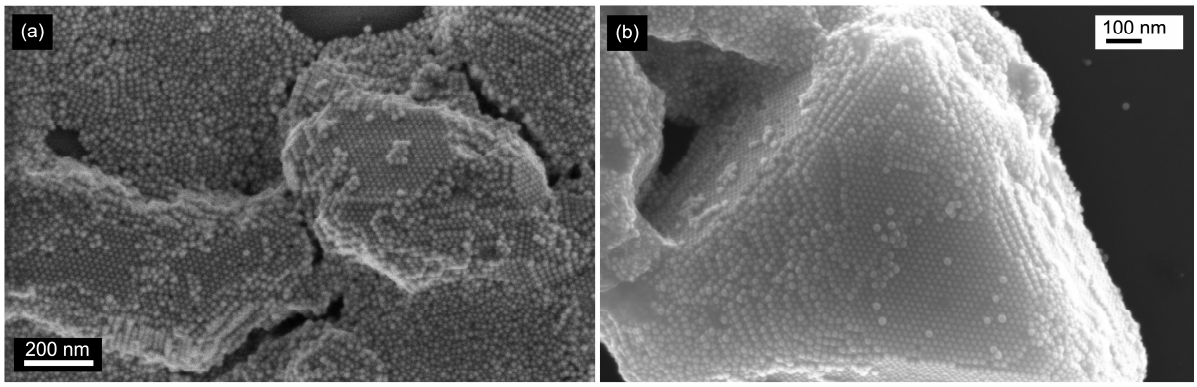

Figure 3.15. Images of gold nanoparticles in MMA colloid after (a) fast evaporation on glass and (b) slow evaporation on silicon. Both images were taken in high-vacuum mode with **(a)** an accelerating voltage of 2 kV and a working distance of 2mm and **(b**) an accelerating voltage of 20 kV with a working distance of 2 mm.

The effect of laser power, for the same irradiation time of 2 minutes, on crystal formation was also investigated and no crystal formation was evident with laser powers of less than 450 mW. These experiments show that the solvent properties and the extent of heating are both critical to the formation of the colloidal crystals.

3.1.3. Discussion

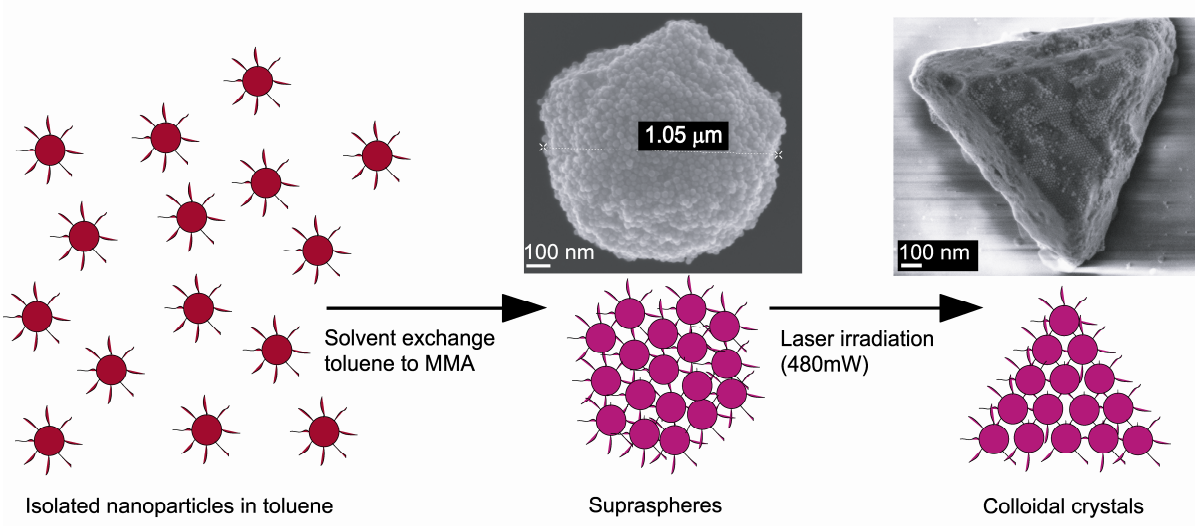

Figure 3.16. Schematic diagram of suprasphere formation after re-suspension of nanoparticles in MMA and the formation of crystals from supraspheres upon laser irradiation.

The measured spectrum of gold nanoparticles in toluene in figure 3.4(a) is in agreement with the results presented by Hiramatsu and Osterloh[18] with a peak at about 526 nm. In the calculated spectrum a peak is apparent at 538 nm and is significantly narrower than the measured spectrum. The difference between the two peaks can be attributed to several factors. When Mie theory is used to calculate the absorption efficiency of a particle several assumptions are made, namely, that the particle is spherical, homogeneous and naked (i.e. there is no stabilising agent) and there is no change in the refractive indices at the interface between the nanoparticle and the surrounding medium. From the insert in figure 3.3 it can be seen, although difficult to quantify, that the particles are not perfectly spherical, which will produce a broadening effect in the measured spectrum.[173] The refractive indices of oleylamine and toluene are 1.459 and 1.496, respectively and the presence of unreacted oleylamine in the colloid will have the effect of slightly blue-shifting the measured peak position relative to the calculated peak. Moreover, it has been shown that the electron density of a particle with a diameter less than or equal to 15 nm is influenced when molecules are absorbed onto the surface where intrinsic effects, which

result from changes in surface material properties, as opposed to extrinsic effects, which are size-dependent responses to the incident field,[14] dominate. The resulting metal-organic complex has the effect of damping and broadening the plasmon resonance. [17, 19, 174, 175]

The DLS size distribution measurements of the gold nanoparticle in toluene colloid, shown in figure 3.4(b), report an average hydrodynamic diameter of 15.0 nm, a standard deviation of 4.1 nm and a polydispersity value of 19.3 %. A polydisperse sample is defined as having a wide single mode or a number of different populations.

MMA was chosen for these experiments as it was anticipated that heat generated by the laser would polymerise the MMA and protect the crystal formation on the glass slide when it was removed from the colloid. It can be seen that re-suspension of the particles in MMA results in large aggregation of the particles when comparing the measured spectra from figures 3.4(a) and 3.5(a). The calculated peak is now produced at 532 nm, which is slightly blue-shifted from the gold nanoparticle in toluene calculation and this is to be expected as the refractive index of MMA, which is 1.414, is less than the refractive index of toluene and thus blue-shifts the plasmon peak.

DLS size distribution measurements of the gold nanoparticle in MMA colloid, figure 3.5(b), confirm that the solution no longer contains a narrow size distribution of, on average, 15 nm hydrodynamic diameter particles, but larger aggregates with two distinct peaks. The first peak has a diameter of approximately 95 nm with a standard deviation of around 35 nm and the second peak a diameter of approximately 960 nm with a standard deviation of around 675 nm. Moreover, the polydispersity is very poor at 80.2 % compared to the original gold nanoparticle in toluene colloid of 19.3 %.

All DLS data were processed using the default cumulants algorithm to extract the size information from the measured correlation function.[176] The cumulants algorithm assumes a monomodal colloid distribution and then represents the distribution as a Gaussian with the mean as the hydrodynamic average value and the polydispersity index as the variance. The cumulants algorithm, while well suited for monodisperse samples such as the gold nanoparticle in toluene colloid, is unsuitable for polydisperse samples such as the gold nanoparticle in MMA colloid shown in figure 3.5(b). A Non-Negative Least Squares (NNLS) algorithm that models the correlation function as an intensity contribution for each

of a number of size bands would be more appropriate for this sample, although not available at the time and care must be taken with the final size distribution measurements of this sample. Nevertheless, aggregation was apparent as the colloid changed colour from a deep burgundy, for the toluene colloid, to purple and eventually colourless due to particle sedimentation, when particles were re-suspended in MMA as is evident from the measured UV-visible spectrum in figure 3.5(a). Moreover, SEM images (figure 3.6) show that the colloid now contains large spherical amorphous aggregates, or supraspheres, of the original 15 nm diameter spherical particles.

The physical phenomenon underlying colloidal crystal formation has been described theoretically by Charbonneau and Reichman,[177] using the Gibbs ensemble Monte Carlo method on colloids with short-range interaction, as a two-step nucleation process whereby disordered supraspheres are initially formed followed by the ordering process. This two-step nucleation process leads to a lowering of the free energy associated with the structure allowing faster crystal growth when compared to classical nucleation theory.[154]

This computational analysis agrees with experimental observations reported by Compton and Osterloh[154], who investigated the process of aggregation by adding dodecanethiol to a solution of oleylamine-stabilised nanoparticles in chloroform. The presence of the dodecanethiol displaced the amine, due to its greater affinity for gold, and aggregation was initiated as the length of the thiol is shorter than that of the amine and is less soluble in chloroform, allowing the initial formation of supraspheres followed by their subsequent ordering into crystals. In agreement with the results of Compton and Osterloh, the lack of long-range order in the heated solution, figure 3.14(b), and fast evaporative control samples, figure 3.15(a), suggests that these structures grew over a short-time scale where crystalline growth via diffusion processes was hindered as the solvent evaporated in a matter of minutes. In contrast, the slow evaporative experiments, figure 3.15(b) allowed adequate time (several hours) for large colloidal crystals to form at room temperature.[154]

An interesting set of experiments was performed by Klajn *et al.*[155] [156] whereby photoisomerisation of dithiol ligands attached to the surface of gold nanoparticles allowed them to use light-induced self assembly of the supraspheres into three-dimensional micron-sized colloidal crystals and vice versa. They explained the structural reversibility in terms

of free energies of the structures. The application of UV irradiation or sunlight had the effect of either increasing or decreasing the nanoparticle binding energies sufficiently to allow the formation of crystals or supraspheres. Essentially when the inter-particle interactions were weak, entropy dominated and supraspheres were formed. However, upon application of UV-irradiation the inter-particle interactions were strong enabling the potential energy to overcome entropic effects, allowing the subsequent formation of colloidal crystals. In our case it is hypothesised that the laser-induced localised plasmonic heating of the nanoparticles accelerates the second step of the nucleation process by increasing the level of diffusion enabling the suprasphere to escape its local energy minimum and allow heterogeneous growth into the more energetically favourable colloidal crystal structure.

Localised heating of gold nanoparticles is well-established.[56, 178] The measured absorbance spectra of the gold nanoparticles in MMA colloid as well as the calculated absorption efficiency, Q_{abs} have been shown in figure 3.5(a). The Q_{abs} peak was calculated to be at a wavelength of 532 nm, at which the particle absorbs 0.92 times its geometric cross-section, but at the wavelength of the laser, which is 514 nm, Q_{abs} is 0.62. The measured absorbance peak is 0.46 at approximately 602 nm and considering the known concentration and diameter of the colloidal particles this measurement corresponds to a particle Q_{abs} of 0.47.

The following calculation shows the significant degree of heating of the gold nanoparticles that can be achieved through laser irradiation and thereby accelerate the thermal diffusion process. This calculation is based on the calculated Q_{abs} of a 10.4 nm gold particle in MMA and uses the same methodology that will be described in greater detail in Chapter 5.

If it is assumed that all of the absorbed radiation is converted to thermal energy then the heat transfer rate, P, measured in Watts, can be calculated from

$$P = IC_{abs} \qquad 3.1$$

where I is the laser intensity and C_{abs} is the particle absorption cross-section, equal to absorption efficiency, Q_{abs} multiplied by the particle cross-sectional area. P is calculated to be 3.22^{-11} W for the present laser intensity of approximately 611 kW/m^2 and Q_{abs} of 0.62 at 514 nm.

Now the temperature of an individual nanoparticle during laser irradiation can be calculated using a convective heat transfer model[178]

$$P = h4\pi r^2 \delta T \qquad 3.2$$

where h is the heat transfer coefficient of 240 W m^{-2} K^{-1}, r the particle radius and δT the change in particle temperature, which is calculated to be ≈ 395 K, an increase of around 100 K from the surrounding room temperature.

3.2. Modelling of three-dimensional gold nanoparticle structures

3.2.1. Methods

The optical extinction spectra of several different shaped three-dimensional structures composed of 15 nm diameter spherical gold particles were calculated using the T-matrix code developed by Mackowski and Mishchenko.[158, 159] These structures included a 96 particle hexagonally-shaped colloidal crystal and a 100 particle spherically-shaped colloidal crystal. Additionally, single SC, BCC and FCC structures containing 8, 9 and 14 particles, respectively were investigated. Chains of these same structures were also examined with the SC, BBC and FCC chains composed of 160, 150 and 162 particles, respectively. Nearest-neighbour particle spacings of 0.5, 0.75, 1.0, 1.5 and 2 nm were considered.

The SC, BBC and FCC chain structures were modelled using the fixed orientation T-matrix technique whereby the wavevector is perpendicular to the chain axis and the incoming electric field is polarised either perpendicular (transverse polarisation) or parallel (longitudinal polarisation) to the chain axis. For the remaining structures the

orientationally-averaged T-matrix technique was used whereby polarisation was orientationally averaged over the entire structure.

An optically determined frequency-dependent dielectric for gold in vacuum, taken from Weaver and Frederikse,[179] was used in the following calculations, which is effectively a local response. Spatially non-local effects will become important in metallic nanostructures where characteristic feature sizes of the structure are small. These effects in the optical properties of nanospheres have been discussed in some detail in the literature and are commonly described in terms of surface scattering and accounted for by a modified damping term.[14] They are manifest for gold particle sizes below about 5 nm in diameter[14] and result in broadening of the plasmon resonance. Recently, a more universal description in terms of a non-local dielectric function and treatment applicable to arbitrarily shaped nanostructures has been given by García de Abajo.[180] The results indicate that for 20 nm gold dimers non-local effects start to appear at gap spacing of about 0.5 nm and cause a red-shift of the resonance. Therefore it is reasonable to exclude these effects here as they would only perturb the calculations for the smallest of the inter-particle spacings and not change the overall conclusions.

As described in Chapter 2 the T-matrix technique calculates the scattered field from the structure as a superposition[172] of the individual fields scattered from each of the spherical particles within the structure. The individual fields scattered from the particles are expressed in terms of vector spherical harmonics and with the use of addition theorems a set of equations for the scattered-field expansion coefficients for the entire structure are created.[158]

In principle, the T-matrix method offers an exact solution to the problem of scattering from arrays of spheres and is a comparatively economic calculation compared with volume discretisation methods such as the DDA technique. Moreover, the difficulty when using the DDA technique for the present simulations lies in using enough dipoles to adequately resolve the inhomogeneous electric fields between the particles when the inter-particle spacing is small. However, the T-matrix method is not entirely immune from these numerical considerations particularly in the near-contact regime where many orders in the spherical harmonics may be required for the calculation to converge to a reasonable level.

The convergence criteria is defined to be the number of orders required so that the wavelength of the resonant peak changes less than 1 nm and the variation in magnitude of Q_{ext} is less than 0.001 at the resonant peak.

It is generally accepted that the number of orders required for convergence for an isolated sphere is

$$N = x + 4x^{\frac{1}{3}} + 2 \qquad 3.3$$

where x is the particle size parameter, $x = \frac{2\pi a}{\lambda}$, a is the sphere radius and λ is the wavelength of the incident light.[13, 158]

Equation 3.3 provides a lower limit to the number of orders required for convergence. For arrays of highly absorbing spheres in the near-contact regime the number of orders will be considerably higher as the singularity at touching is approached. For this reason the convergence conditions in these calculations have been carefully checked for different inter-particle spacings and for different polarisations.

The results are shown in figure 3.17 for a dimer of 15 nm diameter gold spheres with the wavevector perpendicular to the dimer axis and polarisations both perpendicular and parallel to the dimer axis. The data are plotted as a function of the ratio of inter-particle gap to particle diameter because it is this quantity that scales the scattering properties rather than absolute size of the particle or gap, at least up to a certain particle diameter.

For perpendicular polarisation the number of orders remains relatively constant, even at the smallest gaps sizes used here (gap to diameter ratio of 0.03) only 6 orders are required. The number of orders changes for a gap to diameter ratio of 0.3 from 4 to 6 orders because the inter-particle spacing has reduced to the point where more orders are required to resolve the interaction between the electric fields. These results also apply to end-on polarisation of the dimer. For parallel polarisation the number of orders increases rapidly as contact is approached. At a gap of 0.5 nm, corresponding to a ratio of 0.03, 17 orders are required for convergence. Khlebstov *et al.*[125] have reported around 30 orders are required

for an inter-particle spacing of 0.15 nm (0.01 ratio) and 40 for an inter-particle spacing of 0.075 nm (0.005 ratio).

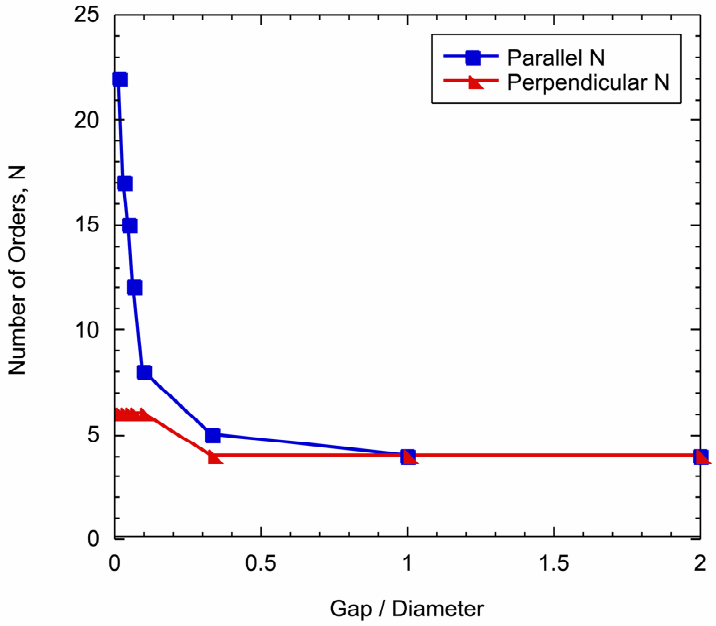

Figure 3.17. Number of orders of spherical harmonics required for convergence of the T-matrix calculations for a dimer of 15 nm diameter gold particles with varying inter-particle spacings. The wavevector was perpendicular to the dimer axis for both parallel and perpendicular polarisations.

With the computational facilities available it is tempting to increase computational accuracy to use more orders than those showing initial convergence. The drawback with this option is that the T-matrix uses forward recurrence to solve the Riccati-Bessel function, ψ_n, which is reported to be unstable[13] and round off errors become evident and the results either do not converge or the calculated scattering coefficients are incorrect.

The 100 particle spherically-shaped FCC colloidal crystal was disordered or melted with Molecular Dynamics (MD) simulations using the General Utility Lattice Program (GULP).[181] The theory of MD is available in many textbooks.[182, 183] Briefly however, the 15 nm diameter gold particles are treated as 1.5 $\mathring{A}$ (0.15 nm) diameter atoms and a 6-12 exponent Lennard-Jones potential, as per equation 3.4, was used to melt the structure over 1 million steps at a temperature of 1750 K.

$$U(r) = \varepsilon\left[\left(\frac{\sigma}{r}\right)^{12} - 2\left(\frac{\sigma}{r}\right)^{6}\right] \qquad 3.4$$

Where, ε is the well depth of 0.4 eV and σ is the equilibrium distance of 1.7. The values of ε, σ and temperature were carefully chosen to allow the spherically-shaped colloidal crystal to melt and retain its overall spherical shape without the onset of particle overlap or overall explosion of the structure.

3.2.2. Results and discussion

To investigate the effect of long-range order on the optical extinction spectra of a structure of gold nanoparticles, a flat hexagonally-shaped FCC colloidal crystal was modelled using the orientationally averaged T-matrix technique. This crystal structure was based upon the synthesised colloidal crystal from figure 3.8(a). The hexagonally-shaped colloidal crystal was modelled with a thickness of four particles and contained a total of 96, 15 nm diameter, gold particles with a nearest-neighbour spacing of 0.75 nm. A top-down schematic illustration of the crystal is shown in figure 3.18.

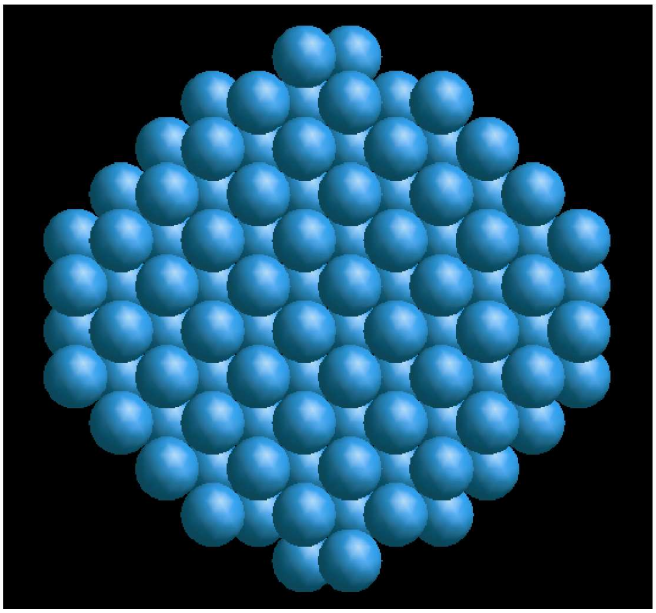

Figure 3.18. Schematic diagram of hexagonally-shaped FCC colloidal crystal composed of 96, 15 nm diameter, gold nanoparticles with a nearest-neighbour spacing of 0.75 nm.

The optical extinction spectrum for the hexagonally-shaped colloidal crystal is shown in figure 3.19.

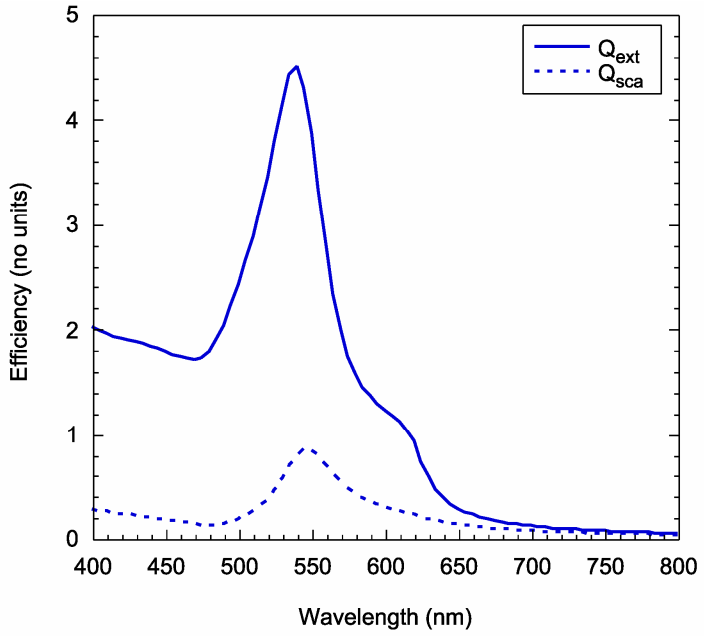

Figure 3.19. Optical response of a hexagonally-shaped FCC colloidal crystal structure composed of 96 spherical particles of 15 nm diameter with a nearest-neighbour spacing of 0.75 nm.

Absorption dominates the extinction spectrum and a broad extinction peak is evident at approximately 540 nm with a smaller additional shoulder present at approximately 610 nm. The presence of the second extinction peak was unexpected and was attributed to the presence of long-range particle ordering within the structure. To prove this hypothesis, two further structures were modelled using the orientationally averaged T-matrix method. The first was a spherically-shaped FCC colloidal crystal containing 100 spherical gold particles of 15 nm diameter and the second was the same structure after it had been melted using GULP to form a disordered suprasphere. The spherical geometry of both of these structures was based on the synthesised supraspheres from figure 3.6 because the spherical nature of the structure was more easily maintained during the melting process. These structures were modelled with a nearest-neighbour spacing of 0.75 nm. A schematic illustration of both structures is shown in figure 3.20.

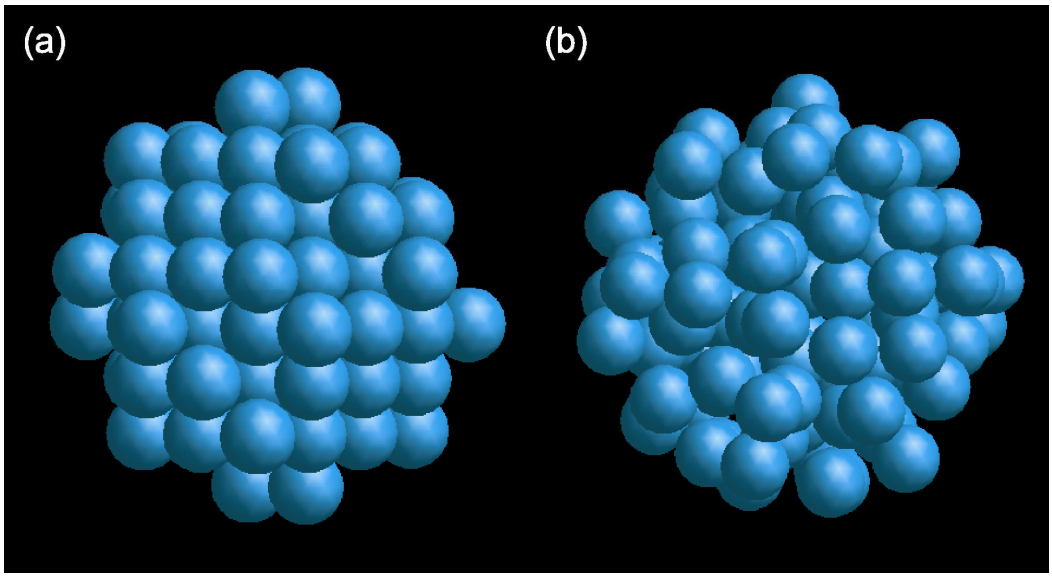

Figure 3.20. Schematic illustration of a 100, 15 nm diameter, particle **(a)** spherically-shaped colloidal crystal and a **(b)** disordered suprasphere.

The Radial Distribution Function (RDF) in figure 3.21 indicates the level of disordering that has occurred after the spherically-shaped colloidal crystal was melted into a disordered suprasphere.

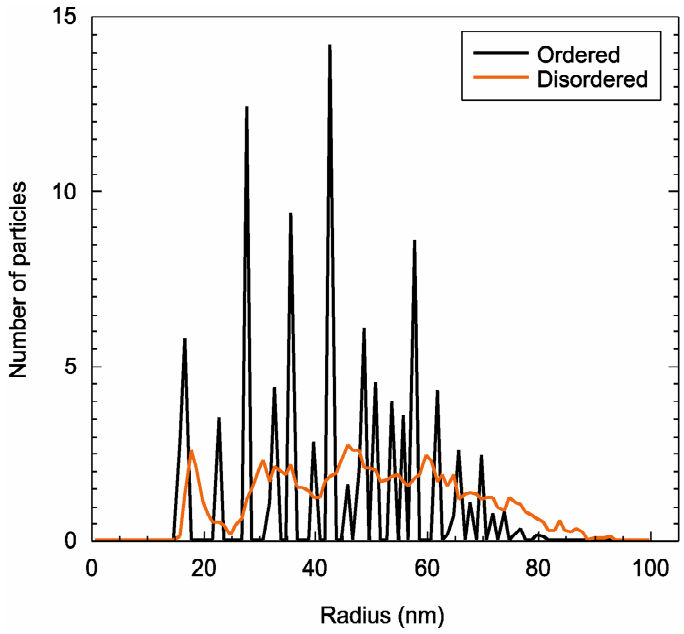

Figure 3.21. Radial Distribution Function (RDF) of the ordered (spherically-shaped colloidal crystal) and the disordered suprasphere.

The RDF for the spherically-shaped colloidal crystal shows long-range order as indicated from the very sharp peaks at larger distances. In contrast, the disordered suprasphere shows short-range order as indicated from the smaller number of particles distributed over larger distances.

Figure 3.22 shows the optical extinction spectra of both the ordered spherically-shaped colloidal crystal and the disordered suprasphere.

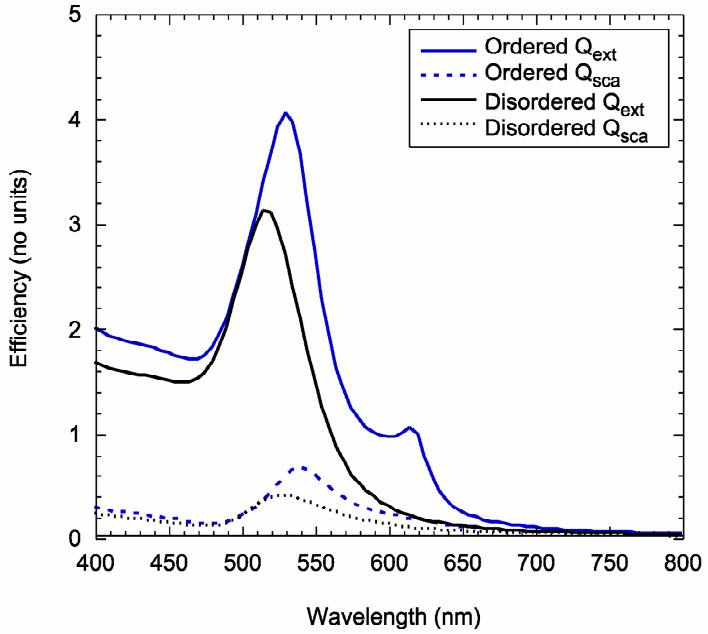

Figure 3.22. Optical response of 100, 15 nm diameter, particle ordered spherically-shaped colloidal crystal and the disordered suprasphere for a nearest-neighbour spacing of 0.75 nm.

It can be seen that a broad extinction peak is evident at 530 nm with a smaller peak evident at 615 nm for the ordered structure. As was the case for the hexagonally-shaped colloidal crystal a second extinction peak is produced by the ordered spherically-shaped colloidal crystal, however this peak is not evident in the disordered suprasphere. These results suggest that the presence of long-range order within the hexagonally- and spherically-shaped crystals is responsible for the production of the second extinction peak. Investigation into the mechanisms responsible for the production of this second extinction peak was done by modelling single SC, BCC and FCC structures with the express purpose of determining the effect of short-range or near-field interactions on the optical response of

structures with different symmetries. Schematic illustrations of these structures can be seen in figure 3.23.

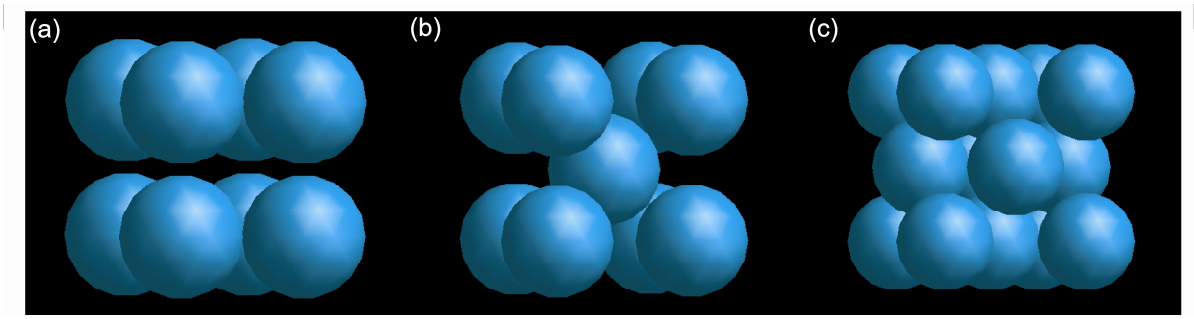

Figure 3.23. Schematic illustration of **(a)** SC, **(b)** BCC and **(c)** FCC structures made from 15 nm diameter spherical gold particles.

The optical extinction spectra of these structures, calculated using the orientationally-averaged T-matrix technique, are shown in figures 3.24 to 3.26 for nearest-neighbour spacings ranging from 0.5 to 2.0 nm.

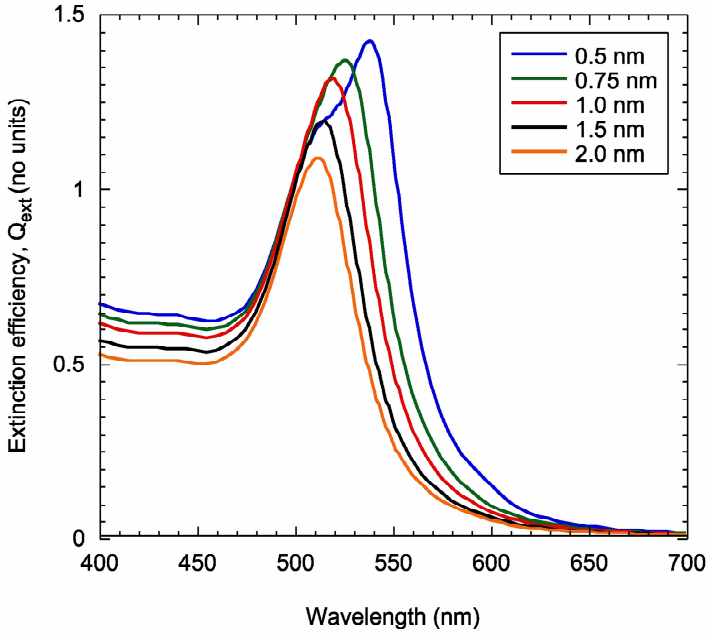

Figure 3.24. Optical response of a SC structure composed of 8, 15 nm diameter, spherical gold particles for nearest-neighbour spacings of 0.5, 0.75, 1.0, 1.5 and 2.0 nm.

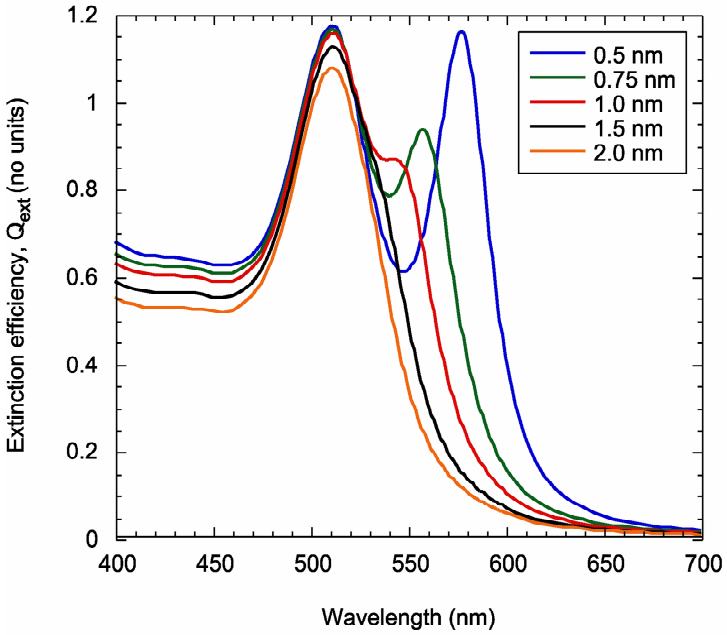

Figure 3.25. Optical response of a BCC structure composed of 9, 15 nm diameter, spherical gold particles for nearest-neighbour spacings of 0.5, 0.75, 1.0, 1.5 and 2.0 nm.

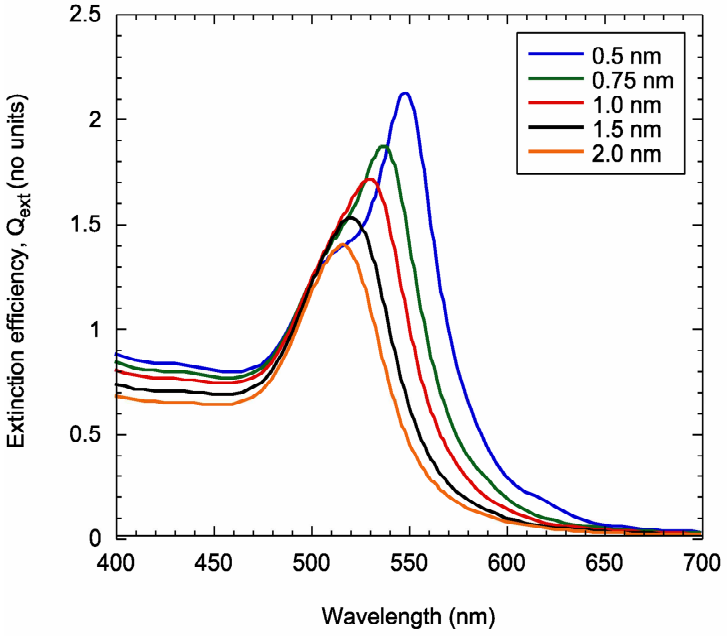

Figure 3.26. Optical response of a FCC structure composed of 14, 15 nm diameter, spherical gold particles for nearest-neighbour spacings of 0.5, 0.75, 1.0, 1.5 and 2.0 nm.

For all structures the extinction peak red-shifts compared to the extinction peak position of a single particle (505 nm, calculated using Mie Theory[68]) as the nearest-neighbour spacing is reduced. Both the FCC and SC structures produce almost identical extinction spectra. Although the peak shift for the FCC structure (549 nm) is slightly greater than that produced by the SC structure (538 nm) with a spacing of 0.5 nm. A slight shoulder is apparent in both the FCC and SC structures at this spacing however, it is not present for spacings larger than 0.75 nm. The effect is more dramatic for the 0.5 nm nearest-neighbour BCC structure where the extinction peak splits into two separate peaks, the first at 511 nm and the second at 577 nm. The second peak is not present in the single BCC structures with nearest-neighbour spacings larger than about 1 nm. This behaviour can be understood in terms of a hybridisation picture as proposed by Prodan *et al*.[22] As the spheres approach, interaction between the plasmon modes of the isolated spheres increases and they hybridise into 'bonding' and 'anti-bonding' combinations that are shifted to lower or higher energies, respectively relative to the isolated resonance. Based on this hybridisation model one would expect the production of a second peak, comparable to the BCC structure, for both the SC and FCC structures however, a slight shoulder becomes apparent in both extinction spectra when the nearest-neighbour distance is reduced to 0.5 nm. This indicates that hybridisation is evident between the particles within these structures. Moreover, it demonstrates that near-field interactions contribute significantly to the variation in the calculated extinction spectra because simply changing the crystal symmetry produces very different optical responses. Quantitative differences in the magnitude of the extinction efficiency are evident and to be expected due to the different number of particles in each of the structures.

To further investigate the effect of disorder on the optical extinction spectra, a single FCC structure with varying degrees of disorder was modelled using the orientationally averaged T-matrix method. In total three structures were considered. The first was a single FCC structure that was used to build both the hexagonally- and spherically-shaped colloidal crystals and has already been modelled in figure 3.26. The second and third structures were the same single FCC structure after partial and then greater disordering was introduced into the structure, respectively. Figure 3.27 shows schematic illustrations of the ordered, partially disordered and slightly more disordered single FCC structure.

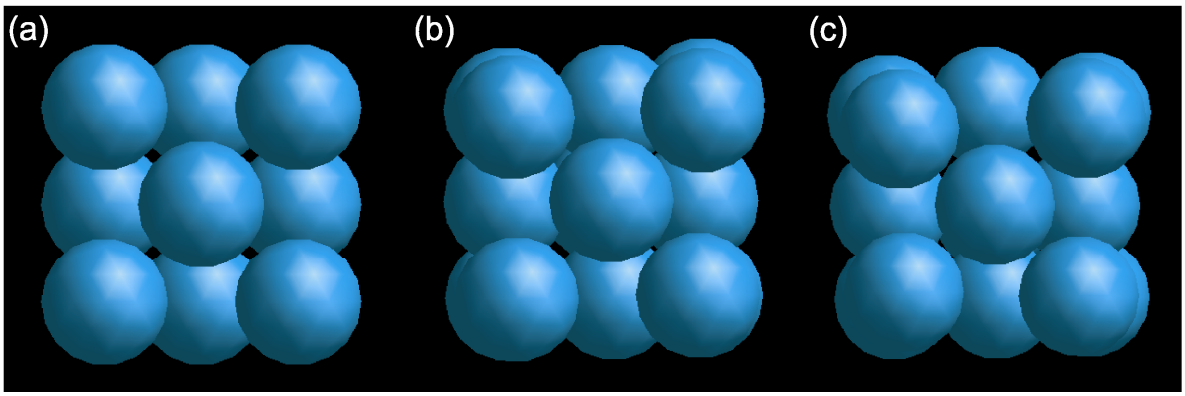

Figure 3.27. Schematic illustration of **(a)** ordered, **(b)** disordered and **(c)** more disordered 15 nm diameter nanoparticle single FCC structure.

Figure 3.28 details the RDF for each of these structures and gives a better indication to the level of disorder associated with each structure.

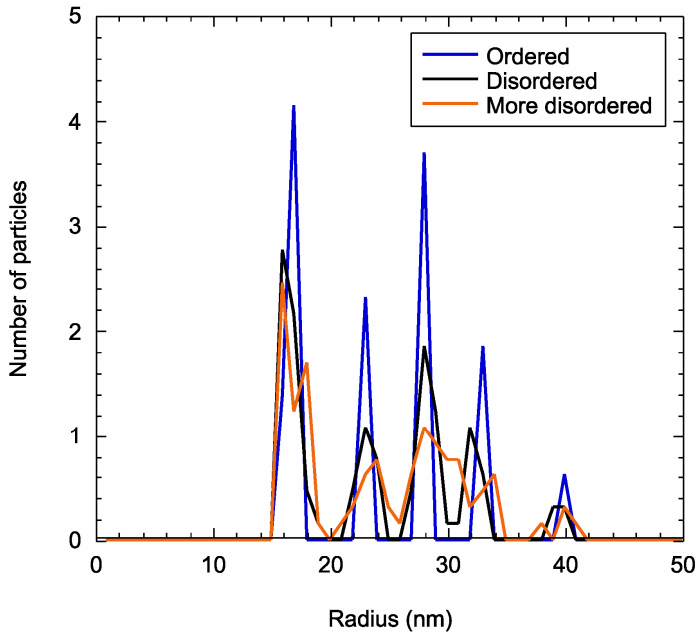

Figure 3.28. RDF of **(a)** ordered, **(b)** disordered and **(c)** more disordered 15 nm diameter particle single FCC structure.

The extinction spectra calculated for the ordered and disordered single FCC structures with nearest-neighbour distances of 0.75 nm are shown in figure 3.29.

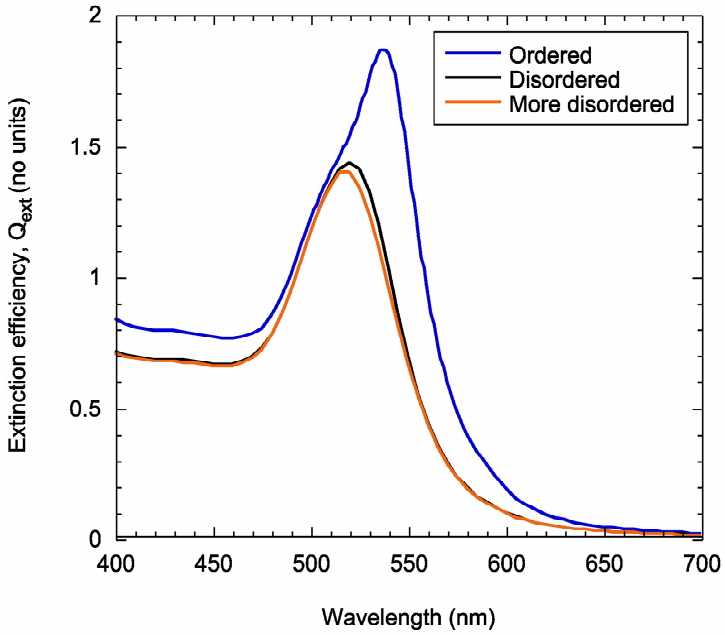

Figure 3.29. Optical response of **(a)** ordered, **(b)** disordered and **(c)** more disordered 15 nm diameter nanoparticle single FCC structure with a nearest-neighbour spacing of 0.75 nm.

The partial shoulder that is produced by the ordered FCC structure is no longer present in the disordered structures. Moreover, the disordered structures produce extinction spectra that are similar, in both peak position and magnitude, to ordered FCC structures with nearest-neighbour spacings of approximately 1.5 to 2.0 nm. These results would suggest that near-field interactions are important and have a substantial influence on the extinction spectra as has been seen from the variation in the calculated optical response of the single SC, BCC and FCC structures. Disordering the single FCC structure has the effect of producing inter-particle spacings that are no longer well-defined when compared with the ordered structure, as is evident from the RDF in figure 3.28. This has the effect of reducing the extent of the near-field interactions and therefore the level of hybridisation between the plasmon modes of the isolated particles and effectively suppresses the production of the additional peak. This disordering effect is seen to a larger extent in the comparison between the ordered spherically-shaped colloidal crystal and the disordered suprasphere. The long-range ordering of the spherically-shaped colloidal crystal allows for a finite number of well-defined inter-particle spacings enabling specific near-field

interactions that produce an additional extinction peak, which is not possible when the structure is disordered.

Additional investigation of near-field interactions in structures containing long-range order were performed by calculating the optical response of long chains of single SC, BCC and FCC structures using the fixed orientation T-matrix technique. All structures were modelled with a nearest-neighbour spacing of 0.75 nm. Schematic illustrations of the chain structures are shown in figure 3.30.

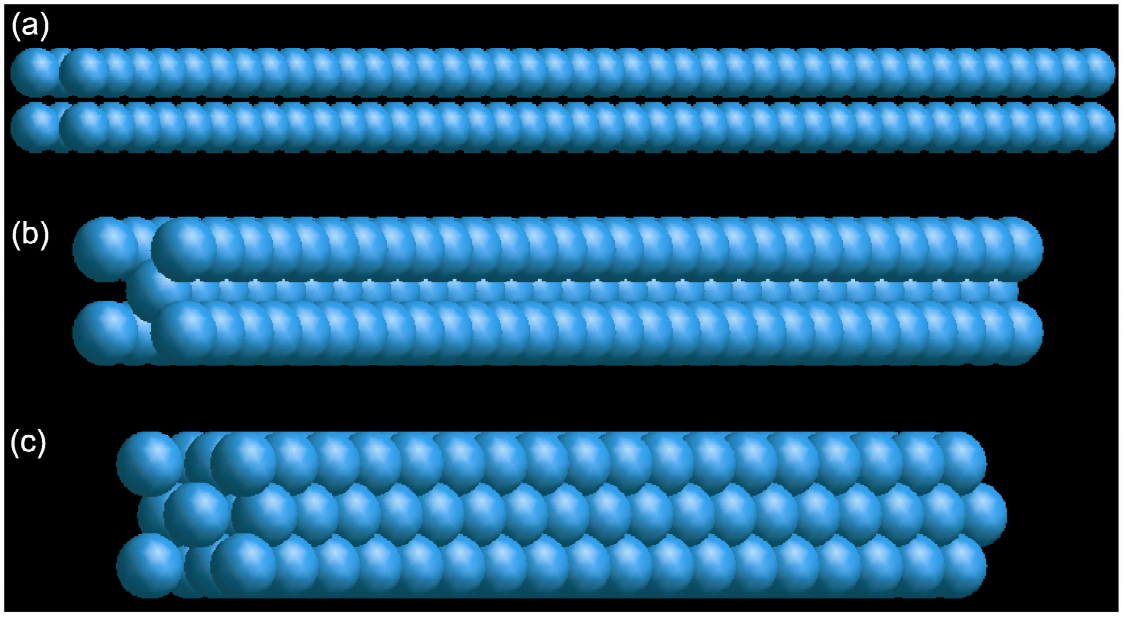

Figure 3.30. Schematic illustration of chains of **(a)** SC (160 particles), **(b)** BCC (150 particles) and **(c)** FCC (162 particles) structures composed of 15 nm diameter spherical particles with a nearest-neighbour spacing of 0.75 nm.

The calculated extinction spectra for all three chains are shown in figure 3.31. The wavevector is taken to be perpendicular to the chain axis and the electric field is polarised either perpendicular (transverse polarisation $\left(\frac{\pi}{2}\right)$) or parallel (longitudinal polarisation (0)) to the chain axis.

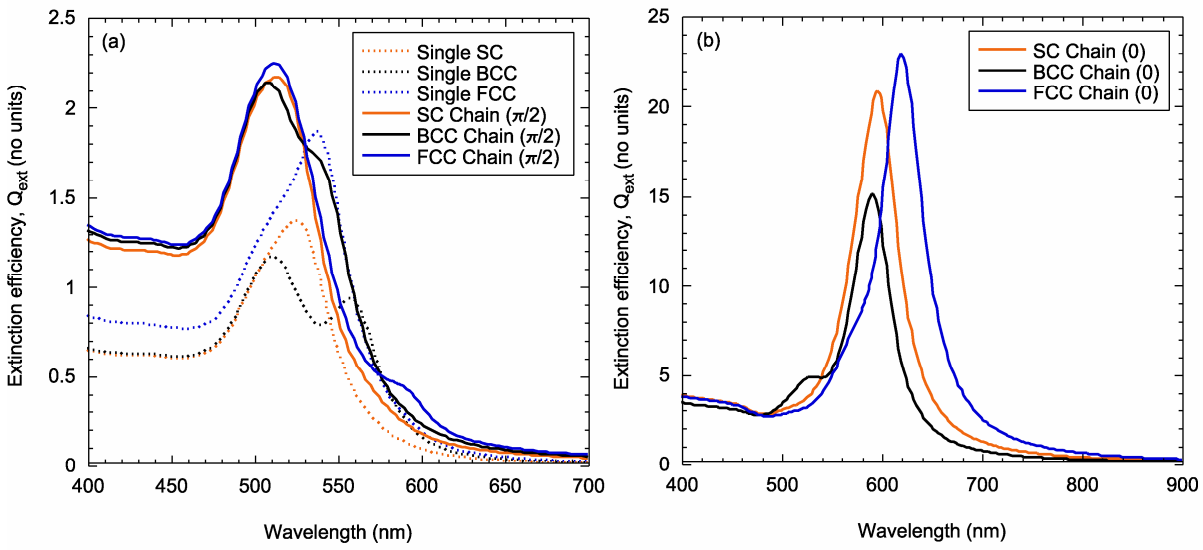

Figure 3.31. Optical response of a chain of single SC, BCC and FCC structures composed of 15 nm diameter spherical gold particles with a nearest-neighbour spacing of 0.75 nm.

For transverse polarisation the extinction peaks for all chains blue-shift when compared to the single SC, BCC and FCC structures. The partial shoulders in the extinction spectra for the single SC and FCC structures are no longer present in the chain structures and, in the case of the FCC chain, a second smaller peak at approximately 590 nm is evident. The second extinction peak at approximately 560 nm for the single BCC structure is blue-shifted and forms a shoulder to the main extinction peak that is evident at approximately 510 nm for the BCC chain. For longitudinal polarisation the extinction peak has red-shifted to about 600 nm for both the SC and BCC chains and approximately 620 nm for the FCC structure. An additional smaller peak is produced by the BCC chain at approximately 510 nm however, no second peaks are produced by either the SC or FCC chains with this polarisation. The magnitude of the extinction efficiency for transverse polarisation increases only slightly for all structures but more dramatically for longitudinal polarisation. In particular, the FCC structure produces an almost tenfold increase in magnitude.

The extinction spectra shown in figure 3.31 are intriguing and require additional analysis in order to elucidate on the underlying physical processes associated with near-field interactions in long ordered arrays. In order to do this a more simplified structure of a

chain of up to 150 spherical gold nanoparticles with varying inter-particle spacings was investigated. The techniques employed to examine the chain structure as well as the calculated results are detailed in Chapter 4.

3.3. Conclusions

In summary, a facile method to synthesise three-dimensional, micron-sized gold colloidal crystals by laser-induced heating of gold nanoparticles has been developed. This technique allows the user to write colloidal crystal patterns by moving a laser beam over a glass substrate. The same sized colloidal crystals can be synthesised using a slow evaporative technique, however control over deposition location is not possible. It is hypothesised that laser-induced plasmonic heating of the gold nanoparticle supraspheres is an inherent requirement associated with the rapid formation of colloidal crystals.

In addition, the effect of particle order and disorder within three-dimensional structures containing spherical gold nanoparticles was investigated using the T-matrix technique. A second extinction peak is produced by the ordered structures yet is not present in the disordered structures. The position of this additional peak depends upon the inter-particle spacing. It transpired that disordering the particles within the structure produces inter-particle spacings that are no longer well-defined when compared to the ordered structures. This reduces the extent of hybridisation between the plasmon modes of the individual particles and prevents the production of an additional extinction peak.

Chapter 4

4. Plasmonic excitation in a chain of nanospheres

One of the final points described in the previous chapter was the influence on the extinction spectra of near-field interactions in large ordered arrays composed of single SC, BCC and FCC structures. To investigate these interactions in greater detail, a more simplified structure of an ordered array of spherical gold particles has been modelled using the T-matrix technique in the regime where the near-fields of the particles are strongly coupled.[ii] The array consists of a one-dimensional chain containing up to 150 spherical gold particles of 15 nm diameter with varying inter-particle spacings. Incident light was polarised either parallel (longitudinal) or perpendicular (transverse) to the axis of the chain. Wavevectors that were either parallel ('end-on') or perpendicular to the chain axis were considered.

For a fixed chain length the longitudinal plasmon resonance red-shifts, relative to the resonance of an isolated sphere, as the inter-particle spacing is reduced. The shift in the plasmon resonance does not appear to follow an exponential dependence upon gap size for these extended arrays of particles. The peak shift is inversely proportional to the distance, a result that is consistent with the Van der Waals attraction between two spheres at short range which also varies as $\frac{1}{d}$. The transverse plasmon resonance shifts in the opposite

[ii] The majority of the work presented in this chapter has been published in a paper entitled, "Plasmon resonances of closely-coupled gold nanosphere chains" by N. Harris, M.D. Arnold, M.G. Blaber and M.J. Ford, in the Journal of Physical Chemistry C, 2009, **113**, 2784.

direction as the inter-particle gap is reduced this shift is considerably smaller and approaches 500 nm as the gap tends to zero.

Increasing the number of particles in the chain for a fixed gap has a similar effect on the longitudinal and transverse plasmon. In this case, however, the longitudinal plasmon tends towards an asymptotic value with increasing chain length, with the asymptotic value determined by the inter-particle spacing. Here, the approach to the asymptote is exponential with a characteristic interaction length of approximately two particles in the near-field regime. This approach to an asymptote as the chain length becomes infinite has been verified in a finite element calculation with periodic boundary conditions.

These calculations were extended to the far-field regime by calculating the extinction spectra of a chain of dimers with spacings between the dimers comparable to the wavelength of the incident light. Calculations were performed on chains containing a total of 200 spherical silver particles of 100 nm diameter. The dimers were aligned either perpendicular or parallel to the chain axis with varying inter-dimer and inter-particle spacings. For this chain structure only the 'end-on' wavevector was considered. The incident light was polarised either perpendicular (transverse) or parallel (longitudinal) to the dimer axis. The most significant result was produced by the dimers that were perpendicularly aligned to the chain axis. In this case, far-field diffractive effects dominate the extinction spectra for transverse polarisation, whereas near-field dimer effects dominate the extinction spectra for longitudinal polarisation.

4.1. Methods

The T-matrix code developed by Mackowski and Mishchenko[158, 159] as described in detail in Chapter 2 was used to calculate the optical extinction spectra of two chain configurations. The first configuration considered was a chain of individual 15 nm diameter spherical gold particles. The length of the chain was varied between 2 and 150 particles and the surface-to-surface inter-particle gap varied between 0.5 and 30 nm. The dimer convergence criteria reported in Chapter 3 has been tested on chains and calculations which are sufficiently converged for the dimer are converged for a 100 particle chain. The second

configuration considered was a chain of dimers of 100 nm diameter silver spheres with a total of 200 particles within the chain. The dimers were oriented either parallel to the chain axis (parallel dimer) or perpendicular to the chain axis (perpendicular dimer). Below, the spacing between the particles within the dimer will be referred to as 'inter-particle spacing' and the spacing between the dimers within the chain will be referred to as 'inter-dimer spacing'. The surface-to-surface inter-dimer spacing varied between 50 and 200 nm and the surface-to-surface inter-particle spacing varied between 3 and 50 nm.

All calculations were performed with the fixed orientation T-matrix technique. Scattering by the chain was calculated for the wavevector both perpendicular and parallel to the chain axis. Light was polarised parallel to the axis of the chain (longitudinal polarisation) and perpendicular to the chain axis (transverse polarisation) for the perpendicular wavevector. Only transverse polarisation need be considered with the wavevector parallel to the chain axis and this will be referred to as 'end-on' polarisation. Scattering by the chain of dimers was calculated with 'end-on' polarisation. In this case the incident light was polarised perpendicular (transverse) and parallel (longitudinal) to the dimer axis.

Simulations for an infinite chain of 15 nm diameter spherical gold particles were performed using the finite elements package COMSOL. Here a plane-wave source with perpendicular polarisation was applied using the scattered-field formalism and open boundaries were simulated using a cylindrical Perfectly Matched Layer (PML). Longitudinal periodicity was enforced by perfect electric conductors terminating a half-period at the symmetry points. Transverse symmetry was captured with a perfect magnetic conductor termination, reducing the simulation volume by a further factor of two. In addition to reducing computational requirements the high symmetry approach was more numerically stable. Scattering and absorption cross-sections were determined via surface integrals of the scattered and total fields, respectively. Numerical accuracy is generally achieved by adequate numerical sampling of the fields, especially in strong gradient regions. The maximum grid size was based on the PML and meshing algorithm employed by COMSOL, ensuring finer sampling in the gap where the field is most intense. Field accuracy in this region may benefit from finer sampling but this would have required much

greater computational resources. The sampling employed is sufficiently accurate for the discussions here.

The dielectric properties of gold and silver in vacuum were taken from Weaver and Frederikse[179] and non-local effects have not been considered as already described in Chapter 3.

4.2. Results and discussion

4.2.1. Chain of single spherical gold particles

The results from the T-matrix calculations for a 150 particle chain with varying inter-particle spacings are shown in figure 4.1 for longitudinal and transverse polarisations.

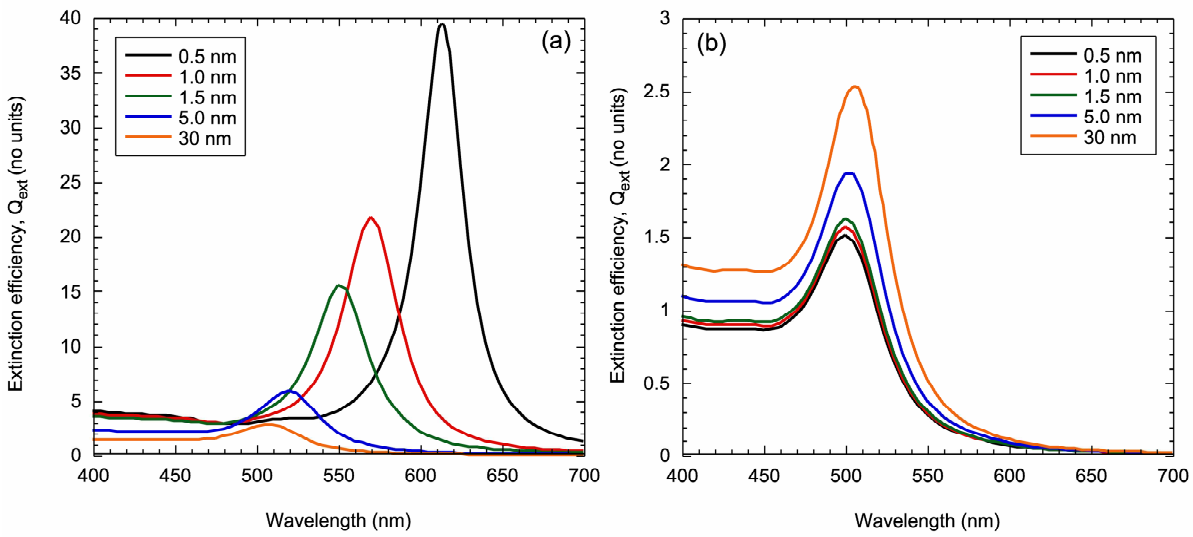

Figure 4.1. Extinction efficiency, Q_{ext} for a 150 particle chain with varying inter-particle gaps with the wavevector perpendicular to the chain axis for **(a)** longitudinal polarisation and **(b)** transverse polarisation.

For the largest gap, 30 nm, both spectra look essentially like an isolated particle with the same plasmon resonance peak for both orientations. As the inter-particle gap decreases the longitudinal and transverse plasmon modes are no longer degenerate and the former

shifts to longer wavelengths while the latter shifts to shorter wavelengths. This shift is much more pronounced for the longitudinal mode, the transverse mode approaches a limiting value of 500 nm.

This peak splitting phenomenon agrees with dimer[61] and other chain studies[119, 120, 184] and qualitative agreement is evident for a 10 particle, 40 nm diameter silver chain with an inter-particle gap of 0.2 nm (0.005 ratio) modelled by Quinten and Kreibig,[120] despite having taken only the dipole and quadrupole modes into consideration. Moreover, Brongersma *et al.*[185] and others[119] have reported a $\frac{1}{d^3}$ dependence on the plasmon peak position predicted by the point dipole interaction model, the appropriateness of this dependence to these results will be described later.

The magnitude of Q_{ext} for transverse polarisation increases as the inter-particle spacing is increased, whereas Q_{ext} increases as the inter-particle spacing is reduced for longitudinal polarisation. This behaviour can be understood in terms of the previously described hybridisation model.[22] One might expect more than two hybridised modes given there are more than two particles, although this is not evident in figure 4.1. This would suggest that the interaction length of the plasmons on different particles is relatively short, or that the smallest gap used here is not small enough to see these higher order modes. At the point of contact Romero *et al.*[186] have pointed out that an additional mode is now possible where charge is transferred between the individual particles. The T-matrix calculations cannot capture this and hence the calculation diverges as the contact point is approached.

For the longitudinal plasmon, Jain *et al.*[107] have recently demonstrated a universal decay constant for the shift of the plasmon as a function of inter-particle gap. More specifically they plot the shift of the plasmon peak relative to the single particle peak position as a function of the ratio of gap to particle diameter and fit the resulting curve to an exponential. They find a universal scaling constant that applies to different shaped nanoparticles as well as different dielectrics and propose optical measurements of the peak shift as a method of determining distances reliably at the nanoscale. The same analysis has been applied to the extended chain of 150 particles. The results are shown in figure 4.2

where the fractional peak shift ratio, $\Delta\lambda$ versus the ratio of the inter-particle gap to the particle diameter is plotted for a 150 particle chain with inter-particle gaps ranging from 0.5 nm to 30 nm for longitudinal polarisation.

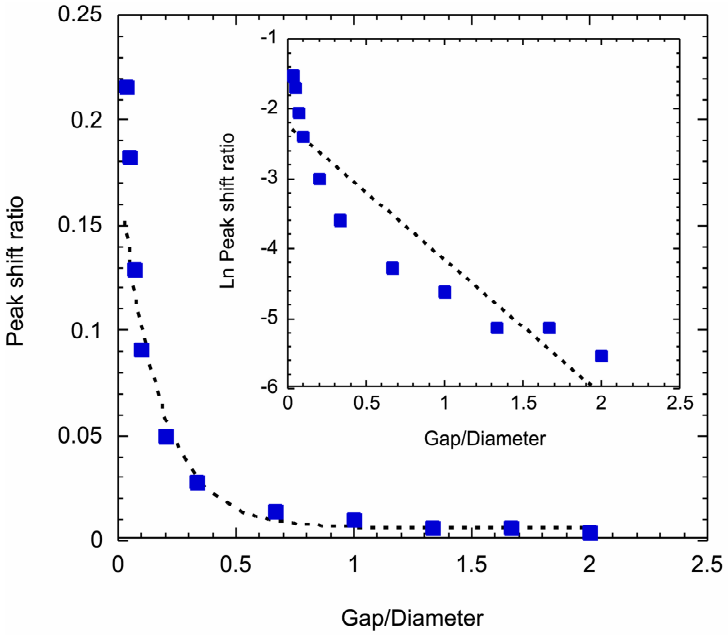

Figure 4.2. Graph of the ratio of the fractional peak shift ratio versus the ratio of inter-particle gap to diameter for a 150 particle chain. The dotted line is an exponential fit to the calculated points. Insert shows the corresponding natural log plot.

The fractional peak shift ratio is defined as

$$\Delta\lambda = \frac{\lambda_p - \lambda_s}{\lambda_s} \qquad 4.1$$

where λ_p is the chain plasmon peak position and λ_s is the plasmon resonance for an individual 15 nm diameter gold sphere (505 nm). In agreement with Jain *et al*. and previous studies[108, 187] the peak shift ratio decays almost exponentially with inter-particle gap. An exponential of the following form was fitted

$$\Delta\lambda = Ae^{-\frac{x}{\tau}} \qquad 4.2$$

to the calculated results, where x is the ratio of inter-particle gap to particle diameter and find the decay constant, τ, to be 0.17. This is close to the result reported by Jain *et al*. However, the quality of this fit is not particularly good with R^2=0.88, and the corresponding natural log plot does not yield a straight line. In these calculations it was ensured that the wavelength resolution was sufficient to give reliable values for the peak position at all gap sizes. The same analysis has been carried out for all chain lengths considered here (between 2 and 150 particles) and the same behaviour is observed, that is, non-exponential scaling of the peak shift. For gap to diameter ratios greater than about 0.5 the log plot begins to look more linear, fitting an exponential only to this larger gap region gives a decay constant of about 0.40, although even here the quality of the fit is still poor and the error in the fitted decay constant is substantial. Jain *et al*. also neglect calculations at smaller inter-particle gaps from their analysis, but in this case it is because of the difficulty of describing this regime adequately with the DDA technique.

The results and analysis presented here would suggest that the plasmon peak shift is not exponential in these gap sizes. Moreover, a plot of the transverse and longitudinal plasmon peak positions as a function of the inter-particle spacing (not shown here) are not well represented by the $\frac{1}{d^3}$ dependence reported by Brongersma *et al*.[185]

Figure 4.3 shows a power law fit to the data for the 150 particle chain in figure 4.1(a). The corresponding log-log plot is very close to linear with a fitted gradient close to –1 (-0.98). The scaling law for the 150 particle chain would therefore appear to follow an inverse distance dependence. This is perhaps not surprising given that the Van der Waals interaction potential between two spheres at small distances also goes as $\frac{1}{d}$. A similar result is found for chains of other lengths, that is, the log-log plot remains linear but the gradient differs slightly from –1 to -0.89 for the dimer.

Figure 4.4 shows the calculated extinction efficiency spectra this time with a fixed gap size of 0.5 nm for varying length chains for longitudinal and transverse polarisation, respectively. The calculation for the infinitely long chain was performed using COMSOL. For clarity only a select number of chains are shown. Note that the Q_{ext} results have been

normalised to an individual particle within the chain so that direct comparison can be made with infinite chain calculation.

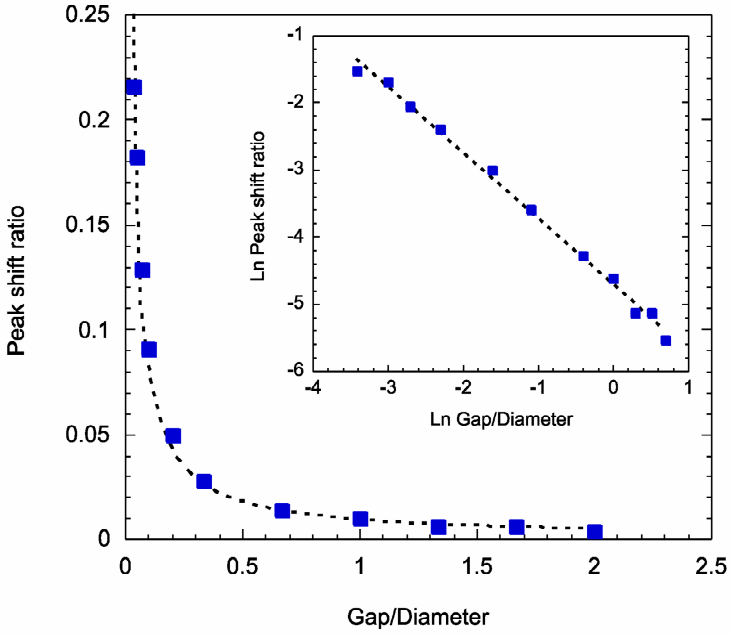

Figure 4.3. Data of figure 4.1(a) fitted to a power law dependence (dotted line). Insert shows the corresponding natural log-natural log plot.

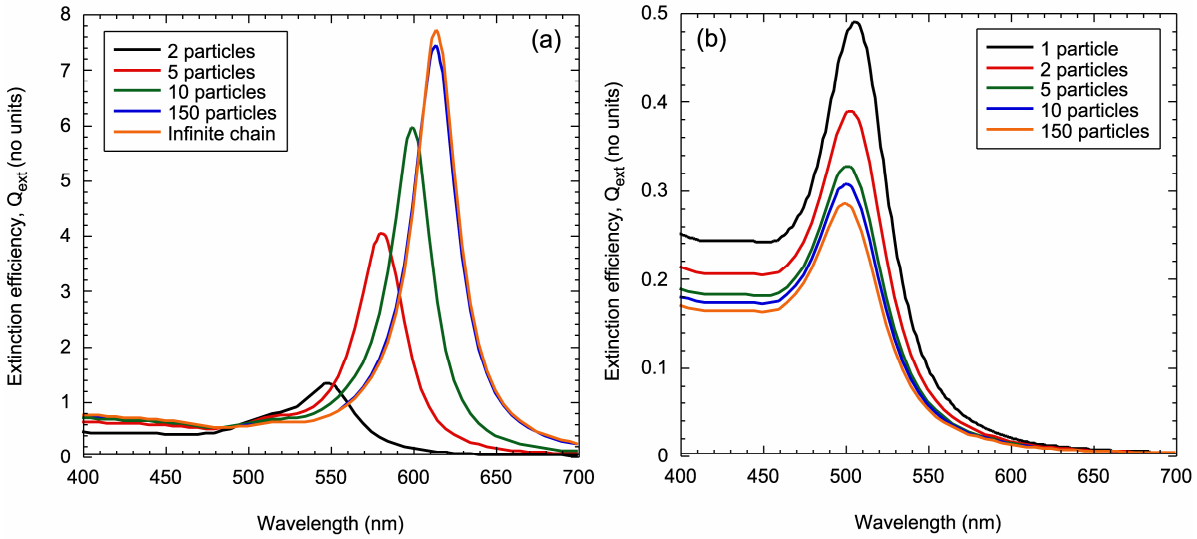

Figure 4.4. Extinction efficiency normalised per particle for **(a)** longitudinal polarisation and **(b)** transverse polarisation with a 0.5 nm inter-particle spacing.

The overall behaviour is similar to the data in figure 4.1 where the inter-particle gap was varied for fixed chain length. As the chain length increases the longitudinal plasmon peak, figure 4.4(a) shifts towards longer wavelengths, conversely, the transverse mode shifts towards shorter wavelengths tending towards 500 nm, figure 4.4(b) with increasing chain length. However, the longitudinal mode tends towards an asymptotic value with increasing length, in this case for a particle gap of 0.5 nm the peak position for an infinite chain is 614 nm. Even for a 10 particle chain the longitudinal plasmon is already close to its asymptotic value, the result for a 150 particle chain is indistinguishable to the infinite length chain.

These calculations have been repeated for different inter-particle gaps, the results are shown in figure 4.5 where the fractional peak shift is plotted as a function of chain length.

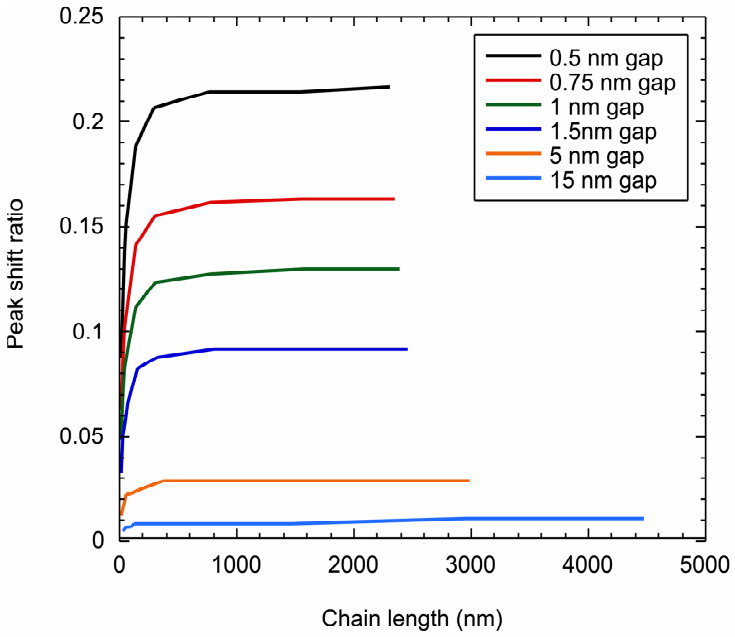

Figure 4.5. Fractional peak shift ratio for increasing length chains with different inter-particle spacings.

As expected the asymptotic value depends upon the inter-particle gap, with smaller gaps being shifted to longer wavelengths. The 30 nm inter-particle gap results are not shown in figure 4.5 because at this spacing the particles are far enough from each other that

the response looks like an isolated sphere and the plasmon peak does not shift as the chain length is increased.

The data in figures 4.4(a) and 4.5 indicate the interaction length of the plasmon resonance on the particle chain. The longitudinal plasmon resonance shifts to longer wavelengths as the chain grows because each additional particle adds to the field enhancement between particles along the entire chain. This effect begins to saturate at about 10 particles as evidenced by the fact that the resonance is close to its asymptotic value, figure 4.4(a), or in another words each particle interacts with about its 10 nearest neighbours. These results agree with those of Citrin[188] who developed a dimensionless model, applicable to any set of chain parameters, to calculate the peak plasmon modes of finite length chains and reported saturation at around 10 particles. Although they differ slightly from the experimental results of Maier *et al*.[184] who reported saturation at around 7 particles for chains of 50 nm diameter gold particles with a centre-to-centre spacing of 75 nm.

To make this idea more quantitative the data in figure 4.5 was analysed in a manner similar to figure 4.2. In this case, however an exponential that tends to an asymptote at large chain lengths needs to be fitted to the data

$$\Delta\lambda = \lambda_o e^{\frac{-m}{x}} \qquad 4.3$$

where $\Delta\lambda$ is the peak shift ratio defined above, x is the number of chain periods within the chain, m is the characteristic interaction length and λ_o is the asymptotic value for the peak shift.

It is clear from figure 4.6 that the exponential form in equation 4.3 fits the calculated data well for all but the 15 nm gap. The slope of the log plot in figure 4.6 is the characteristic interaction length defined in equation 4.3 in units of the number of chain periods and is almost constant across particle gaps below 5 nm with a value of around 2. This indicates that each particle in the chain has an interaction length of 2 particles, that is, it interacts with its 2 nearest-neighbours. This demonstrates that the resonance is localised on the chains. As the inter-particle gap is increased the characteristic interaction length for

the 5 nm (m = 1.43) and 15 nm (m = 1.23) inter-particle gaps reduces and the fit becomes poorer to the point where $m=0$ (not shown) for the 30 nm gap chain indicating that there is little to no coupling between these particles. The y-axis intercepts in figure 4.6 give the values of the asymptotic value of the peak position. They agree very well with the finite element calculations for infinite chains.

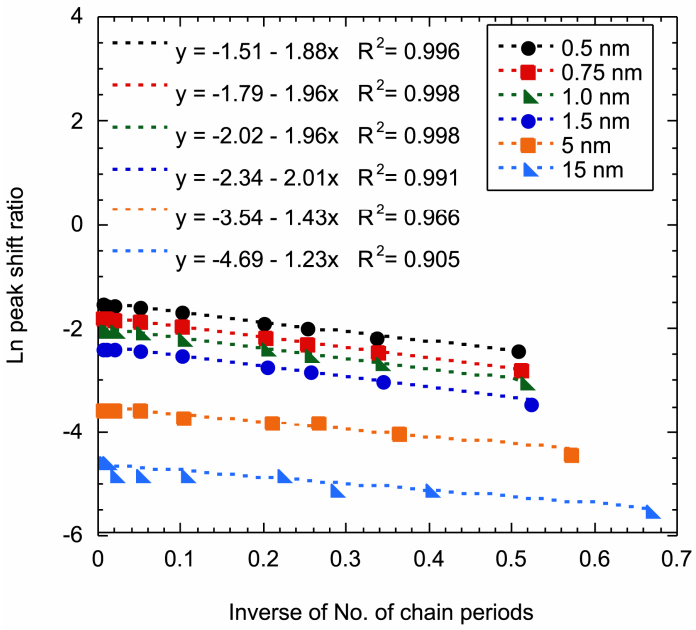

Figure 4.6. Natural log of fractional peak shift ratio versus the inverse of the number of chain periods.

Figure 4.7 shows the calculated extinction efficiency per particle with a fixed particle gap of 0.5 nm and varying chain lengths with longitudinal for transverse polarisation.

The different nature of the longitudinal and transverse resonances is obvious from this figure. Particles at the end of the chain do not contribute significantly to the longitudinal mode. The asymptotic behaviour of this mode with increasing chain length is further illustrated in figure 4.7(a), where the extinction distribution along the chain for the 50 and 150 particle chains is qualitatively the same. The rapid increase in extinction efficiency at the ends of the chain gives another indication of the interaction length of the resonance. For the 150 particle chain the extinction reaches its maximum value 5 particles from either end.

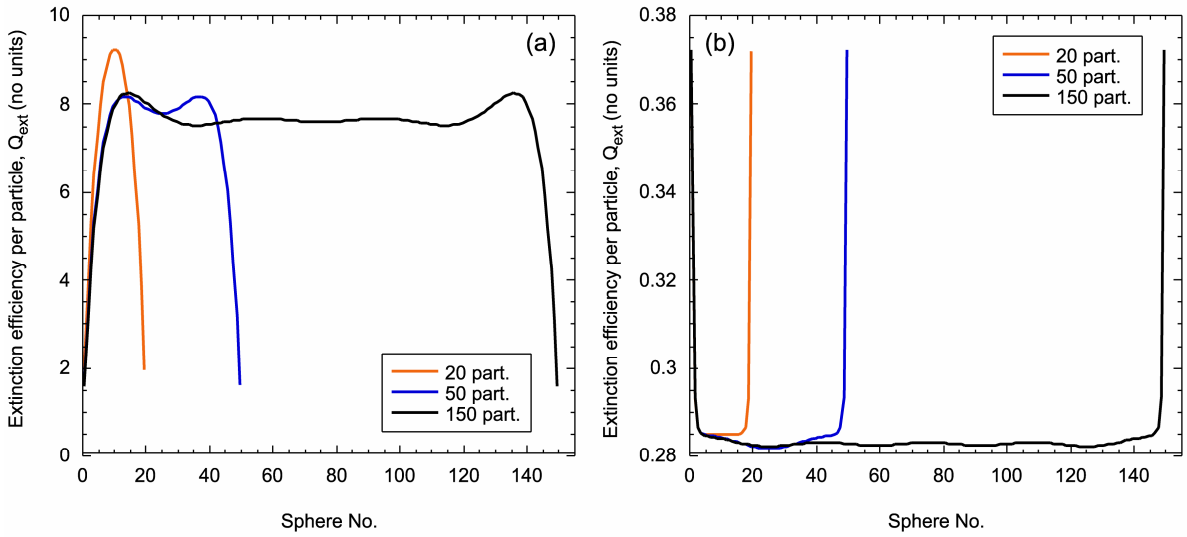

Figure 4.7. Extinction efficiency, Q_{ext} per particle for a 0.5 nm inter-particle gap with varying chain lengths and **(a)** longitudinal polarisation, **(b)** transverse polarisation.

The situation is quite different for transverse polarisation, figure 4.7(b), where the end particles dominate the extinction efficiency. The plots for all three chain lengths are qualitatively the same, and the extinction decreases very rapidly from either end of the chain. The interaction length for the transverse mode is much shorter than the longitudinal mode, or equivalently the plasmon is more localised along the chain. This would seem to be consistent with a TE guided mode in the chain which couples into the far-field only at the ends of chain. Such modes have recently been described by Sainidou and García de Abajo[124] for planar arrays of nanoparticles.

It is now possible to combine the $\frac{1}{d}$ power law and equation 4.3 to develop a scaling law, which predicts the plasmon resonance peak shift, away from the resonance of an isolated sphere, as a function of chain length and inter-particle spacing in the near-field regime as per equation 4.4.

$$\Delta\lambda = \ln A \frac{2r}{d} e^{-\frac{m}{x}} \qquad 4.4$$

Where $A = -4.7$ is the y-axis intercept of the log-log graph in figure 4.3, r is the radius of the particle and d is the inter-particle spacing. Figure 4.8 shows a correlation plot of the plasmon peak position of a 150 particle chain with varying inter-particle spacings calculated using the T-matrix technique and the scaling equation 4.4.

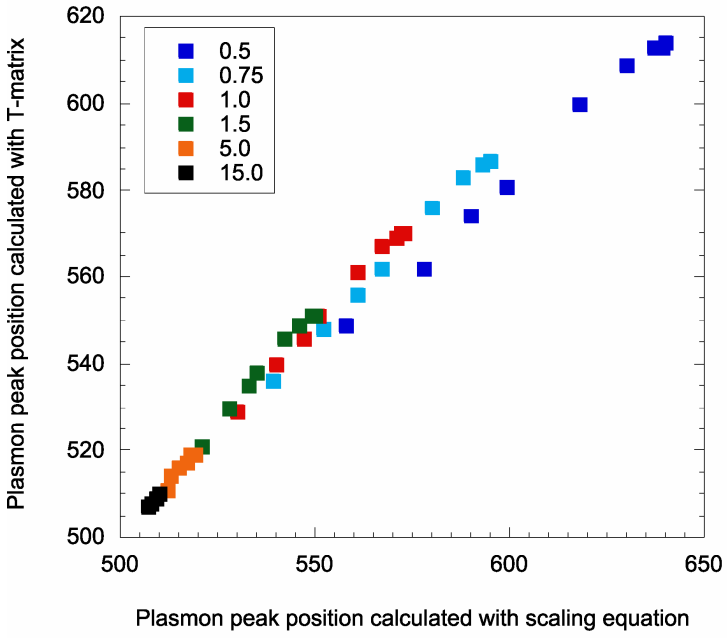

Figure 4.8. Correlation diagram of plasmon peak position calculated using the T-matrix technique and equation 4.4.

Excellent correlation exists between both sets of results for all inter-particle spacings, with only a slight difference apparent for 0.5 nm inter-particle gap. Moreover, the optical properties of individual gold spheres up to a diameter of about 100 nm are dominated by absorption and one might therefore expect the results presented here for chains of spheres to apply across a similar size range. This has been confirmed in a few representative calculations for various chain lengths and particle sizes and in fact it is the ratio of sphere diameter to inter-particle gap that determines the optical properties rather than the absolute value of either quantity.

It is now clear from the calculations presented above that for inter-particle gaps greater than about 30 nm the near-field coupling between particles is more or less zero and the 15 nm particles within the chain behave in the same way as isolated particles. This is

only true for small particles where the scattering efficiency is small. For larger particles with diameters larger than about 100 nm with inter-particle spacings larger than approximately 100 nm radiative and retardation contribute to the dipole interactions and diffractive effects become apparent. This phenomenon has been demonstrated by Zou and Schatz[104] who showed that for 100 nm diameter silver particles, increasing the inter-particle gap to about the same size as the wavelength produces additional structure in the extinction spectrum. Under suitable conditions a very sharp, narrow resonance can be produced in addition to the resonance resulting from plasmon excitation on a single particle. This effect is diffractive in character and hence requires that the individual particles have a reasonable scattering efficiency. The data presented above is in the near-field regime where coupling between the particles dominates the extinction and absorption efficiency is the determining factor.

As a final check of the calculations presented above, T-matrix calculations were performed on 150 particle chains with a constant, large particle gap with varying particle diameters. The results are shown in figure 4.9.

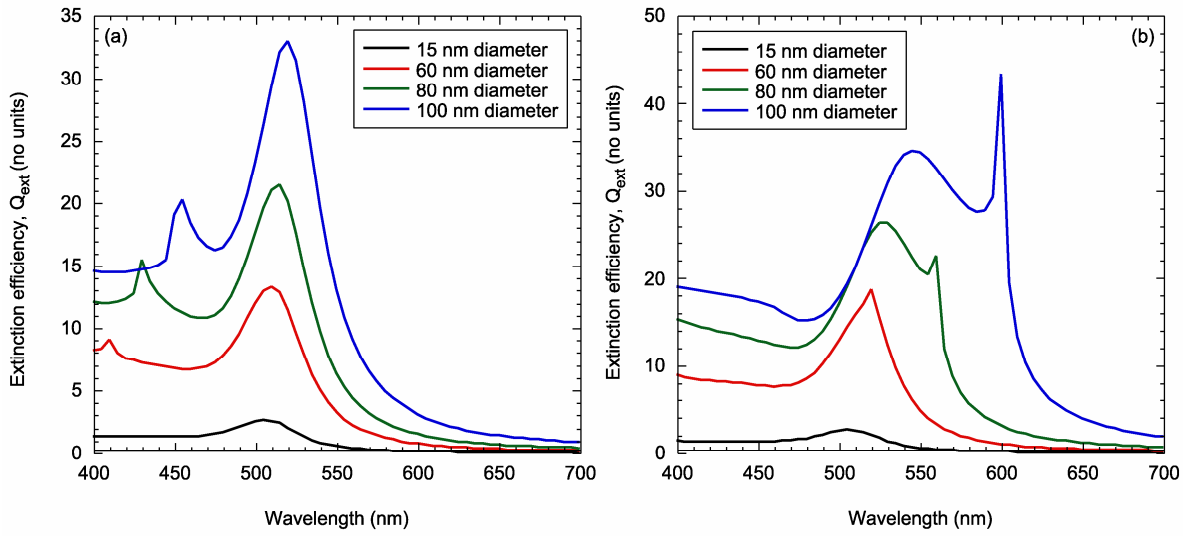

Figure 4.9. Extinction efficiency, Q_{ext} for varying diameter particles for a 150 particle chain with **(a)** an inter-particle spacing of 350 nm and transverse polarisation, **(b)** 200 nm gap and end-on polarisation.

The present calculations give results which are in agreement with those of Zou and Schatz.[104] A second much narrow resonance begins to appear as the particle diameter increases, becoming apparent for 60 nm particles with transverse polarisation and at about 80 nm for end-on polarisation. This narrow peak shifts in opposite directions for these two polarisations as the particle diameter increases further. For the longitudinal polarisation (not shown) the second sharp peak is absent at particle diameters from 15 to 100 nm. The transverse and end-on polarisations are the same, but the incident wavevectors are different, perpendicular to the chain in the former and parallel to the chain in the latter. There is no reason why these two equivalent polarisations should produce the same extinction spectrum for extended chains of particles as the phase of the excitation field is different in the two cases, and certainly Figures 4.9(a) and (b) demonstrate this. In the near-field regime, however, no difference is observed between the two wavevectors for identical polarisation even for chains that are longer than the incident wavelength. This is, at first, surprising, but is presumably a consequence of the fact that the interaction length of the resonance is small compared with the wavelength.

Zou and Schatz mention that the use of chain structures with large inter-particle spacings in SERS applications is constrained by the need for the incident and Stokes shifted wavelengths to be enhanced.[104] This is not achieved with the long chains of 100 nm diameter silver particles modelled in their work. Therefore it was hypothesised that replacing the single silver particle with a silver dimer would introduce an additional extinction peak, due to the near-field interactions of the dimer, to the already existing diffractive peak and overcome this constraint. The following section describes the results of several calculations that were performed to test this hypothesis.

4.2.2. Chain of dimers of silver nanospheres

Schematic illustrations of the three chain configurations of 100 nm diameter spherical silver particles considered within this section are shown in figure 4.10. All chains were modelled with end-on polarisation.

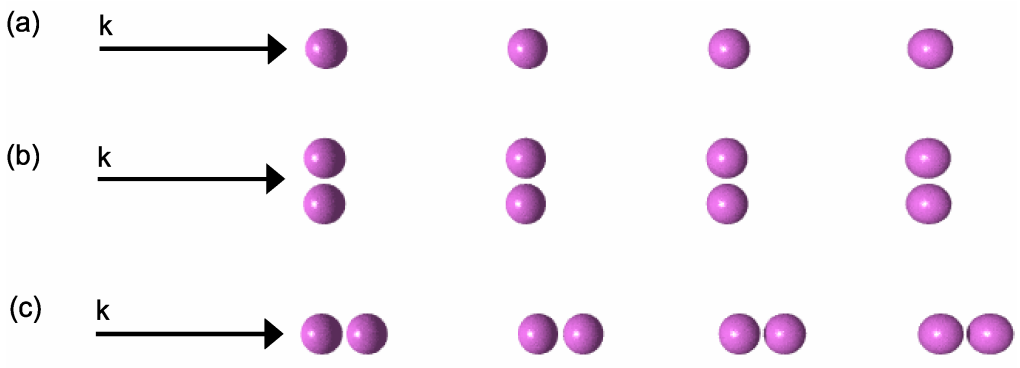

Figure 4.10. Schematic illustrations of a chain composed of 100 nm diameter silver spherical particles with **(a)** single particles and **(b)** dimers aligned perpendicular and **(c)** dimers aligned parallel to the chain axis.

The first configuration examined was a chain of single silver particles, figure 4.10(a). The calculated extinction spectra for this configuration with varying inter-particles spacings are shown in figure 4.11. This is a reproduction of one of the calculations performed by Zou and Schatz and have been reproduced here to demonstrate the diffractive behaviour of the chain.[104]

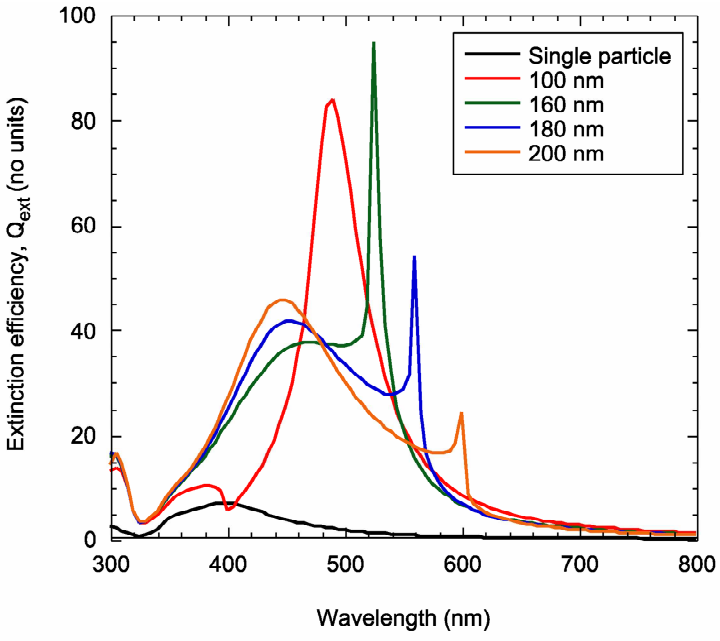

Figure 4.11. Extinction efficiency of a chain of single silver 100 nm particles with varying inter-particle spacings with 'end-on' polarisation.

It can be seen that the extinction peak initially red-shifts, from that of an isolated sphere, for the small inter-particle spacing of 100 nm. For larger inter-particle spacings the peak then blue-shifts and splits into two peaks, one broad at about 450 nm and the other sharp and narrow at a wavelength that is close to twice the inter-particle spacing, when measured between the centres of the particles. Zou and Schatz report that the sharp peaks are only produced when the real and imaginary parts of the dipole sum are close to the reciprocal of the polarisability.[104]

Prior to the replacement of the single particles in the chain with dimers the extinction spectrum of a single dimer was first examined. The wavevector was considered perpendicular and parallel to the dimer axis. Transverse (0) (perpendicular to the dimer axis), longitudinal $\left(\frac{\pi}{2}\right)$ (parallel to the dimer axis) and 45^{o} $\left(\frac{\pi}{4}\right)$ polarisations were modelled for the perpendicular wavevector configuration. The dimer was modelled with an inter-particle spacing of 3 nm. The optical response can be seen in figure 4.12.

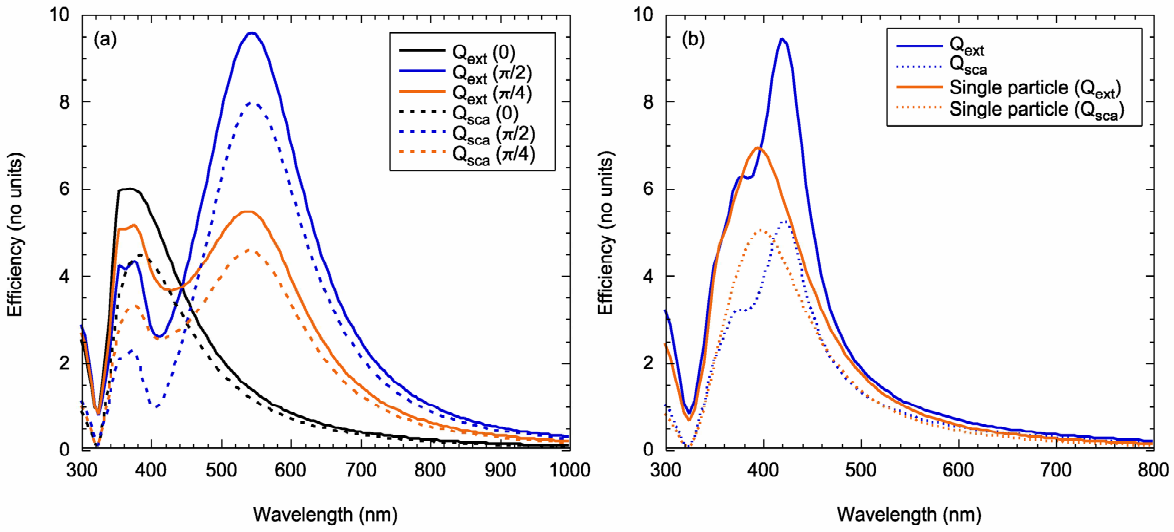

Figure 4.12. Extinction efficiency of a single dimer of 100 nm diameter spherical silver particles with an inter-particle spacing of 3 nm with the wavevector **(a)** perpendicular and **(b)** parallel to the dimer axis.

For the perpendicular dimer, figure 4.12(a), with transverse polarisation the extinction peak blue-shifts to 370 nm compared to a single particle resonance of 395 nm (orange line

in figure 4.12(b)). Two extinction peaks are produced for longitudinal polarisation with the smaller of the peaks located at approximately the same position as the transverse peak and the larger of the peaks red-shifted to 545 nm. For the parallel dimer, figure 4.12(b), the single particle extinction peak splits into two peaks with the smaller peak located at 380 nm and the larger peak red-shifted, from the single particle extinction peak, to 420 nm. The dimer behaviour can again be explained in terms of the hybridisation model. In this case, however scattering dominates the extinction spectra for both transverse and longitudinal polarisations. A large scattering component is to be expected in 100 nm diameter particles due to higher order contributions and is essential in the production of the diffractive phenomenon of the chain.

A 200 particle chain containing dimers that were aligned perpendicular to the chain axis, figure 4.10(b), was then modelled. Varying inter-dimer and inter-particle spacings were examined with end-on polarisation. Both transverse (perpendicular to the dimer axis) and longitudinal (parallel to the dimer axis) polarisations were modelled for this configuration and the calculated extinction spectra are shown in figures 4.13 and 4.14, respectively.

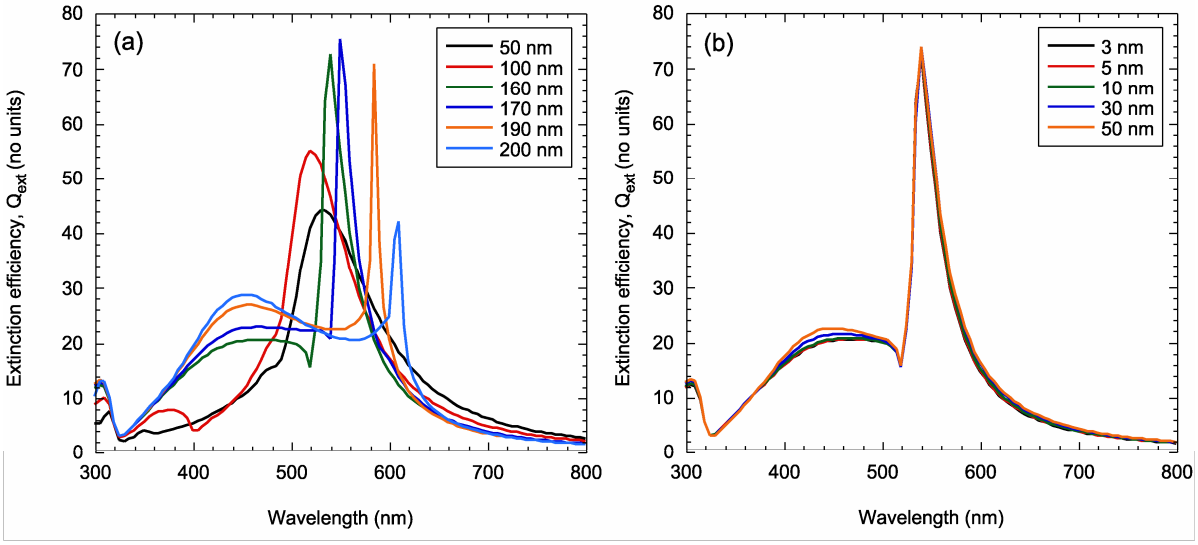

Figure 4.13. Extinction efficiency of a chain of dimers, with the dimer axis oriented perpendicularly to the chain axis, for transverse polarisation for **(a)** constant inter-particle gap of 3 nm and **(b)** constant inter-particle gap of 160 nm.

Diffractive effects dominate for transverse polarisation as can be seen from figure 4.13(a), which shows the extinction spectra for a chain with a constant inter-particle gap of 3 nm and inter-dimer gaps varying between 50 and 200 nm. It can be seen that for inter-dimer spacings larger than 100 nm, the extinction spectra splits into two peaks and produces a very sharp peak at approximately twice the wavelength of the inter-dimer spacing, when measured between the centres of the dimers. This is the same behaviour that is produced from a single chain of spheres as shown in figure 4.11. Figure 4.13(b) shows the extinction spectra for a constant inter-dimer spacing of 160 nm and inter-particle spacings varying between 3 and 50 nm. The previous section described the red-shifting of the dimer plasmon resonance as the inter-particle spacing is reduced, due to greater hybridisation between the particles. One would then expect the extinction peak from figure 4.13(b) to red-shift as the inter-particle spacing is reduced from 50 nm to 3 nm. However, this is not the case and the extinction peak effectively remains in the same position over this range of inter-particle spacings indicating that the dimer has little influence on the optical response in this chain formation.

The opposite is true for longitudinal polarisation as can be seen from figure 4.14.

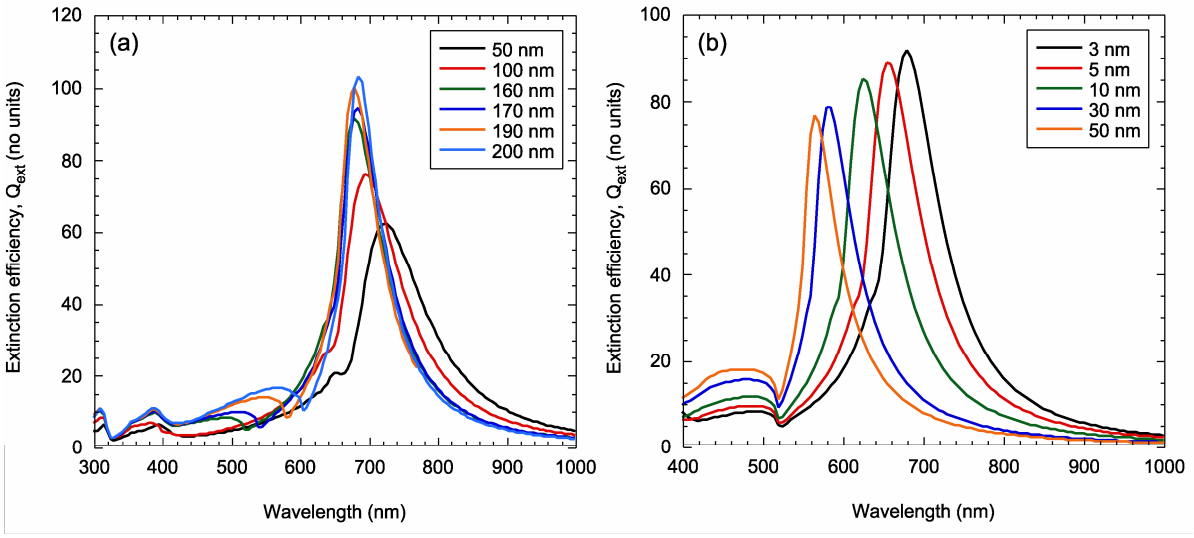

Figure 4.14. Extinction efficiency of a chain of dimers, with the dimer axis oriented perpendicularly to the chain axis, for longitudinal polarisation for **(a)** constant inter-particle gap of 3 nm and **(b)** constant inter-particle gap of 160 nm.

In figure 4.14(a) the inter-particle spacing is held constant at 3 nm and the inter-dimer spacing is varied between 50 and 200 nm. For inter-dimer spacings greater than 100 nm the extinction peak converges to approximately 690 nm. Longitudinal polarisation of the single dimer produced a second extinction peak at 545 nm. The chain described in figure 4.14 contains 200 particles and based on the discussion in section 4.2.1, which described the peak red-shift towards an asymptotic value as a function of chain length, it would seem reasonable to attribute the production of the 690 nm extinction peak to the red-shifting of the individual dimer peak with increasing chain length. This is not the case for inter-dimer spacings of 100 nm and less because at these spacings the dimers are now close enough to each other to allow near-field interactions, which will red-shift the extinction peak as the inter-dimer spacings are reduced. Figure 4.14(b) demonstrates that dimer effects dominate the extinction spectra for longitudinal polarisation. In this case the inter-dimer spacing is held constant at 160 nm and the inter-particle spacing is varied between 3 and 50 nm. As the inter-particle spacing is reduced from 50 to 3 nm the extinction peak red-shifts as one would expect from a dimer.

The final configuration examined was a 200 particle chain containing dimers that were aligned parallel to the chain axis with end-on polarisation, as per figure 4.10(c). Figure 4.15 shows the calculated extinction spectra for varying inter-dimer (4.15(a)) and inter-particle (4.15(b)) spacings. In this case partial diffractive effects are present, however not to the same extent produced by the perpendicular dimers with transverse polarisation.

In figure 4.15(a) the inter-particle spacing is kept constant at 3 nm and the inter-dimer spacing is varied between 50 and 300 nm. Additional smaller extinction peaks are present for inter-dimer spacings between 50 and 160 nm however, these are not of the same magnitude as those produced by the chain containing perpendicular dimers with transverse polarisation. In that case the 160 nm inter-dimer spacing produced the optimum extinction peak. This would indicate that the parallel alignment of dimers suppresses the diffractive effect.

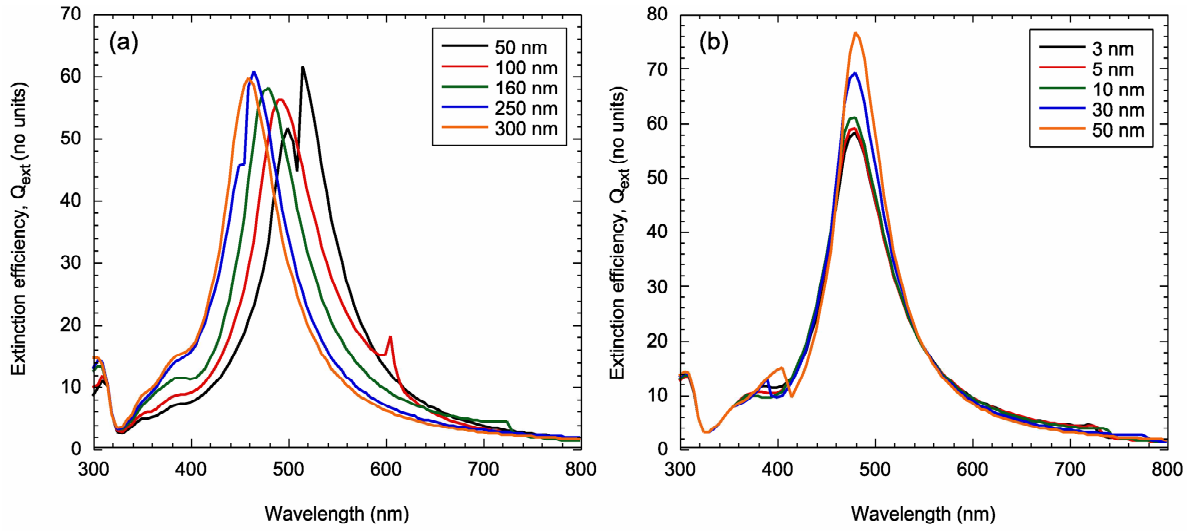

Figure 4.15. Extinction efficiency of chain of parallel dimers for **(a)** constant inter-particle gap of 3 nm and **(b)** constant inter-dimer gap of 160 nm.

In figure 4.15(b) the inter-dimer spacing was held constant at 160 nm and the inter-particle spacing was increased from 3 nm to 50 nm. There is no red-shifting of the peak with decreasing inter-particle spacing, indicating that dimer effects are not dominant. Moreover, a small additional extinction peak is produced when the inter-particle spacing is increased to 50 nm. Increasing the inter-particle spacing beyond 50 nm will result in the production of a chain of single spheres as per figure 4.10(a) and the extinction spectra would approach that shown in figure 4.11.

The chain containing perpendicular dimers is the most interesting of all the chain configurations considered in this section as two large extinction spectra are produced at wavelengths well separated from each other as determined by the direction of polarisation. To enhance both the incident and Stokes shifted wavelengths both resonances need to be produced at the same time. This is possible if polarisation at 45^{o} is used and this effect can be seen from figure 4.16. In this case the optimum perpendicular dimer chain with an inter-dimer spacing of 160 nm and an inter-particle spacing of 3 nm is polarised with transverse, longitudinal and 45^{o} polarisations. Two extinction peaks at approximately 545 and 690 nm are produced with 45^{o} polarisation and although the magnitude of the extinction efficiency is approximately half of that produced by the individual transverse and longitudinal polarisations, it is nevertheless still significant.

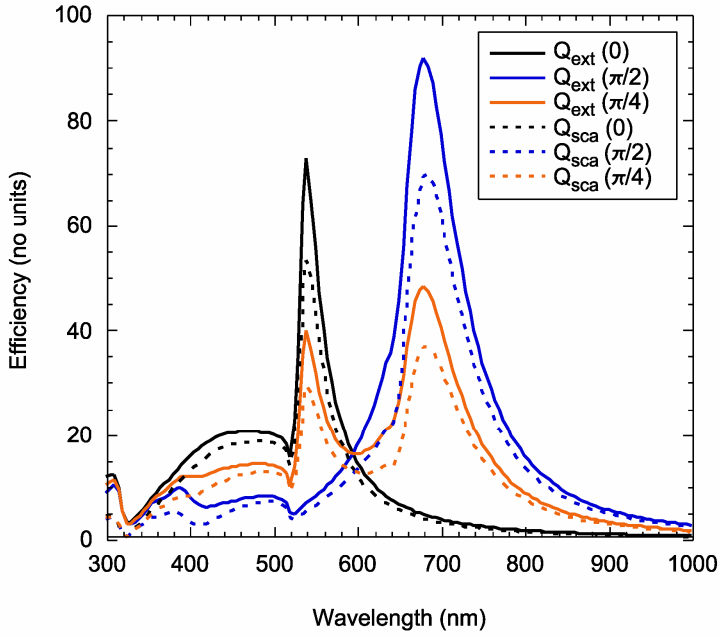

Figure 4.16. Efficiency response from a chain of perpendicular dimers with an inter-dimer spacing of 160 nm and an inter-particle spacing of 3 nm for transverse (0), longitudinal $\left(\frac{\pi}{2}\right)$ and 45° $\left(\frac{\pi}{4}\right)$ polarisation.

4.3. Conclusions

In summary, the T-matrix technique was first used to model the optical response of varying length chains of 15 nm diameter gold spheres in both the near- and far-field regimes. In the near-field regime the inter-particle gaps were small enough to ensure that the electric fields of the spheres were strongly coupled. Decreasing the inter-particle spacing for a fixed length chain caused the plasmon resonance to split into two separate peaks and blue-shift in the case of transverse polarisation and red-shift in the case of longitudinal polarisation. However, the peak splitting phenomenon did not follow the $\frac{1}{d^3}$ dependence reported for other chains nor did the red-shifted peak follow an exponential dependence upon gap size that has been associated with dimers. The inverse cube dependence is predicted by a model where the particles are represented by interacting point dipoles. The results from the calculations performed here suggest that higher order terms

cannot be neglected. The number of orders required to reach convergence in the T-matrix calculations supports this conclusion. The exponential dependence has been predicted in DDA calculations and could be due to difficulties in describing the rapidly varying electric fields in the gap region using a volume discretisation method. The peak shift does, however, follow a power law dependence on the gap distance giving a straight line in log-log plots. This dependence is close to $\frac{1}{d}$ for all chain lengths although there is some variation with chain length: the exponent varies from –0.98 to –0.89 for 150 and 2 particle chains, respectively. At short distances the Van der Waals interaction (effectively the interaction between plasmon modes) for two spheres also varies as $\frac{1}{d}$.

Increasing the chain length for a constant inter-particle gap caused the longitudinal plasmon peak to exponentially approach an asymptote, the value of which depended upon the inter-particle spacing. For inter-particle gaps below 5 nm the asymptote was reached by around 10 particles and had a characteristic interaction of 2 particles, demonstrating the localised nature of the resonance of the chain within the near-field regime. This behaviour appears to be quite general and applicable to all chains with a gap less than 5 nm, that is, in the near-field regime.

In the far-field regime 150 particle chains with inter-particle gaps similar to the wavelength of the incident light were modelled. It transpired that the production of a second very sharp, narrow peak was not evident in chains with small particles where the scattering cross-sections are small and only became evident for larger particles with diameters of around 60 nm for perpendicular polarisation and around 80 nm for end-on polarisation. No second peak was evident for parallel polarisation for sphere diameters ranging from 15 to 100 nm. Chains containing 200 silver particles of 100 nm in diameter were also modelled in the far-field regime. Replacement of a single particle with a dimer enabled both diffractive and dimer effects to contribute to the optical extinction spectra. Far-field diffractive effects dominated the extinction spectra for dimers that were aligned perpendicular to the chain axis with transverse polarisation. Conversely near-field dimer effects dominated the extinction spectra for longitudinal polarisation.

Chapter 5

5. Optimisation of plasmonic heating in gold nanoshells

The effect of rapid formation of colloidal crystals from localised-plasmonic heating of nanospheres during laser irradiation was examined in Chapter 3. Nanoshells and nanorods have the ability to exploit these localised heating effects far more efficiently than nanospheres because their absorption cross-sections far exceed their geometric cross-sections. Moreover, by varying their aspect ratio the plasmon resonance can be tuned into the infrared part of the spectrum. Considerable attention has been paid to this tuneability of the optical response of nanoshells and a variety of applications explored which exploit the temperature change induced by the strong plasmon-induced surface heat flux.[27, 56, 189] In previous work, heat has been applied to gold nanoparticles via laser-induced methods to examine their energy absorption and relaxation times within aqueous solutions[190, 191] and gel matrices.[192] The relationship between absorption maximum and nanoshell geometry is now well established. While temperature changes as a result of incident illumination have been calculated[53, 59, 191] and/or measured[55, 59, 191, 193] for these particles, no work has been performed to determine geometries that optimise this temperature change. Moreover, conductive heat transfer models have been used in the past to calculate the temperature change of nanoparticles within an aqueous medium,[53, 191] however, the presence of bulk fluid motion was not taken into account within these models.

In this chapter the optimum nanoshell geometry that provides the maximum thermal equilibrium temperature under irradiation by sunlight and laser light is determined.

Absorption efficiencies were calculated using the BHCOAT computer program.[13] This is an implementation of Mie theory[68] and is, in principle, an exact solution to the scattering of electromagnetic waves by spherical particles. The surface heat flux of the nanoshells based upon their absorption efficiency and the intensity of the incident light were then calculated. A convective heat transfer model was developed to calculate the equilibrium temperature of each nanoshell based upon the surface heat flux produced after irradiation. From this the optimum nanoshell geometry that produced the maximum thermal equilibrium temperature was determined.

5.1. Methods

5.1.1. Calculation of absorption efficiency and heat flux

The computer program BHCOAT, which is described by Bohren and Huffman,[13] was used to calculate the extinction efficiency from the nanoshells. BHCOAT calculates scattering by using Mie theory[68] to provide numerical solutions for scattering efficiency, Q_{sca}, absorption efficiency, Q_{abs}, and extinction efficiency, Q_{ext} ($Q_{ext} = Q_{abs} + Q_{sca}$). As described in Chapter 2 Mie theory[68], in principle, provides an exact solution to the scattering problem for coated spheres or shells. In practice, however, the infinite multipole expansion must be terminated at some point and the exactness of the solution is therefore determined by how quickly this series converges. For the shells considered here only the first one or two terms make a significant contribution and even for the largest particle sizes, series convergence is not expected to be a problem.

More problematic in BHCOAT is the potential to calculate very large numbers, which exceed computational limits. This occurs because the scattering coefficients for a shell, unlike a solid sphere, cannot be written in such a way that the functions of complex arguments are ratios, allowing the Riccati-Bessel functions to have real arguments. This can lead to numerical difficulties if the shell is particularly large or highly absorbing, that is, has a large imaginary part of the refractive index. To prevent these numerical problems Bohren and Huffman[13] recommend that the imaginary component of the size parameter

multiplied by the inner or outer shell radius should not exceed 30. For the largest shells examined here, this limit is approached with maximum values of around 10. To determine whether the calculated scattering efficiencies are subject to these numerical problems calculations for solid spheres using the BHCOAT algorithm, where the inner and outer spheres are composed of the same material, were compared to calculations using the BHMIE[13] algorithm from Bohren and Huffman, which is the exact solution for a solid sphere. The latter does not suffer with the numerical problems described above and for all particle sizes the two algorithms give identical results.

Nanoshells with diameters of 30 nm, 50 nm, 80 nm, 110 nm, 200 nm, 250 nm, 300 nm, 350 nm and 400 nm with aspect ratios of 0, 0.2, 0.4, 0.6, 0.8, 0.85, 0.9, 0.925 and 0.95 were simulated. The aspect ratio is the ratio of the inner sphere diameter to the outer nanoshell diameter. Therefore an aspect ratio of 0 describes a solid gold sphere, and a 0.95 aspect ratio is one where the shell thickness is 5 % of the diameter of the sphere. The shells were simulated as immersed in water, with water also making up the core of the shell, by modifying the frequency dependent refractive index of bulk gold[179] so that it was relative to water. Damping of the plasmon resonance from surface scattering has not been considered. The refractive index of water was assumed to be frequency independent and non-absorbing. This is justified as the value of refractive index varies by only 2% across the spectrum investigated here.[194] Calculations were performed on each shell between wavelengths of 300 nm and 1500 nm in 1 nm increments. This range of wavelengths was chosen as they include the surface modes for all of the particle geometries and hence include the dominant absorption bands.

Assuming that all of the energy absorbed from the incident light is converted to thermal energy then, under steady-state conditions, the power absorbed by and simultaneously transferred out of a shell is given by

$$\frac{dQ}{dt} = \int_{300}^{1500} C_{abs} E_{\lambda} . d\lambda \qquad 5.1$$

and the surface heat flux is

$$\frac{dq}{dt} = \frac{1}{4}\int_{300}^{1500} Q_{abs} E_{\lambda} . d\lambda \qquad 5.2$$

where $\frac{dQ}{dt}$ is the heat radiated out of the shell (W/particle), C_{abs} is the absorption cross section, E_{λ} is the spectral irradiance of the light source ($Wm^{-2}nm^{-1}$), λ is the wavelength of light, and $\frac{dq}{dt}$ is the heat flux (Wm^{-2}) at the nanoparticle surface.[195]

Two scenarios were considered for the incident radiation. The first was to simulate irradiation of the shells with 800 Wm^{-2} of standardised sunlight.[196] The second was to simulate irradiation of the shells with a 10 mW continuous wave laser with a 0.5 mm diameter spot size, providing a laser intensity of 50.9 kWm^{-2}. It was assumed that the wavelength of this laser could be tuned to the wavelength of maximum absorption of the shells.

These sources of radiation correspond to two potential applications of plasmonic effects in nanoparticles such as wavelength selective solar glazing and localised heating under laser irradiation for therapeutic treatment. There are also two very different scenarios for the laser irradiation. Firstly, the irradiation times might be short, such as in the case of a pulsed laser, and transient effects occur in the particles and/or the surrounding medium. Secondly, irradiation times may be sufficiently long so as to allow the particles to equilibrate with the surrounding fluid. The latter of these two cases will be examined here.

5.1.2. Relationship of heat flux to shell temperature

Previous work[53, 191] on transient heating and cooling has focused on the temperature of the particle itself. However, it is not necessarily the high particle temperature that would cause it to have functionality in, for example, thermal therapy. Rather, it is the temperature that the particle imparts to its immediate surroundings, which is determined by the surface heat flux $\frac{dq}{dt}$. Once $\frac{dq}{dt}$ is known, the steady-state particle temperature can be estimated using a model that accounts for heat loss by a suitable mechanism.

In order to gain an upper limit on the equilibrium temperature the calculation was first performed for isolated shells in vacuum where the surroundings are at an ambient temperature of 293 K. This is a relatively trivial calculation where the heat loss mechanism is entirely radiative.

The equilibrium temperature due to radiative cooling alone can be calculated by setting the absorbed power equal to that radiated by a black body at temperature T_p [197]

$$\frac{dQ}{dt} = e\sigma 4\pi r_p^2 (T_p^4 - T_{surr}^4) \qquad 5.3$$

where e = 0.9 and is the emissivity of the shell, σ is the Stefan-Boltzmann constant[195] ($5.67\times10^{-8}\,Wm^{-2}K^{-4}$), r_p is the radius of the shell, T_p is the temperature of the shell and T_{surr} is the ambient temperature of the surroundings ($293\ K$).[197] Since $\frac{dQ}{dt}$ can be calculated from equation 5.1, T_p can be extracted in this case.

The second step is to calculate the temperature of the shell whilst it was immersed within a surrounding water medium. To do this it is assumed that there is a constant rate of heat generation per unit volume. For the larger particles with shells thicker than the mean free path of gold (31nm[198]) this assumption is justified as the thermal conductivity of gold is very high at $315\ Wm^{-1}K^{-1}$.[198] For the smaller particles with shell thicknesses smaller than the mean free path a more sophisticated approach may be adopted to take into account ballistic conduction. However, this is not necessary as the temperature gradient within the particle is extremely small as it is.

Calculation of the equilibrium temperature of the shell under irradiation is then relatively straightforward from the appropriate heat transfer equation where the surrounding water medium is assumed to be an infinite bath at an ambient temperature of $293\ K$. The shells are assumed to be a sufficiently dilute suspension so that they do not interact with one another either thermally or through near-field plasmonic interactions.

Heat transfer from the shell to the surrounding water is via conduction in still water (no bulk fluid motion) and by convection in moving water.[195] Within this scenario it is

assumed that the temperature change of the shells is large enough to overcome the resistance of the water molecules to movement and consequently initiate natural convection currents.[195] Convection as opposed to conduction was used as the heat transfer mechanism.

The convection heat transfer mechanism can be described by the following equation.[197]

$$\frac{dQ}{dt} = h4\pi r_p^2 (T_p - T_{surr}) \qquad 5.4$$

where h is the total heat transfer coefficient of still water.

The difficulty in this approach lies in finding an appropriate value for the heat transfer coefficient of water. From the literature, typical values of h for still water range between 50 to 10,000 $Wm^{-2}K^{-1}$. However, h is not solely a property of the water and its value is determined from experiment and will depend upon a combination of the shell surface geometry, the water properties and the motion of the water, whether forced or still.[195]

In an attempt to find an appropriate value of h, empirical results from various nanofluid studies were considered. To our knowledge, no work has been performed to determine h for gold nanoparticles within a nanofluid. However, Khanafer *et al*. have modelled h for natural convection in a nanofluid for various circumstances, such as varying Grashof numbers and volume fractions.[199] Using the most appropriate circumstances that would be applicable to this model h was calculated to be around 520 $Wm^{-2}K^{-1}$. In another study[200] h was found to be approximately 240 $Wm^{-2}K^{-1}$, corresponding to the heating of a nanofluid of titanium dioxide nanoparticles for 500 seconds.

The use of different empirically measured values of h within equation 3.8 will have the effect of altering the calculated temperature of the shell, however this will not detract from the main aim of this chapter, which is to determine the optimum shell geometry to maximise surface heat flux. Therefore, after examining the h values from literature and empirical studies, it was decided that a natural convection heat transfer coefficient of 240 $Wm^{-2}K^{-1}$ will be used in this model.

5.2. Results and discussion

5.2.1. Optimum shell geometry to produce maximum surface heat flux

As described in Chapter 1 it is the aspect ratio of the shell that is the dominating influence on the wavelength at which maximum absorption occurs.[27] However, for a fixed aspect ratio, the wavelength at which maximum absorption occurs nevertheless also shows some dependence on shell diameter. As the shell diameter increases the peak begins to broaden and larger shells tend to scatter incident light more efficiently and absorb less compared with smaller diameters.[201] This can be seen in figure 5.1 where absorption and scattering of 80 nm and 400 nm diameter gold spheres are compared. An 80 nm diameter sphere absorbs approximately 2.5 times the amount it scatters, whereas a 400 nm diameter sphere scatters approximately 2.5 times the amount it absorbs.

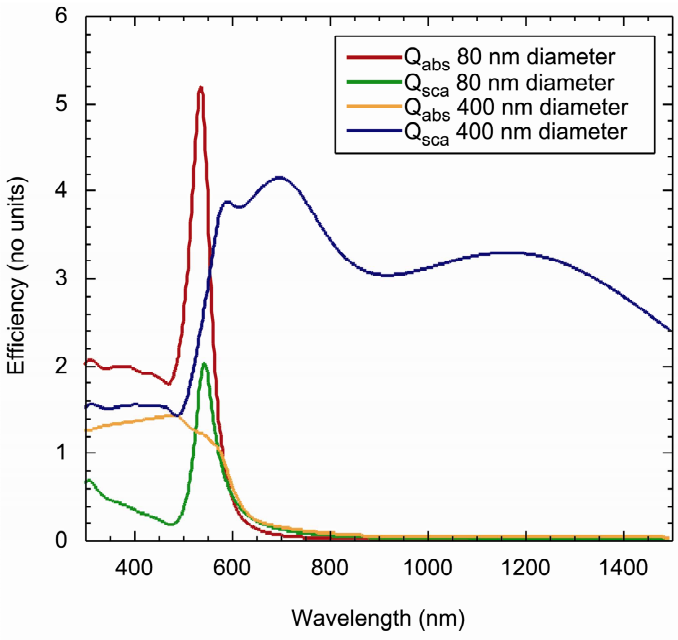

Figure 5.1. Absorption efficiency, Q_{abs} and scattering efficiency, Q_{sca} for 80 nm and 400 nm spheres (aspect ratio = 0).

The peak absorption efficiencies as a function of shell diameter for fixed aspect ratios are shown in figure 5.2. The optimum absorption efficiency of $Q_{abs} \approx 19$ occurs at 846 nm for a diameter of 50 nm and an aspect ratio of 0.9. For a solid sphere of the same diameter the peak absorption efficiency is almost a factor of 5 smaller with $Q_{abs} \approx 4$. For all aspect ratios the absorption efficiency falls rapidly beyond shell diameters of about 100 nm because these larger particles scatter more efficiently.

Assuming that the laser irradiation can be tuned to the absorption maximum, equation 5.2 shows that the surface heat flux under the laser radiation is directly proportional to Q_{abs}, and can therefore also be shown in figure 5.2.

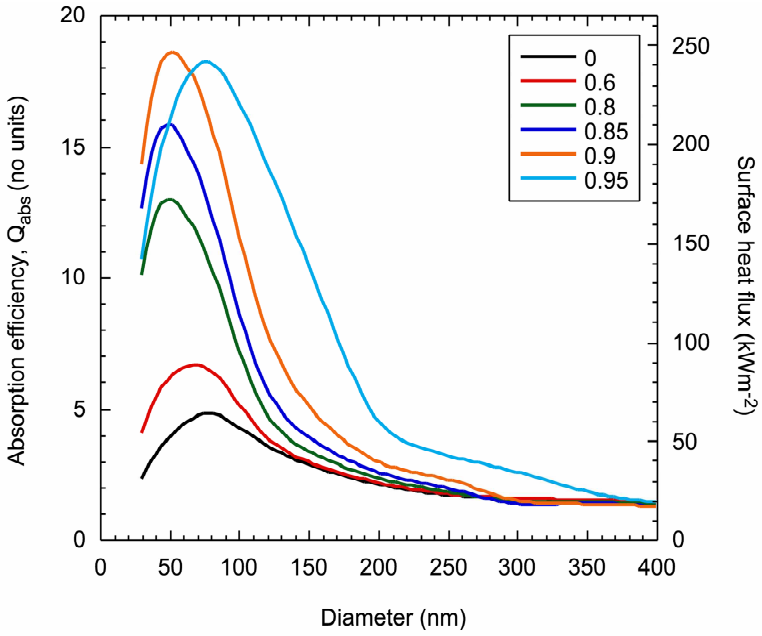

Figure 5.2. Peak absorption efficiencies, Q_{abs} as a function of shell diameter for fixed aspect ratios and associated surface heat flux when irradiated with a laser.

It can be seen that the 50 nm, 0.9 aspect ratio shell produces a maximum surface heat flux of 245 kWm^{-2}, significantly larger than the maximum 50 kWm^{-2} produced by a sphere of about the same diameter. In this case the optimum geometry is the same as that which produced the maximum absorption.

The situation is slightly different for sunlight irradiation as described in figure 5.3. The maximum surface heat flux of approximately 175 Wm^{-2} occurs for a diameter of 80 nm and an aspect ratio of 0.8. Note that the optimum surface heat flux, in this case, does not correspond to an aspect ratio that gives the optimum absorption efficiency. Moreover, a solid sphere of diameter 110 nm gives a nearly comparable surface heat flux of 150 Wm^{-2}.

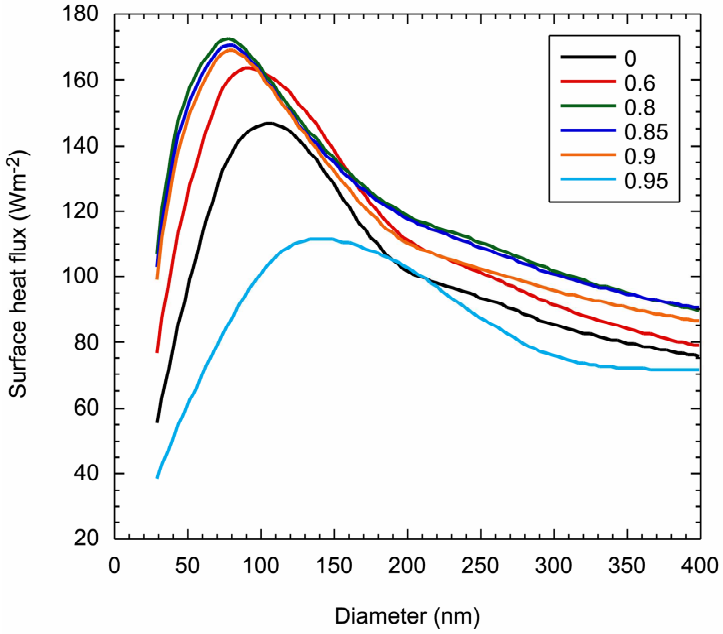

Figure 5.3. Variation of surface heat flux versus shell diameter for fixed aspect ratios when irradiated with sunlight.

The cause of this effect can be explained with the aid of figure 5.4, which shows the variation in peak absorption efficiency, Q_{abs} as a function of aspect ratio for a shell of 50 nm diameter. The large Q_{abs} values result from the production and hybridisation[22] of surface plasmon modes at the shell-dielectric interfaces. The strength of the surface mode is determined by the size of the imaginary component of the material dielectric constant. A material with a small imaginary component will have a large, narrow absorption peak whereas a material with a large imaginary component will have a small, broader absorption peak.[20] It can be seen that for the solid sphere the absorption maximum occurs at about 530 nm whereas for the 0.9 aspect ratio shell it is at 846 nm. Since the majority of the Sun's intensity falls between about 400 nm and 700 nm[197], larger diameter, thicker shells with a

smaller aspect ratio are best suited to converting sunlight to heat flux. Indeed, the use of shells compared with solid spheres has limited advantage in this type of application.

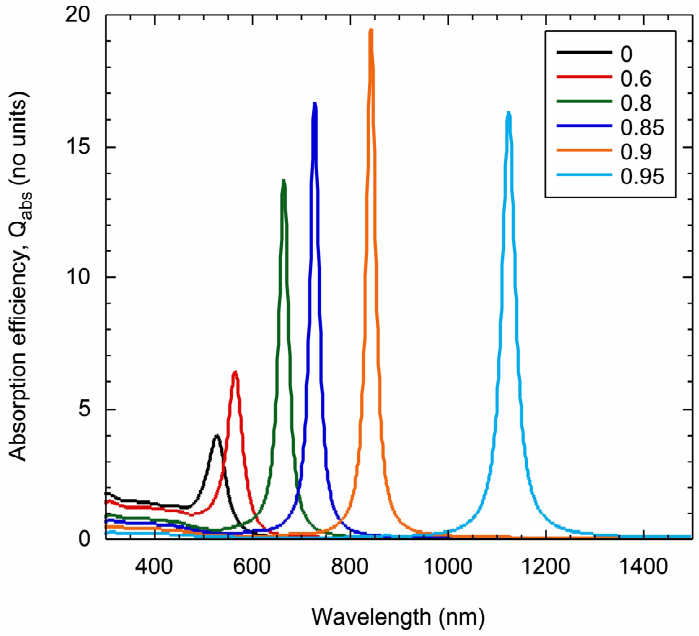

Figure 5.4. Absorption efficiencies for a 50 nm diameter shell with varying aspect ratios.

On the other hand, proposed therapeutic applications, which use monochromatic radiation in the near-infrared, may be best served by smaller diameter, thinner shells with larger aspect ratios. Although for the 0.95 aspect ratio shell Q_{abs} is around 16 and the shell thickness is 2.5 nm. At these dimensions plasmon damping will become apparent and the imaginary part of the dielectric constant will increase forcing a broadening and consequent reduction of the absorption peak

The results from figures 5.2 and 5.3 demonstrate how precisely the surface heat flux of a shell can be controlled. That is, by varying the shell thickness, the absorption efficiency can be optimised and consequently the amount of surface heat flux produced by the shell can be engineered to an optimum value.

5.2.2. Heat transfer by radiation

Using equation 5.3, the equilibrium temperature for the gold shells in vacuum, was calculated from the heat flux results shown in section 5.2.1. The results for illumination by sunlight and a laser are shown in figures 5.5 and 5.6, respectively. It should be noted that temperature induced modifications to the dielectric function and particle phase were not taken into consideration in this model.

Under irradiation by sunlight the maximum equilibrium temperature of 535 K is reached for an 80 nm shell with an aspect ratio of 0.8. Whereas under laser illumination a maximum equilibrium temperature of 1775 K occurs for the 50 nm diameter shell with an aspect ratio of 0.9. The optimum geometries follow directly from the heat flux calculations of the preceding section. Obviously, the ability to tune the laser wavelength to the peak absorption wavelength gives a much larger final temperature. No account is taken in these calculations of melting of the shell, which is known to occur under sufficiently intense laser illumination.[57]

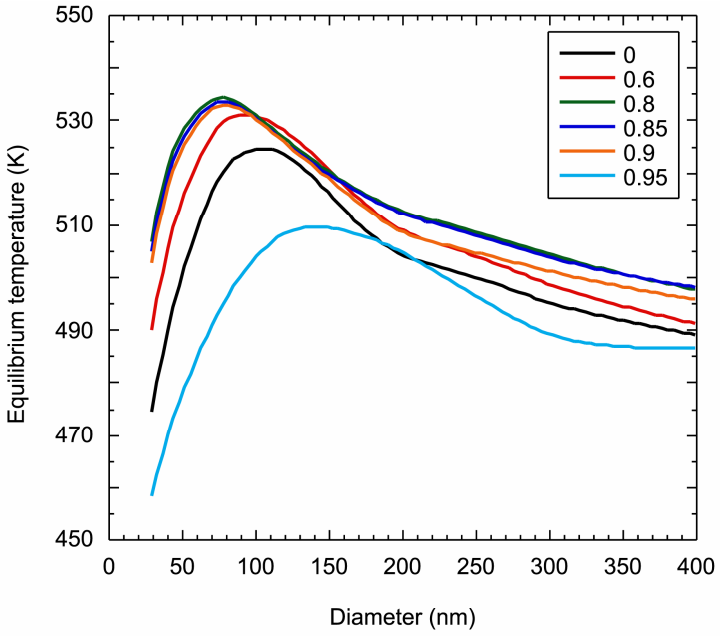

Figure 5.5. Calculated shell temperature after irradiation by sunlight in vacuum.

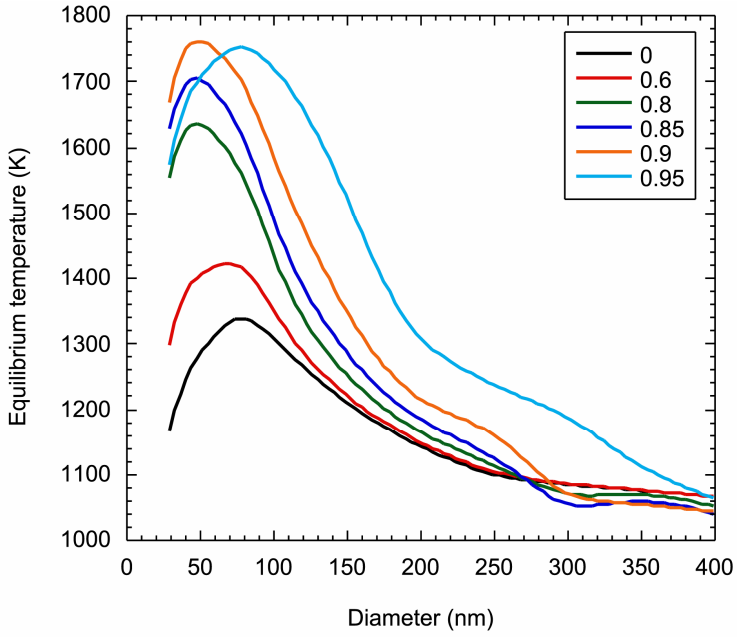

Figure 5.6. Calculated shell temperature after irradiation by laser in vacuum.

5.2.3. Heat transfer by convection

The calculated temperatures for shells suspended in water and irradiated with sunlight and a laser are shown in figures 5.7 and 5.8, respectively.

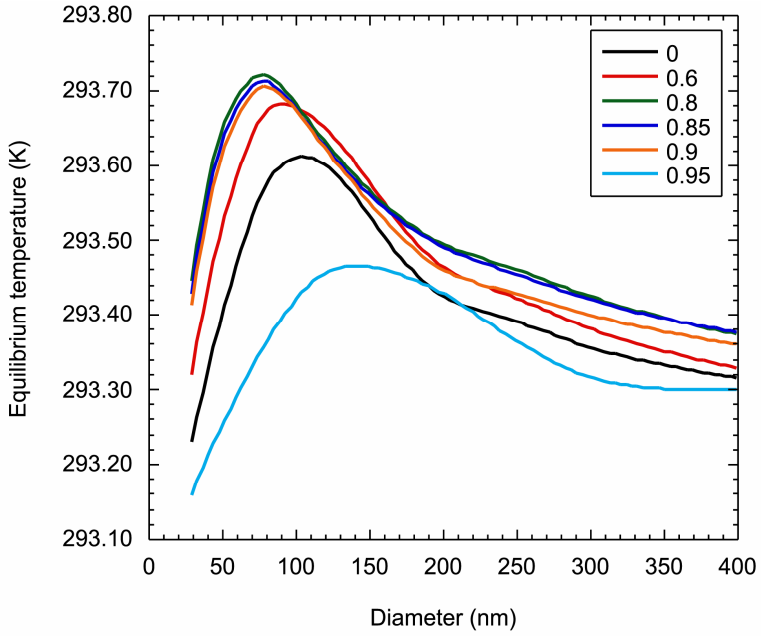

Figure 5.7. Calculated shell temperature after sunlight irradiation while immersed in water.

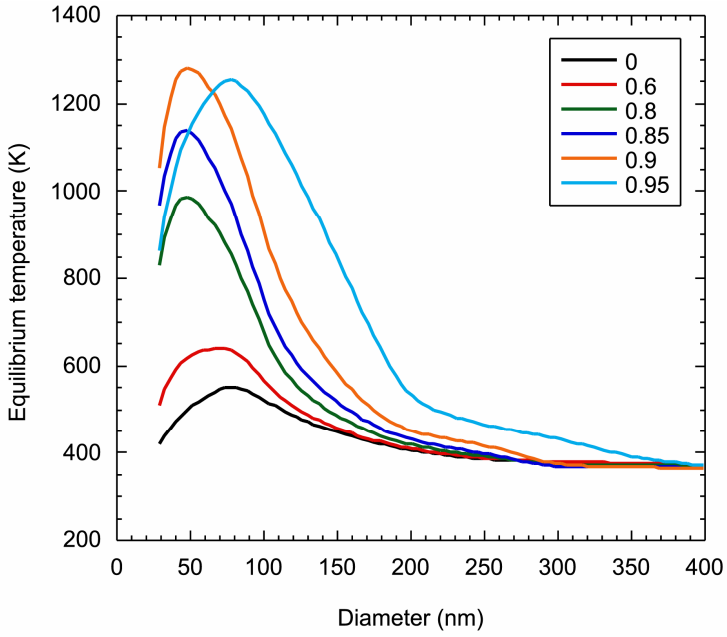

Figure 5.8. Calculated shell temperature after laser irradiation while immersed in water.

As expected, the optimum geometries for maximum equilibrium temperature again follow directly from the trends found for Q_{abs} and heat flux. Under sunlight irradiation there is negligible temperature change, the maximum equilibrium temperature reaching only 293.74 K for the 80 nm diameter, 0.8 aspect ratio shell. By comparison, when irradiated by the laser the 50 nm diameter, 0.9 aspect ratio shell reached an equilibrium temperature of 1323 K when suspended in water. This temperature is extremely high and in practice, under these conditions, melting of the gold and fragmentation of the shell is likely as has been demonstrated in previous experimental studies.[53, 57, 202] Nevertheless it is possible to optimise the radiation parameters to prevent this situation by limiting the laser intensity and/or the irradiation period.

Recently Pitsillides *et al.*[53] used a solution to the heat conduction equation to theoretically calculate the temperature change of a gold nanoparticle within a surrounding fluid after irradiation by a 532 nm laser pulse at a fluence of 0.5 J/cm^2. To do this they assumed the nanoparticle was a homogeneous sphere embedded in an infinite homogeneous medium (surrounding fluid). A temperature change of around 2500 K was calculated for a 30 nm gold particle (Q_{abs} = 2) after irradiation for 20 ns. Within this model conduction as

opposed to convection was used as the method of heat transfer. However, the thermal conductivity of fluids is quite poor and convection is a far more efficient method of cooling, as heat is taken from one location to another resulting from the bulk fluid motion as opposed to heat transfer between adjacent electron or phonon interactions during conduction.[195] As such it is believed that the calculated temperature change of 2500 K is actually greater than physically realisable.

It is clear that the different shell geometries are not the same when it comes to generating localised heat fluxes. It has been shown that the optimum shell geometry under conditions of laser irradiation has a diameter of 50 nm and an aspect ratio of 0.9. This shape provides the highest possible heat flux, and would therefore suggest that it is the most appropriate shape for applications that require plasmonic heating. In water this particular shell has a maximum plasmon absorption at 846 nm, which is positioned within the 'infrared window' of human tissue. If the dielectric core were made of polystyrene or silica, as opposed to water, it would have had the effect of red-shifting the peak position and decreasing Q_{abs}.

5.3. Conclusions

A classical physics approach was adopted to demonstrate that a shell could be engineered to achieve an optimum temperature by varying the geometry of the shell. Irradiation of the shell was simulated by two methods, firstly by 800 Wm^{-2} of sunlight and secondly by a 10 mW, 0.5 mm diameter spot size laser. The absorption efficiency of the shells and hence the surface heat flux was calculated from an implementation of Mie theory. Equilibrium temperatures for irradiated shells suspended in water were calculated using a convective heat transfer model.

It was found that for shells irradiated by sunlight, relatively thick shells with a diameter in the range of 80 nm to 100 nm gave the optimum surface heat flux. Despite the shift in wavelength of the absorption maximum the use of thick shells compared with solid spheres has only a small effect upon the surface heat flux and 80 nm diameter, 0.8 aspect ratio shells produced a maximum surface heat flux of approximately 175 Wm^{-2}. By

comparison 110 nm solid spheres produced a maximum surface heat flux of around 150 Wm^{-2}. When these shells were suspended in water the corresponding equilibrium temperature was essentially the same as the surrounding medium, that is, there was virtually no temperature rise. The relative insensitivity to the use of shells or solid spheres arises from the broad spectrum of the irradiating sunlight.

On the other hand, shells offered dramatic advantages over solid spheres when illuminated by a laser source where the laser wavelength could be tuned to the absorption maximum. The calculated maximum surface heat flux was produced by the 50 nm diameter, 0.9 aspect ratio shells. For an incident intensity of 10 mW over a 0.5 mm spot size the value is approximately 245 kWm^{-2} whereas solid spheres produced a maximum of only about 50 kWm^{-2}. For isolated shells suspended in water the calculated optimum equilibrium temperature was 1323 K. Realising these substantial temperature changes in a real experiment would, however, rely upon availability of the appropriate laser source and for the 50 nm diameter, 0.9 aspect ratio shells the calculated absorption maximum occurs at a wavelength of about 846 nm.

Chapter 6

6. Tuneable plasmon absorption in gold nanoparticles: shells versus rods

In the previous chapter it was shown that shells produce impressive absorption efficiencies at a plasmon resonance wavelength that can be tuned from the visible to the infrared part of the spectrum by varying the aspect ratio of the shell. Rods also have this ability and recently the relative merits of rods and shells as absorbers and scatterers of light for medical and biological applications have been analysed by Jain *et al*.[203] They concluded that gold rods were an order of magnitude more effective than shells in terms of absorption and extinction when compared on the basis of overall particle volume. However, the high value of gold implies that a more relevant figure-of-merit will be based on the amount of gold contained per particle, which in the case of shells with their dielectric cores, is a rather different measure.

In this chapter the absorption cross-sections of rods and shells, with a constant volume of gold, are compared directly. Mie theory and DDA techniques are used to calculate the optical efficiencies of geometrically varying shells and rods, respectively. The aim is to make a direct comparison between their absorption efficiencies and thereby decide which nanoparticle is better suited to applications such as thermal therapeutic techniques and energy efficient window coatings.[iii]

[iii] The work presented in this chapter has been published as a paper entitled, "Nanoparticles: The case for gold rods and shells" by N. Harris, M.J. Ford, P. Mulvaney and M.B. Cortie, in Gold Bulletin, 2008, **41**, 5

Clearly, other symmetries of particle will have plasmon resonances at different wavelengths and can provide methods for tuning the absorption spectrum. However, here only shells and rods are considered as they provide a systematic method for tuning the optical response, that is, by changing the aspect ratio. In addition, shells and rods have been synthesised by a number of groups.

6.1. Methods

For all calculations the bulk dielectric function of gold was used[179] and damping of the plasmon resonance from surface scattering was not considered. Surface scattering effects are smaller for the longitudinal mode of the rods[204] compared to the transverse mode of the rods and the resonance for shells, where the extinction peak will broaden significantly.

6.1.1. Shells

BHCOAT,[13] as described in Chapters 2 and 5, was used to calculate the extinction efficiency of geometrically varying shells. To enable a mass-weighted absorption comparison between rods and shells the volume of gold used to model each particle was kept constant at 55,550 nm^3. This is the same amount of gold contained in a solid spherical particle of 23.7 nm radius. This value was chosen to ensure that the optimum shell geometries calculated in the previous chapter were included here. The shell geometries to be modelled were produced by taking the solid spherical particle and then increasing the inner core radius a of the shell in 1 nm steps until a final shell with a radius b of 51.71 nm, shell thickness of 1.71 nm and a 0.97 aspect ratio was modelled. All shells were modelled with a core composed of water.

6.1.2. Rods

The extinction efficiencies of hemispherically capped rods were calculated using the DDA[164-167] technique described in Chapter 2 and implemented in the DDSCAT code of

Draine and Flateau.[157] All of the calculations presented here were conducted under computational conditions which exceed those recommended by the DDSCAT authors[157] to give reasonably converged answers. For solid spheres and shells the agreement between DDSCAT calculations using the present computational conditions and the exact Mie theory is excellent.

A 100 x 100 x 100 finite grid point array was used to render the volume of the rod. The length and diameter of the hemispherically-capped rod was used to determine the number of grid points that were "turned on" to represent the rod volume and the number of dipoles used to represent the rod was adjusted to keep the inter-dipole spacing constant at around 1 nm. This ensured that there were sufficient dipoles to accurately represent the rod geometry. However, it meant that for some rod geometries the volume varied from the constant volume of 55,550 nm^3, with the most extreme case having a tolerance of $55{,}550 \pm 875$ nm^3 for the l = 74 nm, d = 33 nm rod.

Calculations were performed on a number of rod geometries with aspect ratios ranging from 1.6 (l = 61 nm, d = 38 nm) to 4.7 (l = 118 nm, d = 25 nm). Computational time limitations prevented the calculation of extinction efficiencies for rods with larger aspect ratios.

The incident light was polarised such that the electric field was parallel to either the longitudinal or transverse axis of the rod, which will be referred to as longitudinal and transverse polarisations, respectively.

Usually optical absorption and scattering values are compared in terms of the extinction cross-section, C_{ext} normalised to the geometric cross-section of the particles and is referred to as the extinction efficiency, Q_{ext}. This is a convenient method for spherical particles as it provides an effective absorption per unit cross-sectional area against which different sized particles can be compared directly. However, for non-spherical particles there is no obvious way of defining the geometric cross-section. The most common convention, at least with computational codes, is to reduce the mass of the particle to an equivalent sphere and use the cross-sectional area of this sphere. This makes sense where the extinction efficiencies are orientationally averaged, but can hide many of the interesting shape dependent effects. Therefore, in this work the absolute absorption and scattering

cross-section values are calculated and then normalised to the true cross-section of the particle, that is, the cross-sectional area the particle presents to light incident from that direction.

6.2. Results

6.2.1. Shells

Figure 6.1 shows the variation in peak absorption efficiency, Q_{abs} as a function of b.

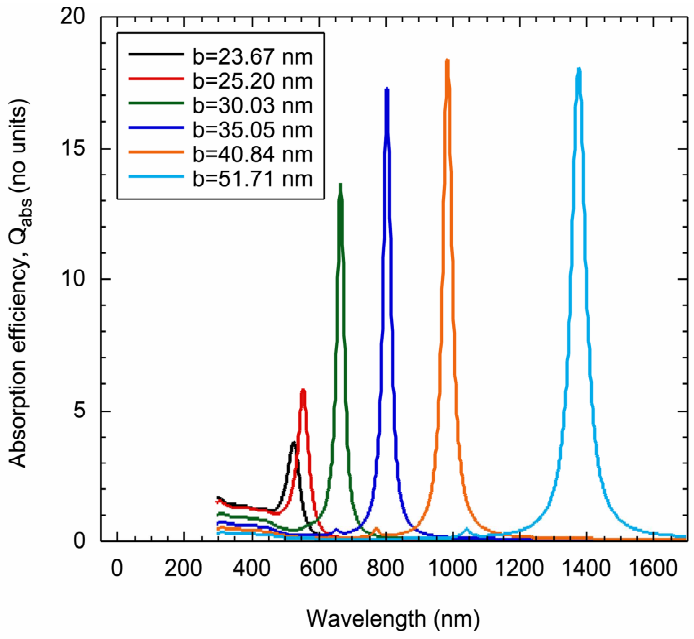

Figure 6.1. Shell absorption efficiencies for increasing aspect ratios. Note that in this figure any peak heights for a shell of b >32nm are likely to be considerably overestimated due to damping of the plasmon resonance in very thin shells.

As b increases the shell becomes thinner and the aspect ratio increases. This causes the peak Q_{abs} to red-shift from the visible spectra into the infrared. This is exactly the same phenomenon that was described in figure 5.4, resulting from the hybridisation of the plasmon modes at the shell-dielectric interfaces. For shell thicknesses between 1.7 nm and

4.8 nm Q_{abs} varies between around 16 and 18. However, the bulk dielectric data used becomes increasingly inappropriate as the shell thickness decreases and plasmon damping will become apparent forcing a broadening and consequent reduction of the absorption peak. This means that shells with thicknesses below approximately 5 nm[14] would have a reduced Q_{abs} and consequently an optimum Q_{abs} somewhere between 14 and 16 would be produced by shells with radii between 30 to 32 nm and shell thicknesses of 5.1 nm to 6.0 nm.

Figure 6.2 shows Q_{abs} and absorption cross-section, C_{abs} at the maximum of the plasmon peak plotted against shell radius, b.

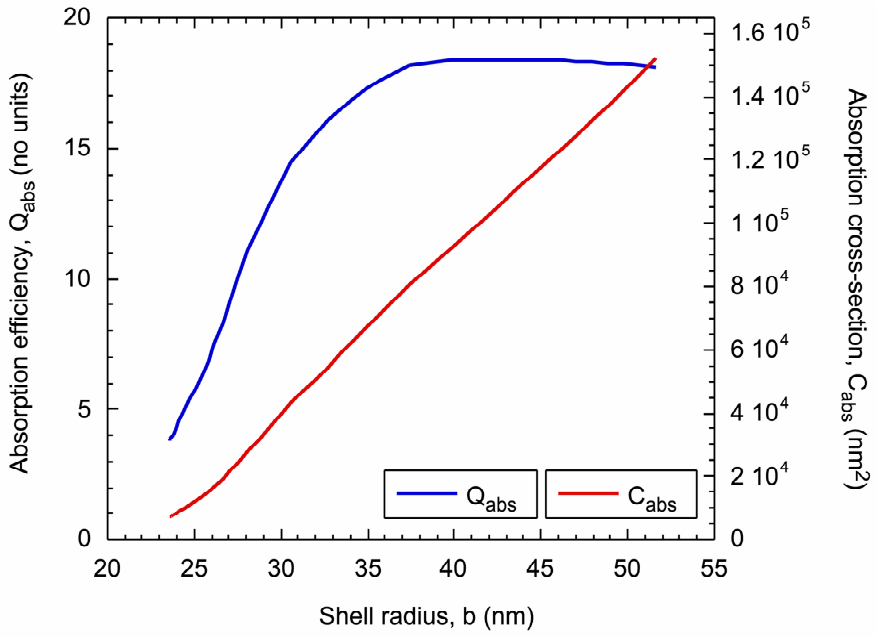

Figure 6.2. Absorption efficiency and cross-section as a function of shell radius calculated using BHCOAT. Shells were modelled as a gold shell with a water core with dimensions ranging from a = 0 nm, b = 23.67 nm to a = 50 nm, b = 51.71 nm.

As the volume was kept approximately constant the shell thickness decreases as the diameter increases. An optimum Q_{abs} of around 18 at a wavelength of 1078 nm is produced by the shell with a = 41 nm and b = 43.5 nm. Beyond this diameter Q_{abs} decreases as the shell becomes thinner reducing the amount of metal available to absorb the incident light.

In Chapter 2 it was shown that the polarisability of a shell in the electrostatic limit could be described by equation 6.1 and it can be seen that the shell polarisability increases with b^3.

$$\alpha = 4\pi b^3 \frac{(\varepsilon_2 - \varepsilon_m)(\varepsilon_1 + 2\varepsilon_2) + f(\varepsilon_1 - \varepsilon_2)(\varepsilon_m + 2\varepsilon_2)}{(\varepsilon_2 + 2\varepsilon_m)(\varepsilon_1 + 2\varepsilon_2) + f(2\varepsilon_2 - 2\varepsilon_m)(\varepsilon_1 - \varepsilon_2)} \quad 6.1$$

The extinction efficiency of the shell in the electrostatic limit can be calculated using equation 6.2

$$C_{ext} = k\,\mathrm{Im}(\alpha) \quad 6.2$$

and since scattering is small compared with absorption in the electrostatic limit equation 6.2 can be re-written as[13]

$$C_{abs} = k\,\mathrm{Im}(\alpha) \quad 6.3$$

Consequently as b increases, so does C_{abs}. This is evident from figure 6.2 with the solid sphere, with b = 23.7 nm producing a C_{abs} of 6534 nm^2 and the 0.97 aspect ratio shell, with b = 51.7 nm producing a C_{abs} of 151543 nm^2.

Figure 6.3 shows scattering efficiency, Q_{sca} and scattering cross-section, C_{sca} at the maximum of the plasmon absorption peak plotted against shell radius b. The amount of incident light scattered by the shells is less than the amount they absorb, at the maximum of the plasmon absorption. For example the solid sphere produces a Q_{abs} of 3.7 and a Q_{sca} of 0.3, whereas the optimum shell with a = 41 nm and b = 43.5 nm, neglecting damping, produces a Q_{abs} of around 18 at a wavelength of 1078 nm and a Q_{sca}, which is around three times less of 6.7 at the same wavelength.

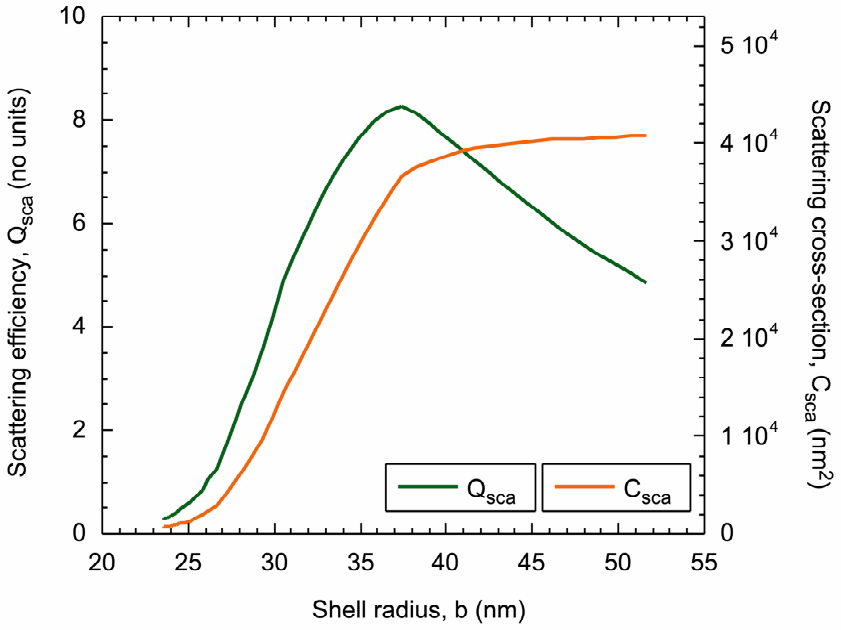

Figure 6.3. Scattering efficiency and cross-section as a function of shell radius calculated using BHCOAT.

There is a point reached where C_{sca} becomes relatively constant, which can be seen to occur for shell radii b beyond around 40 nm. At this point Q_{sca} starts to reduce as it is normalised to the increasing cross-sectional area. Scattering across the entire wavelength spectrum, however, will increase as the particle size increases. At particle radii of around 50 nm the overall scattering will begin to dominate absorption.

6.2.2. Rods

Figure 6.4 shows the variation in the maximum longitudinal plasmon response, Q_{abs} as a function of rod aspect ratio and it can be seen that Q_{abs} red-shifts with increasing aspect ratio, as predicted by Gans.[24] For example the 1.6 aspect ratio rod (l = 61 nm, d = 38 nm) produces a peak Q_{abs} of around 9 at 583 nm. Whereas the 4.2 aspect ratio rod (l = 110 nm, d = 26 nm) produces a peak Q_{abs} of around 32 at 887 nm.

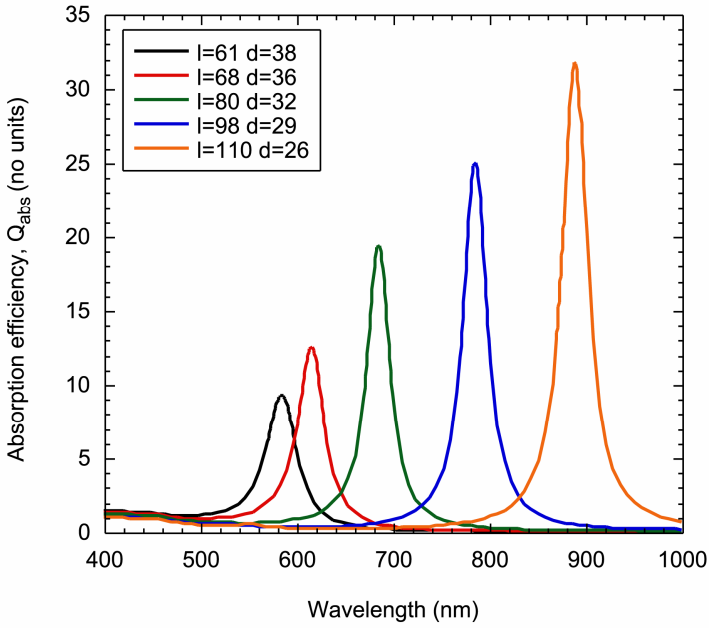

Figure 6.4. Longitudinal absorption efficiencies for a rod with an increasing aspect ratio.

In addition to the longitudinal Q_{abs} the transverse Q_{abs} was calculated for each rod, with the magnitude of Q_{abs} for the transverse response of the rods constituting the lesser of the two plasmon responses. Moreover, the position of the transverse Q_{abs} peak blue shifts with increasing aspect ratio with the smallest rod, l = 61 nm, d = 38 nm producing a transverse Q_{abs} of 3.8 at 519 nm and the largest rod, l = 118 nm, d = 25 nm producing a Q_{abs} of 5.6 at 512 nm. The transverse absorption is very similar to a spherical particle of the same diameter

The calculated Q_{abs} and C_{abs} results for varying aspect ratio rods are shown in figure 6.5 for a maximum plasmon absorption and figure 6.6 shows the calculated scattering efficiency, Q_{sca} and scattering cross-section, C_{sca} for the same geometry rods. All of these results are produced from the longitudinal polarisation of each rod.

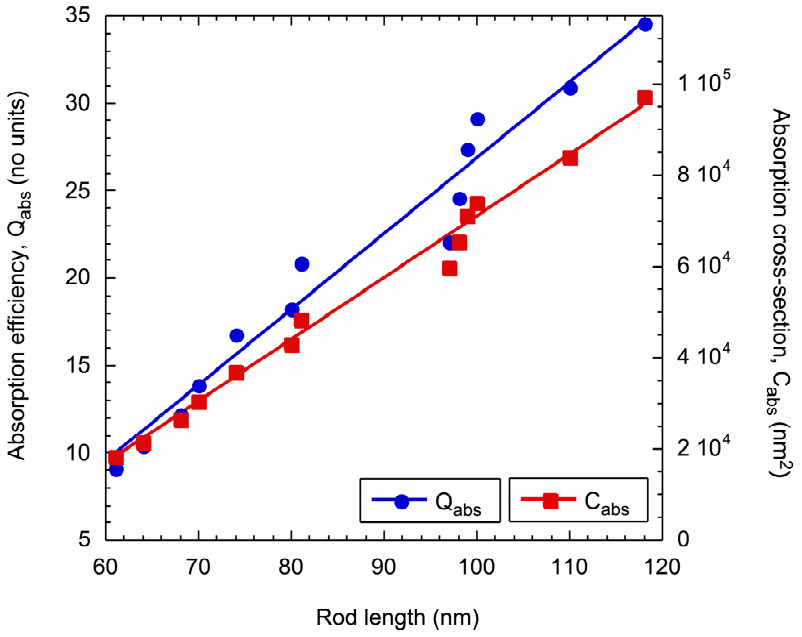

Figure 6.5. Absorption efficiency and cross-section as a function of rod length calculated using DDSCAT. Rods were modelled as gold hemispherically capped rods in water with dimensions ranging from l = 61 nm, d = 38 nm to l = 118 nm, d = 25 nm.

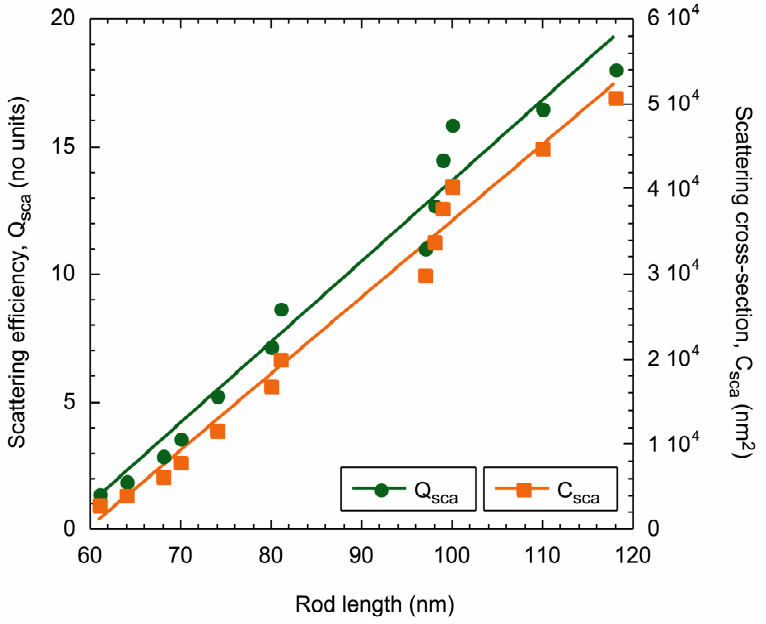

Figure 6.6. Scattering efficiency and cross-section as a function of rod length calculated using DDSCAT.

The data points within these figures are not in a straight line as the rod geometries were rendered to a three-dimensional finite grid array, where in some cases a small change in the rod geometry resulted in an abrupt grid change. Therefore a line of best fit has been used to fit the data points within each figure.

The polarisability of the rod/ellipse in the electrostatic limit was described in Chapter 2 by equation 6.4 and it can be seen that the rod polarisability increases with rod aspect ratio.

$$\alpha_x = 4\pi abc \frac{\varepsilon_1 - \varepsilon_m}{3\varepsilon_m + 3L_1(\varepsilon_1 - \varepsilon_m)} \qquad 6.4$$

In the electrostatic limit scattering is small compared with absorption and, as was the case for the shells, equation 6.2 can be re-written as

$$C_{abs} = k\,\mathrm{Im}(\alpha) \qquad 6.5$$

Consequently as the rod aspect ratio increases, so does C_{abs}, which is evident from figure 6.5 with the smallest rod (l = 61 nm, d = 38 nm) producing a C_{abs} of around 18345 nm^2 and a Q_{abs} of 9.1 at 583 nm. The longest rod (l = 118 nm, d = 25 nm) produces a C_{abs} of around 97127 nm^2 and a Q_{abs} of 34.5 at 951 nm. However, equation 6.4 is only valid in within the electrostatic limit. Therefore as the length of the rod increases there will come a point where Q_{abs} and C_{abs} will reach an optimum value and then start to decrease because the electrostatic regime is no longer valid, as the rod becomes very long compared with the incident wavelength, and the intensity of the longitudinal plasmon absorption will begin to decrease and approach zero.[13] Unfortunately an optimum geometry for maximum absorption efficiency was not calculated as the computational time required to calculate absorption efficiencies of larger aspect ratio rods was a hindrance.

It can be seen from figure 6.6 that Q_{sca} and C_{sca} also increase as the length of the rod increases. However, the rods still scatter considerably less than they absorb, at the peak of the plasmon resonance, making them attractive for thermal applications. For example the longest rod (l = 118 nm, d = 25 nm) produces a maximum Q_{abs} of 34.5 and Q_{sca} of

around 18. For the same rod the absorption cross section, C_{abs} is around 97127 nm^2 and it scatters around half the amount of incident light it absorbs, that is, C_{sca} is around 50741 nm^2.

6.3. Discussion

Rods out perform shells by producing larger overall absorption efficiencies and larger absorption efficiencies per unit area for a constant volume of gold. For example, the optimum Q_{abs} produced by the 43.5 nm radius shell with a shell thickness of 2.5 nm was around 18 whereas a maximum Q_{abs} of 34.5 was produced by a rod with a length of 118 nm and a diameter of 25 nm. Furthermore, the longitudinal response of the rod is unlikely to be affected by surface scattering, which will become apparent in a 2.5 nm thick shell, meaning that this optimum shell Q_{abs} value is likely to be overestimated.

The cross-sectional area of the optimum shell ($Q_{abs} \approx 18$) was around 5939 nm^2, and around 2816 nm^2 for the largest rod ($Q_{abs} \approx 34.5$). When compared against the shell the rod produces around twice the Q_{abs} with half the cross-sectional area. Because a constant volume has been maintained in the particles, and because the rods are twice as efficient as the shells, half the number of rods, and hence half the amount of gold, would be required to produce the same absorption per unit area compared with shells, on the surface of, for example a window coating. This assumes, of course, that the rods or shells are distributed over the surface such that the inter-particle spacing is large enough to ensure that there are no near-field resonance interactions. In addition, because the rods have half the cross-sectional area they can be packed more densely on a surface when compared with shells and hence achieve greater total absorption at the expense of more gold per unit area.

Moreover, while it is now possible to produce shells with thicknesses of around 4.5 nm,[86] the seed-mediated synthesis techniques used to produce rods are well established and capable of producing any aspect ratio rod, limited only by the seed nature and size and the nature of surfactant.

6.4. Conclusions

It has been shown that for a fixed volume of gold the absorption efficiency produced by rods out performs the absorption efficiency produced by shells. Shell efficiencies and cross-sections were calculated using an implementation of Mie theory while rod efficiencies and cross-sections were calculated using a DDA technique.

The optimum shell with a = 41 nm and b = 43.48 nm produced a maximum Q_{abs} of around 18 and C_{abs} of 108837 nm^2 at 1078 nm. While the longest rod, with l = 118 nm, d = 25 nm produced a maximum Q_{abs} of around 34.5 and C_{abs} of 97127 nm^2 at 950 nm. The C_{abs} produced by the optimum shell exceeds that produced by the largest rod. However, since Q_{abs} is C_{abs} normalised to the nanoparticle cross-sectional area the largest rod, with a smaller cross-section than the optimum shell, produces a greater Q_{abs} than the shell.

Despite the inability to do a direct comparison between the optical responses for the optimum shell and the optimum rod due to computational time limitations using the DDA method, the results presented here demonstrate the optical response of the rods still out performs that of the shells.

The volume of the gold within the nanoparticles was kept constant therefore the largest rod produced twice the Q_{abs} compared to the optimum shell. As such halve the number of rods and therefore half the volume of gold would be required to produce the same absorption per unit area.

Despite the establishment of new synthesis techniques capable of producing uniform sized shells with smaller shell thicknesses the wet chemistry synthesis techniques used to make rods are well established with meticulous control over rod aspect ratio achieved through the selection of an appropriate seed and surfactant. Based on the synthesis techniques described in section 1.2.4 it is possible to synthesise the rods modelled within this chapter, whereas the synthesis of the optimum geometry shell with a shell thickness of around 2.5 nm, at this point in time, may prove to be more difficult.

Chapter 7

7. Conclusions and future directions

One of the aims within this thesis was to develop a new technique to synthesise three-dimensional gold nanoparticle colloidal crystals. This was achieved by irradiating a glass substrate immersed in a gold nanoparticle in MMA colloid with a 514 nm laser at 480 mW for two minutes. Control over deposition location was possible through the translation of the glass substrate using an X-Y stage. This technique is advantageous compared to other techniques currently employed to synthesise colloidal crystals because templates or pre-functionalised substrates are not required. Through the use of control experiments and calculations it was hypothesised that localised-plasmonic heating of the gold nanoparticles within the supraspheres aids in the rapid formation of the colloidal crystals. To provide further evidence to support this hypothesis, 9 nm diameter silver nanoparticles should be synthesised using the method of Hiramatsu and Osterloh.[18] These particles have a plasmon resonance of around 400 nm and thus allow the plasmon resonance to be tuned away from the laser wavelength. Alternatively, the use of different sizes, for example 50 to 100 nm diameters, or shapes, for example nanoshells or nanorods, will allow one to red-shift the plasmon resonance away from the d-band transitions of gold to the point where a diode laser with a wavelength of 808 nm could be used.

Future experimental work will include a more vigorous analysis of the optical properties of the colloidal crystals. Dark field microscopy analysis was attempted with the help of Professor Paul Mulvaney from the University of Melbourne, however it transpired that the colloidal crystals scattered significantly and only very bright white light or yellow scattered light was evident with no reproducible spectra. The next step forward is to use a

spectrophotometer with a micron-sized spot size as well as SAXS and spectroscopic ellipsometry, providing synthesis of colloidal crystals with 100 micron domains is possible. It is assumed that the starting size of the supraspheres influences the size of the colloidal crystal with the number of nanoparticles per suprasphere proportional to the ratio of the concentration of nanoparticles in solution and the number of nucleation sites.[205] Therefore the ability to tailor the size of the supraspheres is important to enable control over the colloidal crystal dimensions and consequently understanding of and control over the aggregation mechanism is essential. Furthermore, investigation of both the possible effect of laser trapping of the supraspheres in the formation of the crescent shaped structures on the glass substrate and possible tailoring of the colloidal crystal formation mechanism in order to enhance or prevent formation needs to be undertaken.

The second aim of this thesis was to model the optical response of three-dimensional gold nanoparticle colloidal crystals. This was investigated using two different approaches. The first approach was to examine the effect of particle order and disorder, within the three-dimensional structures, on the extinction spectra using the T-matrix technique. This was achieved by comparing the extinction spectra of a 100 particle spherically-shaped colloidal crystal and the same structure after it had been disordered using GULP. An additional extinction peak was evident in the spherically-shaped colloidal crystal, however it was not present in its disordered counterpart. Further investigation of ordered and disordered single FCC structures concluded that disordering the particles within the structure had the effect of producing inter-particle spacings that were no longer well-defined when compared to the finite number of well-defined spacings present within the ordered structure. This reduced the effect of hybridisation of the individual particle plasmon modes and prevented the production of an additional extinction peak in the disordered structure.

The second approach devised to investigate the optical response of three-dimensional colloidal crystals was to examine a long, one-dimensional chain of gold particles with varying inter-particle spacings. This approach used the T-matrix technique to calculate the extinction spectra produced by the chain and subsequently uncover the physics associated with near-field interactions in large ordered arrays. Decreasing the inter-particle spacing for a fixed length chain caused the extinction peak to split into two separate peaks. The first peak was blue-shifted with transverse polarisation and the second peak was red-shifted with

longitudinal polarisation. Interestingly, the longitudinal peak-shift did not follow an exponential dependence as reported earlier by other groups. Rather the extent of the peak-shift is more accurately described by the inverse inter-particle or distance power law dependence, as per Van der Waals interactions between two spheres. This dependence is applicable for all chain lengths and inter-particle spacings in the near-field regime. Increasing the length of the chain for a constant inter-particle gap caused the longitudinal extinction peak to red-shift to an asymptote, the value of which depended upon the inter-particle spacing. In this case the peak-shift did follow an exponential dependence and the asymptotic value was achieved by approximately ten particles with a characteristic interaction length of two particles. It was then possible to combine both the inverse distance and exponential dependence laws into a universal equation, which predicts the extinction peak-shift, from an isolated sphere, for chains of any length and inter-particle spacings in the near-field regime. This law is applicable to particle sizes below 100 nm.

These calculations were extended to the far-field regime through the investigation of a chain of silver dimers with the aim of calculating the optical response of a structure that could enhance both the incident and Stokes shifted wavelengths. For dimers that were aligned perpendicular to the chain axis with transverse polarisation, far-field diffractive effects dominated the extinction spectra. Conversely, for longitudinal polarisation, near-field dimer effects dominated the extinction spectra. Polarisation at 45^{o} enabled both the diffractive and dimer extinction peaks to be present at the same time.

The potential to use nanoshells and nanorods in the synthesis of colloidal crystals has promise as both of these geometries have the ability to exploit the localised-plasmonic heating effect far more efficiently than nanospheres due to their larger absorption cross-sections. Therefore, the nanoshell geometry that was capable of producing an optimum equilibrium temperature under sunlight and laser irradiation was determined. A formulation of Mie theory was used to calculate the absorption efficiency for geometrically varying gold nanoshells. Surface heat flux was calculated after irradiation was simulated by 800 Wm^{-2} of sunlight and by a $10\ \mathrm{mW}$, 0.5 mm diameter spot size laser. A convective heat transfer model was then used to calculate the equilibrium temperature of an isolated nanoshell suspended in water. A calculated maximum surface heat flux of approximately

175 Wm^{-2} was produced by the 80 nm diameter, 0.8 aspect ratio nanoshell. This amount of surface heat flux resulted in virtually no temperature rise in the nanoshell. By comparison, upon laser irradiation, the 50 nm diameter, 0.9 aspect ratio nanoshell produced a maximum surface heat flux of approximately 245 kWm^{-2}.For isolated shells suspended in water this produced an optimum equilibrium temperature of 1323 K.

A direct comparison between the calculated absorption efficiencies of nanoshells and nanorods for a fixed volume of gold was then performed. A formulation of Mie theory and the DDA technique were used to calculate the absorption efficiencies of the nanoshells and nanorods, respectively. The optimum nanoshell, with a diameter of 43.48 nm and an aspect ratio of 0.9 produced a maximum absorption efficiency of approximately 18. By comparison, the longest nanorod with a length of 118 nm and an aspect ratio of 4.7 produced a maximum absorption efficiency of 34.5. Therefore, the optical response of nanorods is almost twice as good as nanoshells with the same volume of gold. Moreover, wet chemistry techniques that have been developed to synthesise nanorods have been improved over time to the point where meticulous control over aspect ratio and yield are possible. Whereas, synthesis of the optimum geometry nanoshells with shell thicknesses less than or equal to 5 nm may be problematic.

Appendices

Appendix A: Publication Report

A.1 Peer reviewed journal articles

- "Plasmonic resonances of closely-coupled gold nanosphere chains", N. Harris, M.D. Arnold, M.G. Blaber and M.J. Ford, *Journal of Physical Chemistry C* **113** 2784 (2009)
- "Mie and Bragg plasmons in sub-wavelength silver semi-shells", A.I. Maaroof, M.B. Cortie, N. Harris and L. Wieczorek, *Small* **4** 2292 (2008)
- "Tunable infrared absorption by metal nanoparticles: the case for gold rods and shells", N. Harris, M.J. Ford, P. Mulvaney and M.B. Cortie, *Gold Bulletin* **1** 5 (2008)
- "Laser-induced assembly of gold nanoparticles into colloidal crystals", N. Harris, M.J Ford, M.B. Cortie and A.M. McDonagh, *Nanotechnology* **18** 365301 (2007).
- "Optical properties of suspension of gold half-shells", J. Liu, K.E. McBean, N. Harris and M.B. Cortie, *Materials Science and Engineering B* **140** 195 (2007).
- "Core-shell nanoparticles with self-regulating plasmonic functionality", M.B. Cortie, A. Dowd, N. Harris and M.J. Ford, *Physical Review B* **75** 113405 (2007).
- "Optimization of plasmonic heating by gold nanospheres and nanoshells", N. Harris, M.J. Ford and M.B Cortie, *Journal of Physical Chemistry B* **22**, 10701 (2006).

A.2 Peer reviewed full conference papers

- "Plasmon absorption in nanospheres: A comparison of sodium, potassium, aluminium, silver and gold", M.G. Blaber, M.D. Arnold, N. Harris, M.J. Ford and M.B. Cortie, *Physica B: Condensed Matter* **2** 184 (2007).
- "Plasmonic heating and its possible exploitation in nanolithography", M.B. Cortie, N. Harris and M.J. Ford, *Physica B: Condensed Matter* **2** 188 (2007).
- "Optimisation of absorption efficiency for varying dielectric spherical nanoparticles", M.G. Blaber, N. Harris, M.J. Ford and M.B. Cortie, in *Proceedings of the International Conference on Nanoscience and Nanotechnology (ICONN 2006)* edited by C. Jagadish and G.Q.M. Lu, p. 556 (Brisbane, 2006 IEEE)

A.3 Oral presentations

- "Synthesis and optical properties of 3-D gold nanoparticle colloidal crystals", N. Harris, M.J. Ford and M.B. Cortie, International Conference on Nanoscience and Nanotechnology (ICONN), February 2008, Melbourne, Australia.
- "Laser-induced synthesis of gold nanoparticle colloidal crystals", N. Harris, M.J. Ford, M.B. Cortie and A.M. McDonagh, International Conference on Materials for Advanced Technologies (ICMAT), July 2007, Singapore.
- "Optimised plasmonic heating in gold nanoparticles", N. Harris, M.J. Ford and M.B. Cortie, International Conference on Nanoscience and Nanotechnology (ICONN), July 2006, Brisbane, Australia.

A.4 Poster presentations

- "Localised heating effects in gold nanoparticles", N. Harris, M. J. Ford and M. B. Cortie, 30th Annual Condensed Matter and Materials Meeting, February 2006, Wagga Wagga, Australia.

Bibliography:

1. Tarhan, I. I.; Watson, G. H. *Phys. Rev. Lett* **1996,** *76*, 315.
2. Yablonovitch, E. *Phys. Rev. Lett* **1987,** *58*, 2059.
3. Yablonovitch, E. *J. Phys. Condens. Matter* **1993,** *5*, 2443.
4. Zhang, X.; Sun, B.; Friend, R. H. *Nano Lett.* **2006,** *6*, 651.
5. Brolo, A. G.; Arctander, E.; Gordon, R.; Leathem, B.; Kavanagh, K. L. *Nano Lett.* **2004,** *4*, 2015.
6. Dick, L. A.; McFarland, A. D.; Haynes, C. L.; Duyne, R. P. V. *J. Phys. Chem. B* **2002,** *106*, 853.
7. Griffith, F. R.; Grabar, K. C.; Allison, K. J.; Bright, R. B.; Davis, J. A.; Guthrie, A. P.; Hommer, M. B.; Jackson, M. A.; Smith, P. C.; Walter, D. G.; Natan, M. J. *Science* **1995,** *267*, 1629.
8. Kubo, S.; Gu, Z.-Z.; Tryk, D. A.; Ohko, Y.; Sato, O.; Fujishima, A. *Langmuir* **2002,** *18*, 5043.
9. Lu, L.; Randjelovic, I.; Capek, R.; Gaponik, N.; Yang, J.; Zhang, H.; Eychmuller, A. *Chem. Mater* **2005,** *17*, 5731.
10. Nie, S.; Emroy, S. R. *Science* **1997,** *275*, 1102.
11. Tessier, P. M.; Velec, O. D.; Kalambur, A. T.; Rabolt, J. F.; Lenhoff, A. M.; Kaler, E. M. *J. Am. Chem. Soc.* **2000,** *122*, 9554.
12. Bohren, C. F. *Am. J. Phys.* **1982,** *51*, 323.

13. Bohren, C. F.; Huffman, D. R., *Absorption and scattering of light by small particles*. Wiley: Weinheim, 2004.

14. Kreibig, U.; Vollmer, M., *Optical properties of metal clusters*. Springer-Verlag: Berlin Heidelberg, 1995.

15. Wagner, F. E.; Haslbeck, S.; Stievnao, L.; Calogero, S.; Pankhurst, Q. A.; Martinek, K.-P. *Nature* **2000,** *407*, 691.

16. Liz-Marzan, L. *Mater. Today* **2004,** *7*, 26.

17. Mulvaney, P. *Langmuir* **1996,** *12*, 788.

18. Hiramatsu, H.; Osterloh, F. E. *Chem. Mater* **2004,** *16*, 2509.

19. Link, S.; El-Sayed, M. *Int. Rev. Phys. Chem* **2000,** *19*, 409.

20. Blaber, M. G.; Harris, N.; Ford, M. J.; Cortie, M. B. International Conference on Nanoscience and Nanotechnology (ICONN), Brisbane, 2006; Jagadish, C.; Lu, G. Q. M., IEEE Explore: p 556.

21. Aden, A. L.; Kerker, M. *J. Appl. Phys.* **1951,** *22*, 1242.

22. Prodan, E.; Radloff, C.; Halas, N. J.; Nordlander, P. *Science* **2003,** *302*, 419.

23. Perez-Juste, J.; Pastoriza-Santos, I.; Liz-Marzan, L. M.; Mulvaney, P. *Coord. Chem. Rev.* **2005,** *249*, 1870.

24. Gans, G. *Ann. Phys.* **1912,** *342*, 881.

25. Schwartzberg, A. M.; Zhang, J. Z. *J. Phys. Chem. C* **2008,** *112*, 10323.

26. Shi, W.; Sahoo, Y.; Swihart, M. T.; Prasad, P. N. *Langmuir* **2005,** *21*, 1610 - 1617.

27. Oldenburg, S. J.; Averitt, R. D.; Westcott, S. L.; Halas, N. J. *Chem. Phys. Lett.* **1998,** *288*, 243.

28. Liang, H. P.; Wan, L. J.; Bai, C. L.; Jiang, L. *J. Phys. Chem. B* **2005,** *109*, 7795.

29. Pham, T.; Jackson, J. B.; Halas, N. J.; Lee, T. R. *Langmuir* **2002,** *18*, 4915.

30. Grzelczak, M.; Perez-Juste, J.; García de Abajo, F. J.; Liz-Marzan, L. M. *J. Phys. Chem. C* **2007,** *111*, 6183.

31. Jana, N. R.; Gearheart, L.; Murphy, C. J. *J. Phys. Chem. B* **2001,** *105*, 4065.

32. Pecharroman, C.; Perez-Juste, J.; Mata-Osoro, G.; Liz-Marzan, L.; Mulvaney, P. *Phys. Rev. B* **2008,** *77*, 035418.

33. Jiang, X. C.; Pileni, M. P. *Colloids Surf., A* **2007,** *295*, 228.

34. Hao, F.; Nehl, C. L.; Hafner, J. H.; Nordlander, P. *Nano Lett.* **2007,** *7*, 729.

35. Nehl, C. L.; Liao, H.; Hafner, J. H. *Nano Lett.* **2006,** *6*, 683.

36. Xie, J.; Lee, J. Y.; Wang, D. I. C. *Chem. Mater* **2007,** *19*, 2823.

37. Bozzini, B.; Fanigliulo, A.; Serra, M. *J. Cryst. Growth* **2001,** *231*, 589.

38. Seo, D.; Park, J. C.; Song, H. *J. Am. Chem. Soc* **2006,** *128*, 14863.

39. Li, C.; Shuford, K. L.; Park, Q.-H.; Cai, W.; Li, Y.; Lee, E. J.; Cho, S. O. *Angew. Chem. Int. Ed* **2007,** *46*, 3264.

40. Li, C.; Shuford, K. L.; Chen, M.; Lee, E. J.; Cho, S. O. *2* **2008**.

41. Pastoriza-Santos, I.; Sanchez-Iglesias, A.; García de Abajo, F. J.; Liz-Marzan, L. M. *Adv. Func. Mater*. **2007,** *17*, 1443.

42. Lu, Y.; Liu, G. L.; Kim, J.; Mejia, Y. X.; Lee, L. P. *Nano Lett.* **2005,** *5*, 119.

43. Shumaker-Parry, J. S.; Rochholz, H.; Kreiter, M. *Adv. Mater.* **2005,** *17*, 2131.

44. Li, K.; Clime, L.; Cui, B.; Veres, T. *Nanotechnology* **2008,** *19*, 145305.

45. Ross, B. M.; Lee, L. P. *Nanotechnology* **2008,** *19*, 275201.

46. Sun, Y.; Wiley, B.; Li, Z.-Y.; Xia, Y. *J. Am. Chem. Soc* **2004,** *126*, 9399.

47. Shankar, S. S.; Rai, A.; Ahmad, A.; Sastry, M. *Chem. Mater* **2005,** *17*, 566.

48. Rai, A.; Singh, A.; Ahmad, A.; Sastry, M. *Langmuir* **2006,** *22*, 736.

49. Boneberg, J.; Konig-Birk, J.; Munzer, H.-J.; Leiderer, P.; Shuford, K. L.; Schatz, G. C. *Appl. Phys. A* **2007,** *89*, 299.

50. Nova, C.; Funston, A. M.; Pastoriza-Santos, I.; Liz-Marzan, L.; Mulvaney, P. *J. Phys. Chem. C* **2008,** *112*, 3.

51. Wang, H.; Brandl, D. W.; Le, F.; Nordlander, P.; Halas, N. J. *Nano Lett.* **2006,** *6*, 827.

52. Wiley, B. J.; Chen, Y.; McLellan, J. M.; Xiong, Y.; Li, Z.-Y.; Ginger, D.; Xia, Y. *Nano Lett.* **2007,** *7*, 1032.

53. Pitsillides, C. M.; Joe, E. K.; Wei, X.; Anderson, R. R.; Lin, C. P. *Biophys. J.* **2003,** *84*, 4023.

54. Loo, C.; Lin, A.; Hirsch, L.; Lee, M.; Barton, J.; Halas, N. J.; West, J. L.; Drezek, R. *Technol. Cancer Res. & Treat.* **2004,** *3*, 33.

55. Hirsch, L. R.; Stafford, R. J.; Bankson, J. A.; Sershen, S. R.; Rivera, B.; Price, R. E.; Hazle, J. D.; Halas, N. J.; West, J. L. *Proc. Nat. Acad. Sci. U.S.A.* **2003,** *100*, 13549.

56. Pissuwan, D.; Valenzuela, S.; Cortie, M. B. *Trends in Biotechnol.* **2006,** *24*, 62.

57. Prasad, V.; Mikhailovsky, A.; Zasadzinski, J. A. *Langmuir* **2005,** *21*, 7528.

58. West, J. L.; Halas, N. J. *Curr. Opin. Biotechnol.* **2000,** *11*, 215.

59. Skirtach, A. G.; Dejugnat, C.; Braun, D.; Susha, A. S.; Rogach, A. L.; Parak, W. J.; Mohwald, H.; Sukhorukov, G. B. *Nano Lett.* **2005,** *5*, 1371.

60. Cortie, M.; Xu, X.; Chowdhury, H.; Zareie, H.; Smith, G. *Proc. SPIE* **2005**.

61. Rechberger, W.; Hohenau, A.; Leitner, A.; Krenn, J. R.; Lamprecht, B.; Aussenegg, F. R. *Opt. Commun.* **2003,** *220*, 137.

62. Romero, I.; Aizpurua, J.; Bryant, G. W.; García de Abajo, F. J. *Opt. Express* **2006,** *14*, 9988.

63. Zou, S.; Schatz, G. C. *Chem. Phys. Lett.* **2005,** *403*, 62.

64. Freestone, I.; Meeks, N.; Sax, M.; Higgitt, C. *Gold Bull.* **2007,** *40*, 270.

65. Kelly, K. L.; Coronado, E.; Zhao, L. L.; Schatz, G. C. *J. Phys. Chem. B* **2003,** *107*, 668.

66. Moores, A.; Goettmann, F. *New J. Chem.* **2006,** *30*, 1121.

67. Faraday, M. *Philos. Trans. R. Soc. London* **1857,** *147*, 145.

68. Mie, G. *Ann. Phys.* **1908,** *4*, 377.

69. Scaffardi, L. B.; Tocho, J. O. *Nanotechnology* **2006,** *17*, 1309.

70. Alvarez, M. M.; Khoury, J. T.; Schaaff, T. G.; Shafigullin, M. N.; Vezmar, I.; Whetten, R. L. *J. Phys. Chem. B* **1997,** *101*, 3706.

71. Kawabata, A.; Kubo, R. *J. Phys. Soc. Jpn.* **1966,** *21*, 1765.

72. Nova, C.; Funston, A. M.; Mulvaney, P. *Nat. Nanotechnol.* **2008**.

73. Turkevich, J.; Stevenson, P. C.; Hillier, J. *Discuss. Faraday Soc.* **1951,** *11*, 55.

74. Brust, M.; Brethell, D.; Schiffrin, D. J.; Kiely, C. J. *Adv. Mater.* **1995,** *7*, 795.

75. Housni, A.; Ahmed, M.; Liu, S. Y.; Narain, R. *J. Phys. Chem. C* **2008,** *112*, 12282.

76. Chen, Y. Y.; Wang, X. K. *Mater. Lett.* **2008,** *62*, 2215.

77. Prodan, E.; Nordlander, P. *J. Chem. Phys* **2004,** *120*, 5444.

78. Chen, M.; Gao, L. *Inorg. Chem.* **2006,** *45*, 5145.

79. Liu, Z. X.; Song, H. W.; Yu, L. X.; Yang, L. M. *Appl. Phys. Lett.* **2005,** *86*, 113109.

80. Sun, Y. G.; Wiley, B.; Li, Z. Y.; Xia, Y. N. *J. Am. Chem. Soc.* **2004,** *126*, 9399.

81. Zhou, H. S.; Honma, I.; Komiyana, H.; Haus, J. W. *Phys. Rev. B* **1994,** *50*, 12052.

82. Decher, G. *Science* **1997,** *277*, 1232.

83. Pastoriza-Santos, I.; Perez-Juste, J.; Carregal-Romero, S.; Herves, P.; Liz-Marzan, L. M. *Chem. Asian J.* **2006,** *1*, 730.

84. Shi, W.; Sahoo, Y.; Swihart, M. T.; Prasad, P. N. *Langmuir* **2005,** *21*, 1610.

85. Schwartzberg, A. M.; Olson, T. Y.; Talley, C. E.; Zhang, J. Z. *J. Phys. Chem. B.* **2006,** *110*, 19935.

86. Sun, Y.; Mayers, B. T.; Xia, Y. *Nano Lett.* **2002,** *2*, 481.

87. Ji, X.; Shao, R.; Elliot, A. M.; Stafford, R. J.; Esparza-Coss, E.; Bankson, J. A.; Liang, G.; Luo, Z.; Park, K.; Markert, J. T.; Li, C. *J. Phys. Chem. C* **2007,** *111*, 6245.

88. Pol, V. G.; Grisaru, H.; Gedanken, A. *Langmuir* **2005,** *21*, 3635.

89. Suzuki, D.; Kawaguchi, H. *Langmuir* **2005,** *21*, 12016.

90. Dahmen, C.; Plessen, G. v. *Aust. J. Chem* **2007,** *60*, 447.

91. Yu, Y.; Chang, S.; Lee, C.; Wang, C. R. C. *J. Phys. Chem. B* **1997,** *101*, 6661.

92. Cepak, V. M.; Martin, C. R. *J. Phys. Chem. B* **1998,** *102*, 9985.

93. Payne, E. K.; Shuford, K. L.; Park, S.; Schatz, G. C.; Mirkin, C. A. *J. Phys. Chem. B* **2006,** *110*, 2150.

94. Gao, J. X.; Bender, C. M.; Murphy, C. J. *Langmuir* **2003,** *19*, 9065.

95. Gole, A.; Murphy, C. J. *Chem. Mater.* **2004,** *16*, 3633.

96. Brioude, A.; Jiang, X. C.; Pileni, M. P. *J. Phys. Chem. B* **2005,** *109*, 13138.

97. Limmer, S. J.; Chou, T. P.; Cao, G. Z. *J. Phys. Chem. B* **2003,** *107*, 13313.

98. Martin, C. R. *Chem. Mater* **1996,** *8*, 1739.

99. Wu, H.; Huang, W.; Huang, M. H. *Cryst. Growth Des.* **2007,** *7*, 831.

100. Rodriguez-Fernandez, J.; Perez-Juste, J.; Mulvaney, P.; Liz-Marzan, L. *J. Phys. Chem. B* **2005,** *109*, 14257.

101. Tsung, C.; Kou, X.; Shi, Q.; Zhang, J.; Yeung, M. H.; Wang, J.; Stucky, G. D. *J. Am. Chem. Soc* **2006,** *128*, 5352.

102. Kou, X. S.; Zhang, S. Z.; Yang, Z.; Tsung, C.-K.; Stucky, G. D.; Sun, L. D.; Wang, J. F.; Yan, C. H. *J. Am. Chem. Soc* **2007,** *129*, 6402.

103. Ni, W.; Kou, X.; Yang, Z.; Wang, J. *Nano* **2008,** *2*, 677.

104. Zou, S.; Schatz, G. C. *Nanotechnology* **2006,** *17*, 2813.

105. Zou, S.; Janel, N.; Schatz, G. C. *J. Chem. Phys.* **2004,** *120*, 10871.

106. Zou, S.; Schatz, G. C. *J. Chem. Phys.* **2004,** *121*, 12606.

107. Jain, P. K.; Huang, W.; El-Sayed, M. A. *Nano Lett.* **2007,** *7*, 2080.

108. Gunnarsson, L.; Rindzevicius, T.; Prikulis, J.; Kasemo, B.; Kall, M.; Zou, S.; Schatz, G. C. *J. Phys. Chem. B* **2005,** *109*, 1079.

109. Arya, K. *Phys. Rev. B* **2006,** *74*, 195438.

110. Hao, E.; Schatz, G. C. *J. Chem. Phys* **2004,** *120*, 357.

111. Dahmen, C.; Schmidt, B.; Plessen, G. v. *Nano Lett.* **2007,** *7*, 318.

112. Ruppin, R. *Phys. Rev. B* **1982,** *26*, 3440.

113. Olk, P.; Renger, J.; Wenzel, M. T.; Eng, L. M. *Nano Lett.* **2008,** *8*, 1174.

114. Olk, P.; Renger, J.; Hartling, T.; Wenzel, M. T.; Eng, L. M. *Nano Lett.* **2007,** *7*, 1736.

115. Nordlander, P.; Oubre, C.; Prodan, E.; Li, K.; Stockman, M. I. *Nano Lett.* **2004,** *4*, 899.

116. Mishchenko, M. I.; Mackowski, D. W.; Travis, L. D. *Appl. Opt.* **1995,** *34*, 4589.

117. Yang, Y.; Shi, J.; Tanaka, T.; Nogami, M. *Langmuir* **2007,** *23*, 12042.

118. Zou, S.; Schatz, G. C. *Phys. Rev. B* **2006,** *74*, 125111.

119. Maier, S. A.; Brongersma, M. L.; Kik, P. G.; Atwater, H. A. *Phys. Rev. B* **2002,** *65*, 193408.

120. Quinten, M.; Kreibig, U. *Appl. Opt.* **1993,** *32*, 6173.

121. McKenzie, D. R.; McPhedran, R. C. *Nature* **1977,** *265*, 128.

122. García de Abajo, F. J. *Phys. Rev. B* **1999,** *60*, 6086.

123. García de Abajo, F. J. *Rev. Mod. Phys.* **2007,** *79*, 1267.

124. Sainidou, R.; García de Abajo, F. J. *Opt. Express* **2008,** *16*, 4499.

125. Khlebstov, B.; Melnikov, A.; Zharov, V.; Khlebstov, N. *Nanotechnology* **2006,** *17*, 1437.

126. Lassiter, J. B.; Aizpurua, J.; Hernandez, L. I.; Brandl, D. W.; Romero, I.; Lal, S.; Hafner, J. H.; Norlander, P.; Halas, N. J. *Nano Lett.* **2008,** *8*, 1212.

127. Sonnichsen, C.; Reinhard, B. M.; Liphardt, J.; Alivisatos, A. P. *Nat. Biotechnol.* **2005,** *23*, 741.

128. Reinhard, B. M.; Siu, M.; Agarwal, H.; Alivisatos, A. P.; Liphardt, J. *Nano Lett.* **2005,** *5*, 2246.

129. Warner, M. G.; Hutchison, J. E. *Nat. Mater.* **2003,** *2*, 272.

130. Lin, S.; Li, M.; Dujardin, E.; Girard, C.; Mann, S. *Adv. Mater.* **2005,** *17*, 2553.

131. Liao, J. H.; Chen, K. J.; Xu, L. N.; Ge, C. W.; Wang, J.; Huang, L.; Gu, N. *Appl. Phys. A* **2003,** *76*, 541.

132. Sardar, R.; Shumaker-Parry, J. S. *Nano Lett.* **2008,** *8*, 731.

133. Wei, Q. H.; Su, K. H.; Durant, S.; Zhang, X. *Nano Lett.* **2004,** *4*, 1067.

134. Fudouzi, H.; Xia, Y. *Langmuir* **2003,** *19*, 9653.

135. Zhang, H.; Edwards, E. W.; Wang, D.; Mohwald, H. *PCCP* **2006,** *8*, 3288.

136. Felidj, N.; Aubard, J.; Levi, G.; Krenn, J. R.; Salerno, M.; Schider, G.; Lamprecht, B.; Leitner, A.; Aussenegg, F. R. *J. Phys. Chem. B* **2002,** *65*, 075419.

137. Wang, H.; Levin, C. S.; Halas, N. J. *J. Am. Chem. Soc* **2005,** *127*, 14992.

138. Dong, W.; Dong, H.; Wang, Z.; Zhan, P.; Yu, Z.; Zhao, X.; Zhu, Y.; Ming, N. *Adv. Mater.* **2006,** *18*, 755.

139. Juillerat, F.; Solak, H. H.; Bowen, P.; Hofmann, H. *Nanotechnology* **2005,** *16*, 1311.

140. Yi, K. C.; Mendieta, V. S.; Castanares, R. L.; Meldrum, F. C.; Wu, C.; Fendler, J. H. *J. Phys. Chem.* **1995,** *99*, 9869.

141. Liang, Z.; Susha, A. S.; Caruso, F. *Adv. Mater.* **2002,** *14*, 1097.

142. Wang, S.; Sato, S.; Kimura, K. *Chem. Mater* **2003,** *15*, 2445.

143. Huang, H.-Y.; Chen, W.-F.; Kuo, P.-L. *J. Phys. Chem. B* **2005,** *109*, 24288.

144. Lin, X. M.; Wang, G. M.; Sorensen, C. M.; Klabunde, K. J. *103* **1999,** *26*.

145. Zhao, S.-Y.; Wang, S.; Kimura, K. *Langmuir* **2004,** *20*, 1977.

146. Osifchin, R. G.; Mahoney, W. J.; Bielefeld, J. D.; Andres, R. P. *Superlattices Microstruct.* **1995,** *18*, 283.

147. Fink, J.; Kiely, C. J.; Bethell, D.; Schiffrin, D. J. *Chem. Mater* **1998,** *10*, 922.

148. Chen, C.-F.; Tzeng, S.-D.; Chen, H.-Y.; Lin, K.-J.; Gwo, S. *J. Am. Chem. Soc* **2008,** *130*, 824.

149. Yao, H.; Minami, T.; Hori, A.; Koma, M.; Kimura, K. *J. Phys. Chem. B* **2006,** *110*, 14040.

150. Nishida, N.; Shibu, E. S.; Yao, H.; Oonishi, T.; Kimura, K.; Pradeep, T. *Adv. Mater.* **2008,** *9999*, 1.

151. Nykypanchuk, D.; Maye, M. M.; Lelie, D. v. d.; Gang, O. *Nature* **2008,** *451*, 549.

152. Park, S. Y.; Lytton-Jean, A. K. R.; Lee, B.; Weigand, S.; Schatz, G. C.; Mirkin, C. A. *Nature* **2008,** *451*, 553.

153. Zheng, N.; Fan, J.; Stucky, G. D. *J. Am. Chem. Soc* **2006,** *128*, 6550.

154. Compton, O. C.; Osterloh, F. E. *J. Am. Chem. Soc* **2006,** *129*, 7793.

155. Klajn, R.; Bishop, K. J. M.; Fialkowski, M.; Paszewski, M.; Campbell, C. J.; Gray, T. P.; Grzybowski, B. A. *Science* **2007,** *316*, 261.

156. Klajn, R.; Bishop, K. J. M.; Grzybowski, B. A. *Proc. Natl. Acad. Sci. U.S.A* **2007,** *104*, 10305.

157. Draine, B. T.; Flatau, P. J. *http://arxiv.org/abs/astro-ph/0409262* **2004**.

158. Mackowski, D. M. *J. Opt. Soc. Am. A* **1994,** *11*, 2851.

159. Mackowski, D. M.; Mischenko, M. I. *J. Opt. Soc. Am. A* **1996,** *13*, 2266.

160. Stratton, J. A., *Electromagnetic theory*. McGraw-Hill: New York, 1941.

161. Xu, X.; Cortie, M. B. *Adv. Func. Mater.* **2006,** *16*, 2170.

162. Cortie, M. B.; Xu, X.; Ford, M. J. *Phys. Chem. Chem. Phys.* **2006,** *8*, 3520.

163. Prescott, S. W.; Mulvaney, P. *J. Appl. Phys.* **2006,** *99*, 123504.

164. Draine, B. T. *J. Astrophys.* **1988,** *333*, 848.

165. Draine, B. T.; Goodman, J. J. *J. Astrophys.* **1993,** *405*, 685.

166. Draine, B. T.; Flatau, P. J. *J. Astrophys.* **1994,** *11*, 1491.

167. Purcell, E. M.; Pennypacker, C. R. *J. Astrophys.* **1973,** *186*, 705.

168. Goodman, J. J.; Draine, B. T.; Flatau, P. J. *Opt. Lett.* **1991,** *16*, 1198.

169. Collinge, M. J.; Draine, B. T. *J. Opt. Soc. Am. A* **2004,** *21*, 2023.

170. Felidj, N.; Aubard, J.; Levi, G. *J. Phys. Chem. C* **1999,** *111*, 1195.

171. Rahmani, A.; Chaumet, P. C.; Bryant, G. W. *J. Astrophys.* **2004,** *607*, 873.

172. Borghese, F.; Denti, P.; Saija, R.; Toscano, G.; Sindoni, O. I. *Aerosol Sci. Technol.* **1984,** *3*, 227-235.

173. Nehl, C. L.; Grady, N. K.; Goodrich, G. P.; Tam, F.; Halas, N. J.; Hafner, J. H. *Nano Lett.* **2004,** *4*, 2355.

174. Henglein, A. *J. Phys. Chem. B* **1993,** *97*, 5457.

175. Linnert, T.; Mulvaney, P.; Henglein, A. *J. Phys. Chem. B* **1993,** *97*, 679.

176. *International Organization for Standardization*, ISO 13321.

177. Charbonneau, P.; Reichman, D. R. *Phys. Rev. E* **2007,** *75*, 011507.

178. Harris, N.; Ford, M. J.; Cortie, M. B. *J. Phys. Chem. B.* **2006,** *110*, 10701.

179. Weaver, J. H.; Frederikse, H. P. R., *Optical properties of selected elements*. 82nd ed.; CRC Press: Boca Raton, FL, 2001; p 12.

180. García de Abajo, F. J. *J. Chem. Phys. C* **2008,** *112*, 17983.

181. Gale, J. D.; Rohl, A. L. *Mol. Simulat.* **2003,** *29*, 291.

182. Allen, M. P.; Tildesley, D. J., *Computer simulation of liquids*. Oxford University Press Inc.: New York, 2001.

183. Frenkel, D.; Smit, B., *Understanding molecular simulation*. Academic Press Limited: London, 1996.

184. Maier, S. A.; Kik, P. G.; Atwater, H. A. *Appl. Phys. Lett.* **2002,** *81*, 1714.

185. Brongersma, M. L.; Hartman, J. W.; Atwater, H. A. *Phys. Rev. B* **2000,** *62*, R16356.

186. Romero, I.; Aizpurua, J.; Bryant, G. W.; García de Abajo, F. J. *Opt. Express* **2006,** *14*, 9988.

187. Su, K.-H.; Wei, Q.-H.; Zhang, X.; Mock, J. J.; Smith, D. R.; Schultz, S. *Nano Lett.* **2003,** *3*, 1087.

188. Citrin, D. S. *Nano Lett.* **2005,** *5*, 985.

189. O'Neal, D. P.; Hirsch, L. R.; Halas, N. J.; Payne, J. D.; West, J. L. *Cancer Lett.* **2004,** *209*, 171.

190. Hu, M.; Petrova, H.; Hartland, G. V. *Chem. Phys. Letters* **2004,** *391*, 220.

191. Hu, M.; Hartland, G. V. *J. Phys. Chem. B* **2002,** *106*, 7029.

192. Mohamed, M. B.; Ahmadi, T. S.; Link, S.; Braun, M.; El-Sayed, M. A. *Chem. Phys. Letters* **2001,** *343*, 55.

193. Chou, C.; Chen, C.; Wang, C. R. C. *J. Phys. Chem. B* **2005,** *109*, 11135.

194. Djurisic, A. B.; Stanic, B. V. *Appl. Opt.* **1999,** *38*, 11 - 17.

195. Cengel, Y. A., *Heat Transfer A Practical Approach*. The McGraw-Hill Companies: 1998.

196. ASTM G159-98. Standard Tables for References Solar Spectral Irradiance at Air Mass 1.5: Direct Normal and Hemispherical for a 37° Tilted Surface. In American Society for Testing and Materials (ASTM): 1998.

197. Young, H. D.; Freedman, R. A., *University Physics with Modern Physics*. Addison Wesley Longman Inc: 2000.

198. Chen, G. *J. Heat Transfer* **1996,** *118*, 539.

199. Khanafer, K.; Vafai, K.; Lightstone, M. *Int. J. Heat Mass Transfer* **2003,** *46*, 3639.

200. Wen, D. S.; Ding, W. *IEEE Trans. Nanotechnol.* **2006,** *5*, 220.

201. Schelm, S.; Smith, G. B. *J. Opt. Soc. Am. A* **2005,** *22*, 1288.

202. Link, S.; El-Sayed, M. A. *J. Phys. Chem. B* **1999,** *103*, 8410.

203. Jain, P. K.; Lee, K. S.; El-Sayed, I. H.; El-Sayed, M. A. *J. Phys. Chem. B* **2006,** *110*, 7238.

204. Nova, C.; Gomez, D.; Perez-Juste, J.; Zhang, Z.; Petrova, H.; Reismann, M.; Mulvaney, P.; Hartland, G. V. *PCCP* **2006,** *8*, 3540.

205. Klajn, R.; Bishop, K. J. M.; Grzybowski, B. A. *Proc. Natl. Acad. Sci. U.S.A* **2006,** *104*, 10305.